Progress in Quantum Electronics 76 (2021) 100302

Contents lists available at ScienceDirect

Progress in Quantum Electronics

journal homepage: www.elsevier.com/locate/pqe

Review

Hexagonal boron nitride: Epitaxial growth and device applications

A. Maity, S.J. Grenadier, J. Li, J.Y. Lin *, H.X. Jiang **

Department of Electrical and Computer Engineering, Texas Tech University, Lubbock, TX, 79409, USA

A B S T R A C T

As a newest family member of the III-nitrides, BN is considered amongst the remaining frontiers in wide energy bandgap semiconductors with potentials for technologically significant applications in deep UV (DUV) optoelectronics, solid-state neutron detectors, electron emitters, single photon emitters, switching/memory devices, and super-capacitors. It was shown that it is possible to produce h-BN epilayers with high hexagonal phase purity, UV transparency, and film stoichiometry by employing nitrogen-rich growth conditions. The quasi-2D nature of h-BN supports unusually strong optical transitions near the band edge and a large exciton binding energy on the order of 0.7 eV. Due to the fact that the isotope of B-10 has a large capture cross-section for thermal neutrons, h-BN is an ideal material for the fabrication of solid-state neutron detectors for special nuclear materials detection, well and geothermal logging, and medical imaging applications. Freestanding B-10 enriched h-BN (h-^{10}BN) epilayers with varying thicknesses up to 200 μm have been successfully synthesized by metal organic chemical vapor deposition (MOCVD) as of this writing. By utilizing the conductivity anisotropy nature of h-BN, 1 cm^2 lateral detectors fabricated from 100 μm thick h-^{10}BN epilayers have demonstrated a detection efficiency of 59% for thermal neutrons, which is the highest on record among all solid-state neutron detectors as of today. It was noted that high growth temperatures, long growth times and the use of sapphire substrate tend to incorporate oxygen related impurities into h-^{10}BN epilayers, which strongly impacted the carrier mobility-lifetime (μτ) products and charge collection efficiencies of h-^{10}BN neutron detectors. As the h-BN material technology further develops, improved carrier mobilities and μτ products will allow the fabrication of h-BN devices with enhanced performance.

1. Introduction

III-nitride semiconductors, AlN, GaN, and InN have been under intensive studies over the last three decades and made grand-scale contributions to technological advances in high efficiency blue/green/white/UV light emitting diodes (LEDs) and laser diodes (LDs), solid-state lighting, and high power/temperature electronics [1–5]. As a newest family member of the III-nitride semiconductors, BN is considered amongst the remaining frontiers in wide energy bandgap semiconductors. BN has recently emerged as the material of choice for the exploration of technologically significant applications, including deep UV (DUV) optoelectronics, solid-state neutron detectors, electron emitters, single photon emitters, switching/memory devices, and super-capacitors. BN exists in three crystalline forms [6–8]. However, the sp^2-bonded hexagonal form (h-BN) is the most stable phase for BN grown at any temperatures under ambient pressure, whereas the stable crystalline structure of GaN, AlN and InN is Wurtzite. Fig. 1 shows the minimum direct energy bandgap vs. lattice constant for common compound semiconductors [5]. The general trend is that the bandgap and mechanical hardness increase with decreasing *a*-lattice constant. Experimental and theoretical studies have revealed that the minimum direct energy bandgap of h-BN is comparable to that of AlN [9–21]. Though it sits to the left of other III-nitride semiconductors in Fig. 1, the mechanical properties of h-BN vastly differ from other III-nitrides.

Hexagonal BN and graphite are two materials that are very similar in terms of crystal structures and lattice constants. As illustrated in Fig. 2, like graphite, h-BN has a layered structure. However, h-BN exhibits in stacking sequence with boron atoms in one layer directly

* Corresponding author.
** Corresponding author.
E-mail addresses: jingyu.lin@ttu.edu (J.Y. Lin), hx.jiang@ttu.edu (H.X. Jiang).

https://doi.org/10.1016/j.pquantelec.2020.100302

Available online 5 November 2020
0079-6727/

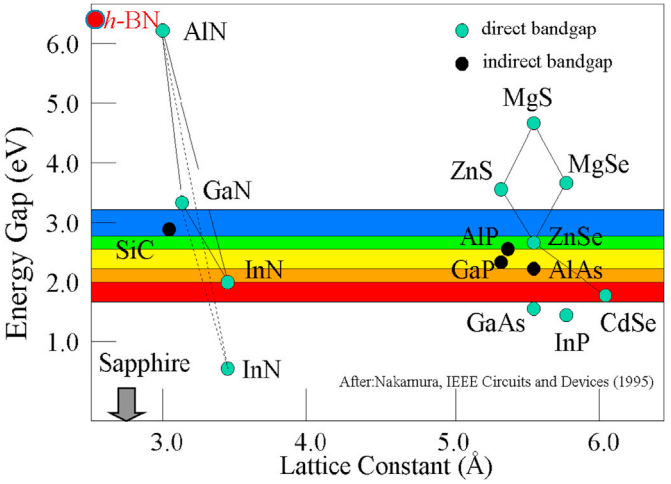

Fig. 1. Energy bandgap vs *a*-lattice constant for common compound semiconductors [Ref. 5; Credit: S. Nakamura, *IEEE Circuits and Devices Magazine* 11, 19 (1995)].

above nitrogen atoms in the adjacent layer, in which atoms within the layers are bonded together by strong covalent bonds (so called sp^2 bonding) while a weak van der Waals force occurs between the different layers. It has an in-plane *a*-lattice constant of 2.504 Å and out-of-plane *c*-lattice constant of 6.66 Å. The distance between nearest neighbors is 1.446 Å. Since every two layers form a repeated structure, the distance between two adjacent layers is hence 3.33 Å. The in-plane lattice constant difference is only about 1.5% between graphite and h-BN. Graphite is a well-studied material and interest has recently been renewed in it due to the discovery of its 2D form, graphene [22,23]. However, h-BN and graphite possess extremely different physical properties in terms of the band structures and the electrical and optical properties [8,24–27]. As shown in Table 1, in contrast to graphite which is a zero-energy bandgap material or semi-metal, undoped h-BN is optical transparent and highly insulating. Applications in electronics and photonics of these two materials are also on the opposite ends of the spectrum due to their disparate materials properties. While h-BN emits and absorbs in the deep ultraviolet wavelengths (~200 nm) [9–21,28–33], C-rich $(BN)_x(C_2)_{1-x}$ alloys absorb photons in the far IR region [33,34]. While undoped h-BN is highly resistive with an expected intrinsic electrical resistivity exceeding 10^{20} Ω cm and a measured resistivity of about 5×10^{14} Ω cm [33–40], graphite is highly conductive. Owing to its structural similarity to graphene, high resistivity, high breakdown field, and ability to provide an atomically flat surface with minimal density of dangling bonds and charge traps, h-BN has become an important member of the two-dimensional (2D) material family and is recognized as the most suitable material as the substrate/dielectric/separation layer for the construction of 2D heterojunction structures and devices [41–46]. Among all 2D materials being explored up to now, h-BN is the only 2D material with an ultrawide energy bandgap.

Table 1 also compares the basic physical parameters between h-BN and AlN. In comparison to other III-nitrides, h-BN has many unique features. Due to its layered structure, it is relatively easy to obtain atomically thin single h-BN sheets from h-BN bulk crystals by exfoliation [41–46], just like with obtaining graphene by exfoliation from graphite. Furthermore, as a layered semiconductor, most of its physical properties, including mechanical, optical, and electronic properties are highly anisotropic, i.e., properties in the c-plane are different from those along the c-axis, with some physical parameters differ by as much as one order of magnitude. On one hand, the anisotropy nature of h-BN increases the amount of effort needed to understand its basic properties since it doubles the parameters to be

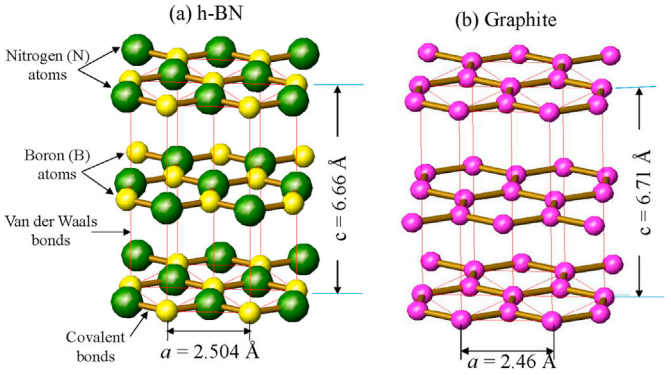

Fig. 2. (a) Schematic illustration of crystal structures of (a) *h*-BN and (b) graphite [After Ref. 27; Credit: M. R. Uddin, T. C. Doan, J. Li, K. S. Ziemer, J. Y. Lin, and H. X. Jiang, AIP Advances **4**, 087141 (2014).

probed. On the other hand, its layered structure gives rise to quasi-2D nature, leading to very strong optical transitions for the above band-edge photons [9,10,19], large density of states near the band-edge [19] and large exciton binding energy [14–21]. Moreover, the anisotropic nature of h-BN can be exploited to realize novel materials and devices with unique functionalities and improved performance. One outstanding example is the realization of freestanding h-BN epilayers by self-separation from sapphire substrate without the need to invoke techniques such as laser-lift-off or chemical etching commonly employed for substrate removal in the case for GaN wafers

Table 1
Comparison of basic parameters between h-BN and w-AlN.

Crystal Structure	Hexagonal BN	Graphite	Wurtzite *AlN*
c-lattice constant (Å)	6.66	6.71	4.98
a-lattice constant (Å)	2.50	2.46	3.112
Minimum direct energy gap (eV)	6.4	0	6.1
Theoretical hole effective mass (m_0) in-plane, out-of plane	0.5 (M→Γ), 1.33 (M→L)	0, 0	3.53
Theoretical electron effective mass (m_0) in-plane, out-of plane	0.26 (M→Γ), 2.21 (M→L)	0, 0	0.3
Electronic bonding	SP^2	SP^2	SP^3
Dielectric constant (in-plane, out-of plane)	6.85, 5.06	8.5	8.5
Thermal conductivity @ RT (W/m·K, in-plane)	500	250	285
Thermal expansion coeff.@ RT (10^{-6}/°C) (in-plane, out-of plane)	−2.7, 38	−1.2, 26	4.2
Melting point (^{0}C)	2970	3670	2270
Material density (g/cm^3)	2.1	2.26	3.26
E_A (eV, measured)	0.3 (Mg)		~0.5 (Mg)
In-plane hole mobility @ RT (cm^2/V·s)	35 (measured)		<5 (estimated)
Electrical resistivity of undoped epilayers (measured)	$>10^{14}$ Ω cm	10^{-5}	$>10^{14}$ Ω cm
P-type resistivity of Mg doped epilayers @ RT (Ω·cm) (Measured)	2–10		$> 10^6$
Breakdown field (MV/cm, out-of-plane, measured)	8		4

References used for Table 1.

•S.L" title = "http://www.ioffe.ru/SVA/NSM/Semicond/.

•S.L. Rumyantsev, M.E. Levinshtein, A.D. Jackson, S.N. Mohammmad, G.L. Harris, M.G. Spencer, and M.S. Shur in *Properties of Advanced SemiconductorMaterials GaN, AlN, InN, BN, SiC, SiGe*. Eds. M.E. Levinshtein, S. L. Rumyantsev, M. S. Shur, John Wiley & Sons, Inc., New York, 2001, 67–92.

•http://www.phy.mtu.edu/∼jaszczak/graphprop.html.

•Numerical/Data and Functional/Relationship in Science and Technology - Crystal and Solid-State Physics, edited by Q. Madelung, Landolt-Bornstein Vol. III (Springer, Berlin, 1972).

•R. S. Pease, "An X-ray study of boron nitride," Acta Crystallographica **5**, 536 (1952).

•R. W. Lynch and H. G. Drickamer "Effect of high pressure on the lattice parameters of diamond, graphite, and hexagonal boron nitride," J. Chem. Phys. **44**, 181 (1966).

•B. Arnaud, S. Lebègue, P. Rabiller, and M. Alouani, "Huge excitonic effects in layered hexagonal boron nitride," Phys. Rev. Lett., **96**, 026402 (2006) and "Arnaud, Lebègue, Rabiller, and Alouani Reply," Phys. Rev. Lett. **100**, 189702 (2008).

•L. Wirtz, A. Marini, and A. Rubio, "Excitons in boron nitride nanotubes: Dimensionality effects," Phys. Rev. Lett. **96**, 126104 (2006).

•X. K. Cao, B. Clubine, J. H. Edgar, J. Y. Lin, and H. X. Jiang, "Two-dimensional excitons in three-dimensional hexagonal boron nitride," Appl. Phys. Lett. **103**, 191106 (2013).

•B. Huang, X. K. Cao, H. X. Jiang, J. Y. Lin, and S. H. Wei, "Origin of the significantly enhanced optical transitions in layered boron nitride," Physical Review B **86**, 155202 (2012).

•T. C. Doan, J. Li, J. Y. Lin, and H. X. Jiang, "Bandgap and exciton binding energies of hexagonal boron nitride probed by photocurrent excitation spectroscopy," Appl. Phys. Lett. **109**, 122101 (2016).

•R. Dahal, J. Li, S. Majety, B.N. Pantha, X. K. Cao, J.Y. Lin, and H.X. Jiang, "Epitaxially grown semiconducting hexagonal boron nitride as a deep ultraviolet photonic material," Appl. Phys. Lett. **98**, 211110 (2011).

•S. Majety, J. Li, X. K. Cao, R. Dahal, B. N. Pantha, J. Y. Lin, and H. X. Jiang, "Epitaxial growth and demonstration of hexagonal BN/AlGaN p-n junctions for deep ultraviolet photonics," Appl. Phys. Lett. **100,** 061121 (2012).

•R. Geick, C. H. Perry, and G. Rupprecht, "Normal modes in hexagonal boron nitride," Phys. Rev. **146**, 543 (1966).

•A. Maity, S. J. Grenadier, J. Li, J. Y. Lin, and H. X. Jiang, "Hexagonal boron nitride neutron detectors with high detection efficiencies," J. Appl. Phys. **123**, 044501 (2018).

•A. Maity, S. J. Grenadier, J. Li, J. Y. Lin, and H. X. Jiang, "High sensitivity hexagonal boron nitride lateral neutron detectors," Appl. Phys. Lett. **114**, 222102 (2019).

•S. J. Grenadier, A. Maity, J. Li, J. Y. Lin, and H. X. Jiang, "Lateral charge carrier transport properties of B-10 enriched hexagonal BN thick epilayers," Appl. Phys. Lett. **115**, 072108 (2019).

•J. Li, S. Majety, R. Dahal, W. P. Zhao, J. Y. Lin, and H. X. Jiang, "Dielectric strength, optical absorption, and deep ultraviolet detectors of hexagonal boron nitride epilayers," Appl. Phys. Lett. **101**, 171112 (2012).

•K. B. Nam, M. L. Nakarmi, J. Li, J. Y. Lin, and H. X. Jiang, **"**Mg acceptor level in AlN probed by deep ultraviolet photoluminescence," Appl. Phys. Lett **83**, 878 (2003).

•M. L. Nakarmi, N. Nepal, C. Ugolini, T. M. Al Tahtamouni, J. Y. Lin, and H. X. Jiang, "Correlation between optical and electrical properties of Mg-doped AlN epilayers," Appl. Phys. Lett. **89**, 152120 (2006).

•Y. Taniyasu, M. Kasu, and T. Makimoto, "An aluminum nitride light-emitting diode with a wavelength of 210 nm," Nature, **441**, 325 (2006).

•R. Dahal, T. M. Al Tahtamouni, J. Y. Lin, and H. X. Jiang, "AlN avalanche photodetectors," Appl. Phys. Lett. **91**, 243503 (2007).

•G. H. Lee, Y. J. Yu, C. Lee, C. Dean, K. L. Shepard, P. Kim, and J. Hone, "Electron tunneling through atomically flat and ultrathin hexagonal boron nitride," Appl. Phys. Lett. **99**, 171103 (2011).

grown on sapphire substrates. Due to its unique layered structure shown in Fig. 2 and the difference in thermal expansion coefficients between h-BN and sapphire substrate, a thick h-BN epilayer tends to automatically separate from the sapphire substrate during cooling down after epitaxial growth to form a freestanding h-BN epilayer [35–40], as illustrated in Fig. 3(a). Fig. 3(b) is a photo of a freestanding Boron-10 enriched h-BN (h-^{10}BN) epilayer quarter-wafer of 4-inches in diameter and Fig. 3(c) shows the thickness profile probe measurement result which demonstrated that the thickness of this freestanding h-^{10}BN epilayer is ~203 μm, produced by the authors grown by metal organic chemical vapor deposition (MOCVD) method.

It has also been demonstrated that high crystalline III-nitrides can be grown on h-BN and vice versa [47,48]. The unique layer structured h-BN can be utilized as a release layer to obtain III-nitride micro- or nano-membranes and to facilitate the mechanical transfer of III-nitride based devices to other substrates. The utilization of h-BN as a releasing layer has been demonstrated recently for GaN blue LEDs and AlGaN/GaN heterostructures with an electron mobility and sheet density of 1100 cm^2/V and 1 × 10^{13}/cm^2 at room temperature [47,48], and h-BN deep ultraviolet detector structures [32] grown on sapphire. The orientation relationship between GaN, AlN, h-BN, and sapphire can be identified as (0001)sapphire || (0001)h-BN || (0001)AlN || (0001)GaN and [1_21_0]sapphire || [11_00]h-BN || [1100]AlN || [1100]GaN [47,48]. It has been demonstrated that the separation of the film takes place between the planes of the h-BN release layer [47,48].

A further example is the utilization of conduction anisotropy in h-BN, which has enabled the design of a novel lateral detector architecture with advantageous features of superior lateral charge transport properties, reduced dark current density, capacitance, and electronic noise over those of vertical devices [38–40]. This together with the realization of thick h-^{10}BN epilayers has ultimately led to the recent attainment of neutron detectors with 1 cm^2 detection area and a record high detection efficiency for thermal neutrons at 59% among all solid-state detectors to date [40]. Neutron detectors are an indispensable tool in geothermal and well logging and used to provide information for porosity evaluation, gas detection, shale evaluation, and borehole corrections. National security is another major end user of neutron detector for detecting the signatures of special nuclear materials and sensing any illicit movement of fissile materials at the ports of entry. Modern neutron tools commonly employ pressurized *He*(He-3) gas tube detectors, which is probably one of only few remaining detector technologies still relying on gases. However, being a gas, He-3 detectors are inherently bulky. Other shortcomings of He-3 detectors are the need of high pressurization, slow response speed (~ms) and expensive. These attributes prohibit flexibilities in detector design and form factors and increase exploration/logging time and maintenance costs. Additionally, He-3 gas detectors are most appropriate for operation below 175 °C. For well logging, the trend is moving into deep and slim wells where temperatures easily exceed 250 °C. For geothermal logging, the environmental conditions are even more extreme where temperatures can be as high as 500 °C. Therefore, solid-state alternatives with enhanced capabilities of operating in extreme environments of high temperatures are highly desirable. Similarly, for special nuclear materials detection, replacing pressurized ^{3}He gas tubes with high performance solid-state detectors will provide significant benefits including reduced size and weight, no pressurization, increased ruggedness, lower power consumption, larger/faster signals, and lower cost of fabrication, operation and maintenance.

Early calculation results revealed an indirect energy bandgap for h-BN with the top of the valence band located at the K-point (or the H-point) and the bottom of the conduction band located at the M-point [49–53]. However, many experimental results suggested that h-BN has very strong optical transitions with a comparable minimum direct energy bandgap as AlN [9–21,32]. More progress has been made in terms of understanding of the band structure of h-BN ever since the bulk crystals become available [15–17,54]. Fig. 4(a) shows the calculated first Brillouin zone (FBZ) of h-BN [15], which shows that h-BN has a hexagon structure with a 6-fold symmetry. Due to the

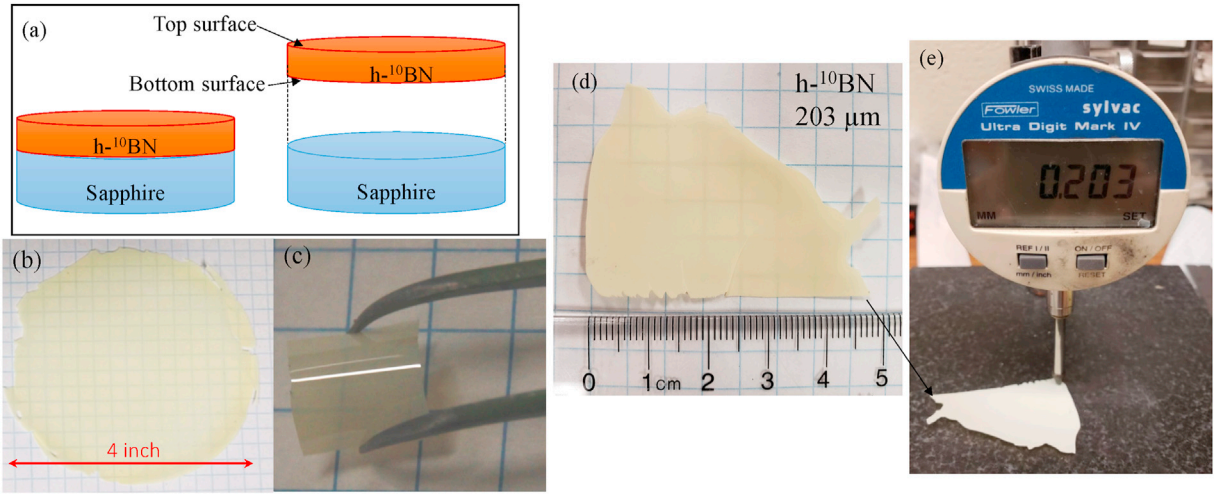

Fig. 3. (a) Schematic illustrations of h-^{10}BN epilayers grown on sapphire substrate and realization of freestanding h-BN epilayers via self-separation. Top and bottom surfaces are indicated with respect to the original interface between h-^{10}BN and sapphire [Ref. 37; Credit: A. Maity, S. J. Grenadier, J. Li, J. Y. Lin, and H. X. Jiang, J. Appl. Phys. **123**, 044501 (2018)]. (b) Photo of a freestanding h-^{10}BN wafer of 4-inches in diameter. (c) Photo of a representative freestanding h-^{10}BN layer showing its flexibility. (d) Photo of a diced freestanding h-^{10}BN quarter wafer of 4-inches in diameter. (e) Thickness profile probe measurement result demonstrated that the thickness of this freestanding h-^{10}BN epilayer is ~203 μm.

high symmetry of layered structure and weak interaction between layers within h-BN, the top (and bottom) plane of the FBZ containing high symmetry points of A, H, and L is very similar to that of the middle plane of the FBZ containing high symmetry points of Γ, K, and M, respectively. To be more specific, the dispersion along K → M is very similar to that of H → L. All-important high symmetry points, which determine its optical and electrical properties, lie at the edges of the FBZ, such as at M − , K-, H-, and L-points.

Fig. 4(b) plots the calculated energy diagram of h-BN along different high symmetry points [15], which reveals many unique features for h-BN: (1) Differ from other III-nitride semiconductors as well as from other common semiconductors, the conduction and valence band edges of the Γ-point or the center of the FBZ of h-BN is higher than those at the M − and K-points. Thus, the Γ-point is not so much relevant with respect to most of its electronic properties because electrons and holes are rarely excited to the Γ-point. (2) The calculated conduction band minimum (CBM) is at the M-point and the valence band maximum (VBM) is at the K-point, which implies that h-BN has an indirect bandgap [15]. (3) The dispersions along the k_z-direction, including K → H and M → L as well as for Γ → A, are extremely flat, reflecting the fact the effective masses of electrons and holes along the c-axis are high in comparison with those in the c-plane, including Γ → K and Γ → M. This is due to a weak interaction between the layers and a strong interaction within the layers. (4) Weak coupling between layers makes the energy difference between the calculated minimum direct bandgap located at the H-points and the indirect energy bandgap is quite small (~0.15–0.52 eV) [15,49]. (5) The self-energy correction increased the gap from 4.02 eV (LDA) to 5.95 eV and the minimum direct gap from 4.46 eV (LDA) to 6.47 eV [15]. In this sense, h-BN could behave quite differently from a typical indirect energy bandgap semiconductor. The higher symmetry points other than CBM and VBM could also contribute to the electrical and optical properties of h-BN. (6) Unlike other semiconductors with optical absorption and transition occurring only at one particular k-point in the FBZ for a fixed energy, optical transitions could occur in a broad range of k-region for a fixed energy value, such as between high symmetry points of K → H since the dispersion is so flat [9,10,19,20,32]. This could also explain the experimental observation of unusually strong optical transitions near the band-edge in h-BN [9–14,19,20,28–32].

Another interesting factor indicated by a previous calculation is that there exists a metastable structure of h-BN [55], which corresponds to a glide distance of B–N bond length (1.446 Å) of all B layers of an ABAB… stacking aligning in a direction of in-plane B–N bond. This metastable configuration is relatively stable since its total energy is only slightly above the ground state. More significantly, though the ground state is indirect, the metastable configuration forms a direct band with an energy gap of about 0.6 eV smaller than that of the ground state (indirect). This suggests that a perfect h-BN crystalline structure may have an indirect gap, whereas a metastable polytype may have a direct energy band gap. The calculation further suggested h-BN crystals with the P63/mmc symmetry to have mixed stacking behaviors of both ground state and metastable structures, resulting in mixed polytypes in typical h-BN crystals. Since epitaxial growth techniques such as MOCVD typically employ temperatures much lower than those used in bulk crystal growth (~1800 °C), it is possible that metastable structure could exist in typical h-BN epilayers. This together with the layer structure induced flatness in dispersion of high symmetry points may contribute to the difficulties in identifying whether the observed bandgap of h-BN is direct or indirect.

2. Epitaxial growth

2.1. *h-BN epilayers grown on sapphire substrates and key growth parameters*

MOCVD is a proven technique with the ability to grow precisely and reproducibly from single atomic layers to thick epilayers (tens of μm in thickness). Prior to the first application of MOCVD epitaxial growth technique to h-BN [56–59], earlier BN thin films grown on foreign substrates contain multiple phases, amorphous (a-BN) or turbostratic phase (t-phase or quasi-ordered structures). On the other hand, single atomic layers between 1 and 5 atomic layers of h-BN have been either isolated from bulk BN crystals which are typically millimeters in size or deposited on a metallic substrate by CVD technique [41–46]. The ability for synthesizing wafer-scale

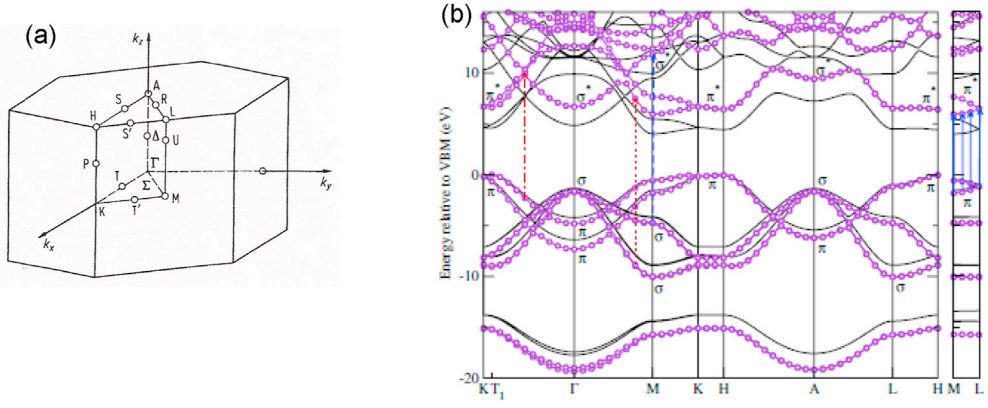

Fig. 4. (a) High symmetry points and directions of the hexagonal Brillouin zone. (b) Calculated electronic band structure along high-symmetry lines for bulk h-BN. The thin solid lines display the LDA results while the solid lines with open circles show the GW approximation results [Ref. 15; Credit: B. Arnaud, S. Lebe'gue, P. Rabiller, and M. Alouani, Phys. Rev. Lett. **96**, 026402 (2006) and **100**, 189702 (2008)].

semiconducting h-BN epitaxial layers with a high crystalline quality is expected to create opportunities for new advancements in fundamental understanding and device applications.

By leveraging the MOCVD growth technologies developed for GaN and AlN over the last several decades, the growth of h-BN epilayers by MOCVD has been successfully demonstrated recently by many groups [27–40,56–65]. The typical precursors for boron and nitrogen are triethylboron (TEB) and ammonia (NH_3), respectively and hydrogen is normally used as a carrier gas. Key growth parameters for obtaining BN epilayers in the hexagonal phase include the growth temperature, growth rate, V/III ratio, and low temperature buffer layer thickness. It was found that the use of a BN buffer layer of about 10 nm–20 nm in thickness deposited at about 800 °C on sapphire substrate prior to the growth of h-BN epilayer is helpful to overcome the lattice mismatch between h-BN and Al_2O_3 [28–30]. Furthermore, it was found that the use of the low temperature buffer layer also enhances the adhesion of thin h-BN epilayers to the substrates [28–30].

For h-BN epilayer growth, the surface migration of boron atoms tends to be poor because the B–N bond is very strong and parasitic reaction between TEB and NH_3 is severe, which resembles the reaction between NH_3 and trimethylaluminum (TMA) during AlN epilayer growth [66–69]. The by-products of the pre-reaction cause a rough surface and high crystalline defect density. The use of pulsed growth mode with alternating supplies of group III (TEB) and group V (NH_3) precursors can significantly suppress the parasitic reactions in the gas phase [28–31,56–59,62–65]. In a pulsed growth mode, there are 4 basic parameters that need to be optimized: "on" time for NH_3 flow (t_{NH3}), "on" time for TEB flow (t_{TEB}), TEB flow rate, and NH_3 flow rate. These parameters can be varied independently to produce materials with improved crystalline quality as well as to achieve different growth rates. This is exemplified in Fig. 5(a) [63], which compares the growth rates of BN epilayers in pulsed-mode and conventional continuous growth with different ammonia flow rates from 0.5 to 4 standard liter per minute (slm) at a growth temperature of 1330 °C. The results in Fig. 5(a) demonstrated that the growth rate in pulsed mode is almost independent of the NH_3 flow rate at approximately 1 nm/min, whereas the growth rate dramatically decreases at high NH_3 flow rates for conventional continuous growth, primarily attributed to a strong parasitic reaction between TEB and NH_3 in the vapor phase [63]. Moreover, the material quality of h-BN epilayers grown under pulsed growth mode is also superior over those grown under conventional continuous growth. This is confirmed by the results shown in Fig. 5(b) and (c), where the x-ray diffraction (XRD) θ-2θ scan results are presented for a set of 70 nm thick h-BN samples deposited at a growth temperature of 1330 °C under pulsed-mode with varying NH_3 flow rates from 0.5 to 2 slm using $t_{TEB} = 2$ s and $t_{NH3} = 1$ s [63]. The results clearly revealed that the pulsed-mode grown h-BN epilayers have much stronger peak intensities and narrower full width at half maxima (FWHM) of the h-BN (0002) peaks in XRD θ-2θ scans than those deposited by continuous growth [63]. This is because the parasitic reaction between TEB and NH_3 is very severe in the continuous growth mode.

Furthermore, as shown in Fig. 5(c), the measured c-lattice constants of the pulsed-mode grown materials approach to that of the bulk h-BN with increasing NH_3 flow rate, which indicates that it is possible to enhance the hexagonal phase by increasing NH_3 flow rate in the

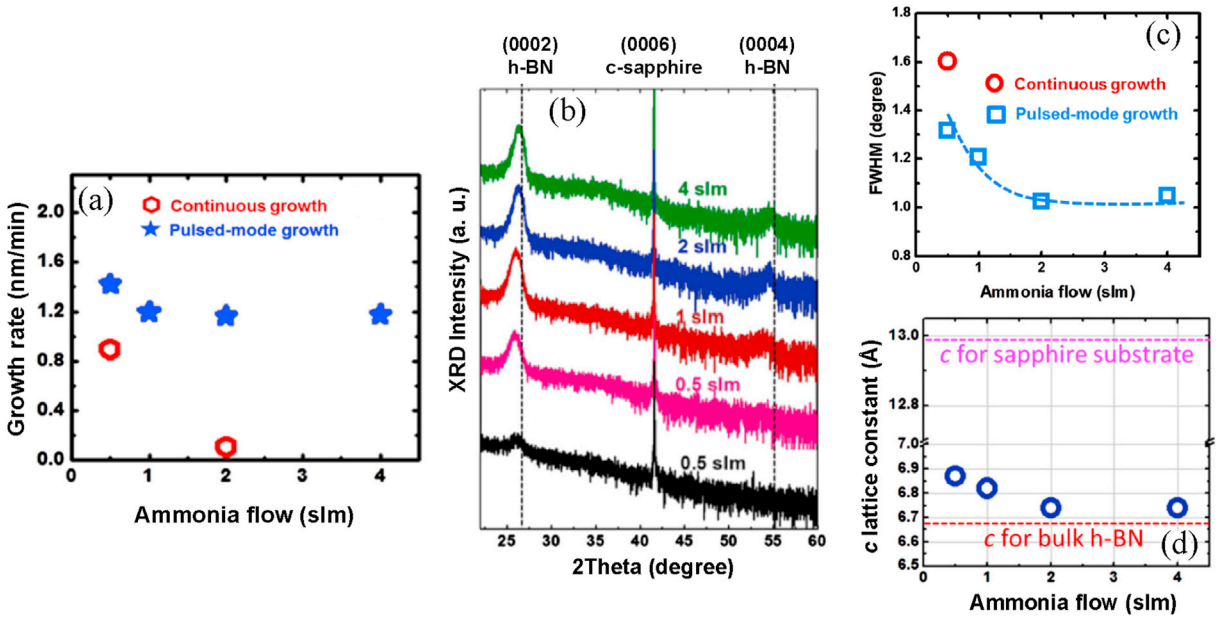

Fig. 5. (a) Growth rate of BN films in pulsed-mode (with $t_{TEB} = 2$ s and $t_{NH3} = 1$ s) and conventional continuous growth with different ammonia flows from 0.5 to 4 slm at a growth temperature of 1330 °C. (b) XRD θ-2θ scans of 70-nm thick BN layers deposited at a growth temperature of 1330 °C under different conditions: the curve at the bottom from conventional continuous growth and the others from pulsed-mode growth with $t_{TEB} = 2$ s and $t_{NH3} = 1$ s. (c) The FWHM of h-BN (0002) peak in XRD θ-2θ scans as a function of the NH_3 flow; The BN layers were grown by pulsed-mode growth (open squares) and by conventional continuous growth (open circles). (d) The c-lattice constant as a function of the NH_3 flow in pulsed-mode growth [Ref. 63; Credit: X. Yang, S. Nitta, K. Nagamatsu, S. Y. Bae, H. J. Lee, Y. H. Liu, M. Pristovsek, Y. Honda and H. Amano, J. Cryst. Growth **482**, 1 (2018)].

pulsed growth mode [63]. The deviations of the measured c-lattice constant of h-BN epilayers from the bulk c-lattice value can be attributed to the fact that MOCVD grown h-BN epilayers contain inclusions of quasi-ordered turbostratic phase of BN (t-BN) [63]. Overall, the XRD data shown in Fig. 5 confirmed that the conventional continuous growth produced epilayers with poorest phase purity and that the use of high NH_3 flow rates is beneficial for obtaining h-BN epilayers with improved hexagonal phase purity. Surface morphologies of h-BN epilayers probed by atomic force microscopy (AFM) revealed that the use of low V/III ratio tends to cause 3D islands with large surface roughness. With increasing V/III ratio, pre-nitridation occurs and smooth h-BN surface can be achieved [63–65]. Prior results seem to suggest that the use of high NH_3 flow rates provides unintentional nitridation and thereby creates high density of nucleation sites, which eventually supports the growth of smooth and continuous h-BN surface [63–65].

Additionally, the use of high NH_3 flow rates is also necessary to provide h-BN epilayers with a high optical transparency and good stoichiometry. This is demonstrated by optical micrographs of h-BN epilayers deposited on sapphire substrates at varying NH_3 flow rates produced by the authors using MOCVD shown in Fig. 6(a). The results clearly signify that it is possible to obtain transparent thin films at relatively high NH_3 flow rates. The secondary ion mass spectrometry (SIMS) characterization results are shown in Fig. 6(b) and (c) for h-BN epilayers deposited at 1350 °C under two different NH_3 flow rates, $NH_3 = 0.1$ slm and (b) $NH_3 = 1$ slm, produced by the authors using MOCVD [25,27], which revealed that the h-BN epilayer grown under $NH_3 = 1$ slm has an excellent stoichiometry [28,30], whereas the layer deposited under $NH_3 = 0.1$ slm has a deficiency of nitrogen. We would like to point out that the results of Fig. 6 are shown for h-BN epilayers with a comparable thickness grown under the same growth temperature (1350 °C), so that the effects of layer thickness and growth temperature on the film stoichiometry and transparency can be neglected in this case. This suggests that epilayers deposited at low NH_3 flow rates contain higher nitrogen vacancies (V_N). The presence of high density of V_N opens the door for the incorporation of other defects such as carbon impurities occupying the nitrogen sites, C_N, and oxygen impurities occupying the nitrogen sites, O_N [70–90]. The presence of these defects in h-BN has a profound influence on the optical and transport properties of h-BN [70–90].

The photoluminescence (PL) emission properties of *h*-BN epilayers grown under different NH_3 flow rates have also been investigated to gain insights into the effects of V_N and other defects in the PL emission properties of *h*-BN epilayers [80,81]. Fig. 7(a) shows the room temperature PL spectra of *h*-BN epilayers grown at 1350 °C under varying NH_3 flow rates ranging from 0.2 to 1.5 SLM [80,82], whereas Fig. 7(b) shows the 10 K PL spectra of *h*-BN epilayers grown at 1350 °C under varying NH_3 flow rates ranging from 0.2 to 20 SLM, corresponding to a maximum V/III ratio of about 8000, with all other growth conditions being identical [81,82]. The samples were placed side-by-side during the PL spectra measurements for spectral feature and emission intensity comparison. The results shown in Fig. 7(a) reveal three impurity peaks below 5 eV, which were identified as a donor-acceptor pair (DAP) transition with a zero-phonon line (ZPL) near 4.1 eV and its phonon replicas at 3.9 and 3.7 eV, involving longitudinal optical (LO) phonons [80–82]. As shown in Fig. 7(b), in the epilayers grown under low NH_3 flow rates (between 0.3 up to 1.0 SLM), two other emission lines near 5.3 eV and 5.5 eV

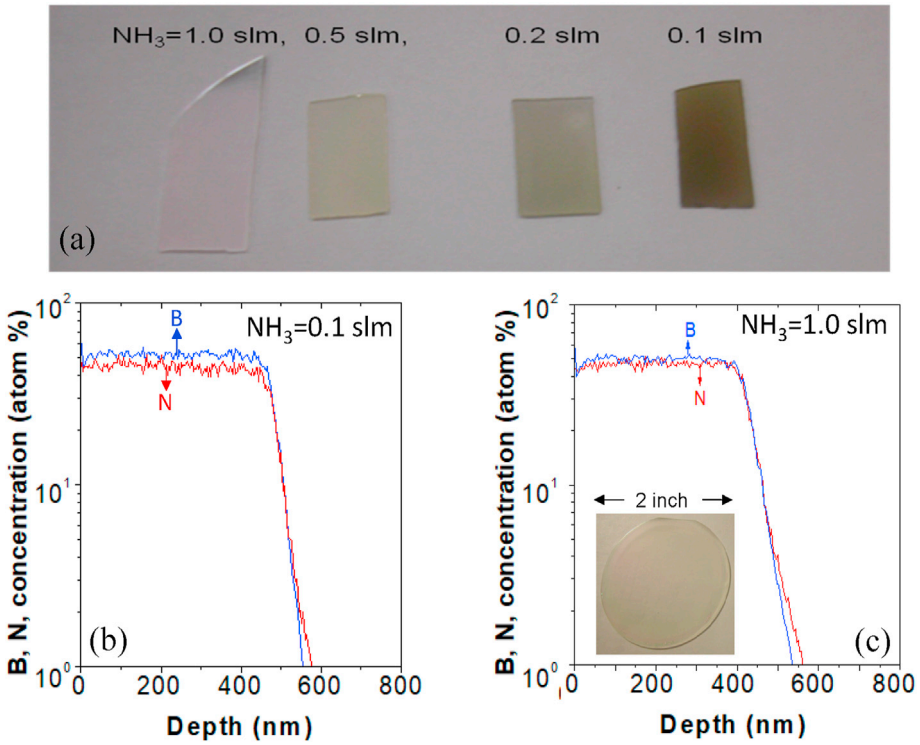

Fig. 6. (a) Transparency of h-BN epilayers of 1 μm in thickness deposited on sapphire using varying NH_3 flow rates from 0.1 slm to 1 slm. (b)–(c) Results of depth profiling probed by secondary ion mass spectrometry (SIMS) for h-BN epilayers grown under two different NH_3 flow rates: (a) $NH_3 =$ 0.1 slm and (b) $NH_3 = 1$ slm. The inset is an optical image of a 2-inch *h*-BN epilayer on sapphire.

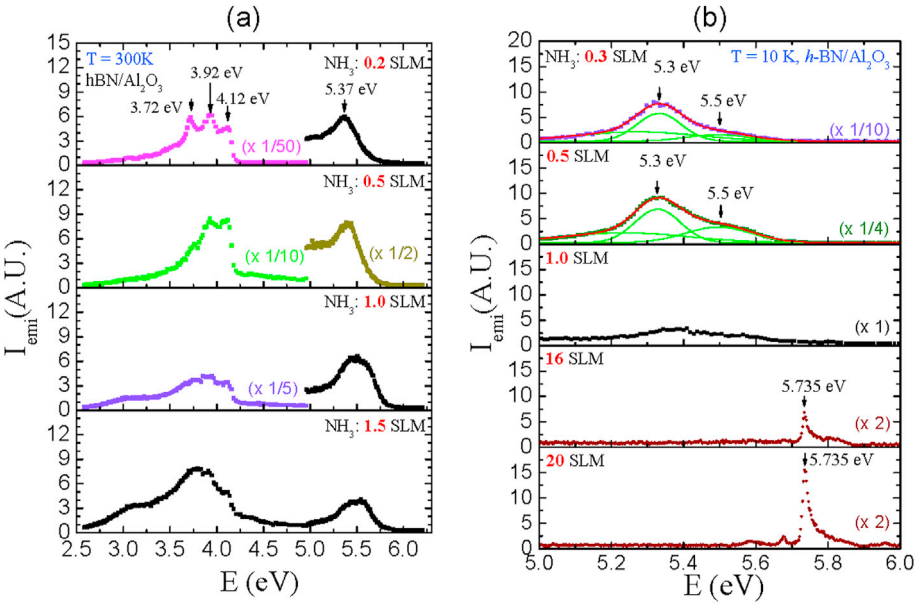

Fig. 7. (a) 300 K PL spectra of impurity related transitions in *h*-BN epilayers of about 0.5 μm in thickness grown at 1350 °C under different NH_3 flow rates [Ref. 80, Credit: X. Z. Du, J. Li, J. Y. Lin, and H. X. Jiang, Appl. Phys. Lett. **106**, 021110 (2015)]. (b) 10 K PL spectra of near band-edge transitions in *h*-BN epilayers of about 0.5 μm in thickness grown under different NH_3 flow rates. The spectra are vertically shifted to provide a clearer presentation [Refs. 81; Credit: X. Z. Du, J. Li, J. Y. Lin, and H. X. Jiang, Appl. Phys. Lett. **108**, 052106 (2016)].

are also clearly resolved, corresponding to a quasi-DAP (q-DAP) transition and a bound exciton transition, respectively [14,20,70, 83–87]. The observation of a q-DAP transition near 5.3 eV suggests that the DAP transition in the epilayers grown at low NH_3 flow rates is under a strong influence of the tail states in the bandgap as a consequence of impurity compensation [83,84].

It can be seen from Fig. 7 that the emission intensities of impurity related transition lines (DAP, q-DAP, and bound exciton transitions) all decrease continuously with an increase of the NH_3 flow rate. The most notable feature revealed in Fig. 7(b) is that the impurity related emission lines disappear altogether, and a sharp emission line emerges at 5.735 eV when the NH_3 flow rate is increased to above 16 SLM [80–82], which was attributed to the free exciton recombination in h-BN epilayers [81]. The elimination of the impurity emission lines in *h*-BN epilayers grown under high NH_3 rates implies that the impurity emission lines are most likely related to V_N. During the growth of *h*-BN epilayers, NH_3 serves as the source of the nitrogen atoms. V_N and carbon impurities occupying the nitrogen sites (C_N) are known to be two common impurities in *h*-BN [70–78]. The results shown in Fig. 7 together with those of Figs. 5 and 6 demonstrated that the hexagonal phase purity, UV transparency, film stoichiometry, and PL emission properties of h-BN epilayers can all be improved by employing nitrogen-rich growth conditions.

An early work has shown that MOCVD growth temperatures between 950 and 1100 °C with V/III ratios between 20 and 70 produced colorless and transparent h-BN epilayers and the c-lattice constant and FWHM of the h-BN (0002) peak in XRD θ-2θ scans decreased with an increase of the growth temperature [56]. From these results, the authors predicted that a growth temperature of 1500 °C may be

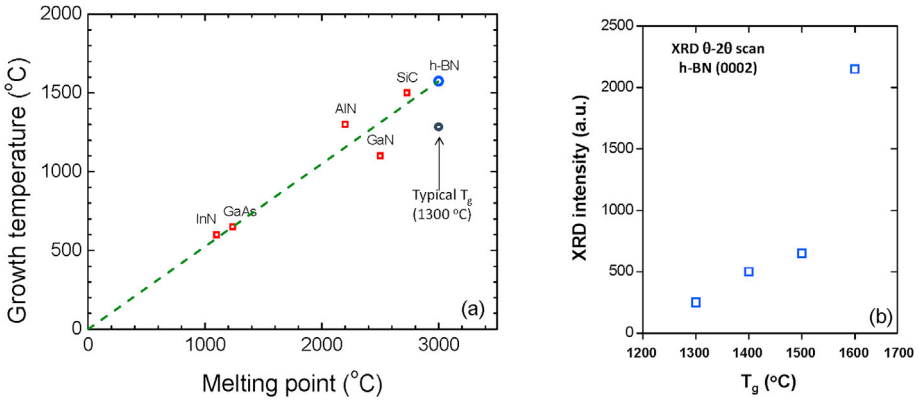

Fig. 8. (a) Empirical data of the typical epi-growth temperature (T_g) (open squares) vs. melting point for several materials. (b) The observed relative XRD intensity of the h-BN (0002) peak in θ-2θ scan as a function of the epi-growth temperature, T_g.

needed for MOCVD grown h-BN epilayers to possess the same c-lattice constant as h-BN bulk crystal [56]. Due to the high melting point of h-BN, many commercially available growth systems are not capable of providing sufficiently high growth temperatures and temperature uniformity necessary for synthesizing large-area h-BN epilayers at high growth rates with high crystalline quality. The empirically observed relationship between the melting point (T_m) and the epi-growth temperature (T_g) plotted in Fig. 8(a) for different semiconductors including other III-nitrides provides insights into the significance of the growth temperature. Since *h*-BN has a higher melting point than other III-nitride semiconductors, its optimal growth temperature is expected to be higher than those of all other III-nitride semiconductor such as AlN epilayers. The trend shown in Fig. 8(a) suggests that the desired growth temperature for *h*-BN epilayers is around 1600 °C. This observation is consistent with results shown in Fig. 8(b), which indicate that the XRD intensity of the *h*-BN (0002) peak in θ-2θ scans and hence the crystalline quality increases for epilayers grown at higher temperatures.

A detailed study on the h-BN epilayer quality for varying growth temperature (T_g) and V/III ratio has been conducted recently [65], from which the authors have categorized h-BN epilayers based on three growth regions of NH_3 flow rates (V/III ratios), i.e. low, intermediate, and high and two regions based on T_g [65]. The low-medium NH_3 flow rate boundary was determined by the physical color transition from yellowish color (low V/III ratio) to transparent stoichiometric h-BN epilayers, whereas the boundary between intermediate and high NH_3 flow rates was determined by the transition between continuous multi-layer growth to self-limited growth of a few monolayers. Furthermore, stoichiometric h-BN epi-growth at the intermediate and high NH_3 flow rates can be further divided into two growth temperature zones with a boundary at $T_g = 1500$ °C based on the observation of near band-edge PL emission from h-BN epilayers. Epilayers grown at $T_g > 1500$ °C at high NH_3 flow rates exhibited free excitonic transitions at 5.743 eV (215.9 nm) and 5.904 eV (210 nm) along with the bound excitonic transition at 5.59 eV (221.8 nm) in PL spectra measured at room temperature, which demonstrates the attainment of high quality material of h-BN epilayers [65]. Relatively low-quality h-BN epilayers with a broader peak of PL emission at 5.66 eV (219 nm) was found at the growth conditions of $T_g < 1500$ °C ($T_g > 1500$ °C) with high (intermediate) NH_3 flow rates. Their results indicated that the NH_3 flow rate needed for producing transparent h-BN epilayers is inversely related to the growth temperature [65]. This is understandable because the cracking efficiency of NH_3 and hence the supply of nitrogen increases at higher temperatures. However, at low NH_3 flow rates, no band-edge PL emission was observable at any growth temperatures [65].

It is useful to calibrate the crystalline quality of MOCVD grown h-BN epilayers at the present stage against that of the more mature AlN epilayers with a comparable energy bandgap. Fig. 9 summarizes XRD characterization results for a representative h-BN epilayer grown at a temperature of 1350 °C on sapphire substrate by the authors [28,30,91]. The typical XRD θ-2θ scan shown in Fig. 9(a) revealed three peaks, corresponding to the *h*-BN (0002), (0004), and (0006) at 26.70°, 55.06°, and 88.00°, respectively, with no other visible peaks [28,30,91]. The results revealed a c-lattice constant of ~6.67 Å [28,30], which matches closely with the bulk c-lattice constant of h-BN (c = 6.66 Å) [6,7]. The slight deviation of the measured c-lattice constant of this h-BN epilayer from the bulk c-lattice constant value is again an indication that this h-BN epilayer may contain inclusions of t-BN, which is consistent with the observation shown in Fig. 5 [63]. This is partly because the growth temperature of 1350 °C is still not high enough to crystallize BN into a perfect hexagonal phase. Fig. 9(b)–(c) compare the XRD θ-2θ scans and rocking curves (ω-scans) of the (0002) diffraction peaks of h-BN and AlN epilayers with a similar thickness. The results indicate that the XRD intensity of the (0002) peak of *h*-BN is about 30 times lower than that of AlN epilayer with the same thickness [32]. The XRD rocking curve of h-BN has a FWHM of ~380 arcsec. In comparison with other III-nitride materials, the FWHM of XRD (0002) rocking curve of h-BN is comparable to those of typical GaN epilayers grown on c-plane sapphire (around 290 arcsec) [4]; however is 6 times broader than those of high quality AlN epilayers deposited on c-plane sapphire (around 60 arcsec) [66]. In III-nitride materials, it is well known that the FWHM of XRD rocking curves is correlated with the density of dislocations [4,66,92,93]. In the case of h-BN with layered structure, the FWHM could also reflect the presence of misalignment between layers, inclusion of t-phase domains, stacking faults and native and point defects. As shown in the inset of Fig. 9(c), thin h-BN epilayers (<1 μm) exhibit good surface morphologies and a root mean square (RMS) surface roughness value of less than 1 nm can be obtained. These results signify that it is feasible to obtain h-BN epilayers with high crystalline quality by MOCVD and that the development of

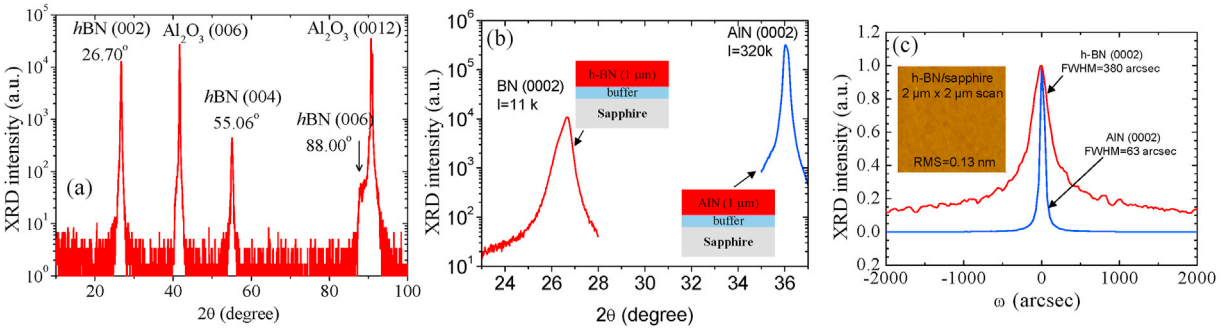

Fig. 9. (a) XRD θ-2θ scan of an *h*-BN epilayer grown on sapphire at a growth temperature of 1350 °C, providing a *c*-lattice constant of 6.67 Å [Ref. 91; Credit: T. C. Doan, J. Li, J. Y. Lin, and H. X. Jiang, AIP Advances **4**, 107126 (2014)]. (b) and (c) Comparison of XRD characterization results between *h*-BN and AlN epilayers of 1 μm in thickness deposited on sapphire: (b) θ-2θ scans and the insets are schematics of epilayer structures. [Ref. 32; Credit: J. Li, S. Majety, R. Dahal, W. P. Zhao, J. Y. Lin, and H. X. Jiang, Appl. Phys. Lett. **101**, 171112 (2012)] and (c) rocking curves (ω-scans) of (0002) peaks and the inset is an AFM surface morphology of h-BN over a 2 × 2 μm^2 area scan [Ref. 91; credit: T. C. Doan, J. Li, J. Y. Lin, and H. X. Jiang, AIP Advances **4**, 107126 (2014)].

epitaxial layers of h-BN is in its early stage compared to AlN and GaN epilayers.

On the other hand, the material quality of h-BN epilayers can also be calibrated against those of h-BN bulk crystals. Direct comparison among XRD rocking curves is difficult because h-BN bulk crystals are still small and contain multi-domains. However, individual h-BN bulk crystallites possess excellent optical properties. In particular, the spectral line shape and intensity of the Raman peaks follow the selection rules that are governed by the symmetry of the transition. The shift of the Raman peaks indicates a change in bonding or electronic energy levels, while the linewidth is directly correlated with the crystalline quality. The mode at $\Delta\sigma = 1370\ cm^{-1}$ in h-BN is attributed to the E_{2g} vibration mode [94], corresponding to the in-plane stretch of B and N atoms as illustrated in the inset of Fig. 10(a). Although a FWHM as narrow as $10\ cm^{-1}$ for the E_{2g} mode with a peak position $\Delta\sigma = 1370\ cm^{-1}$ in Raman spectra has been previously observed in ultrathin h-BN epilayers grown by the authors using MOCVD [95], Fig. 10 indicates that the typical linewidth of the Raman mode for MOCVD grown epilayers is generally greater than $10\ cm^{-1}$, whereas those of bulk crystals are narrower than $10\ cm^{-1}$. These comparison results indicate that many improvements in material quality of h-BN epilayers are still anticipated.

2.2. Hexagonal BN/w-AlGaN p-n junctions

The poor p-type conductivity of Al-rich $Al_xGa_{1-x}N$ alloys is a major obstacle that limits the quantum efficiency (QE) of DUV light emitting devices operating in the UV-C range, which is the most effective wavelength for the destruction of the nucleic acids in microorganisms such as pathogens and viruses. This issue is mainly caused by the deepening of the Mg acceptor level in $Al_xGa_{1-x}N$ alloys with increasing x, from about 170 meV (x = 0) to 530 meV (x = 1) [96–101]. Since the free hole concentration depends exponentially on acceptor energy level (E_a), an E_a value around 500 meV translates to only 1 free hole for roughly every 2 billion (2×10^9) incorporated Mg impurities (at 300 K). This causes an extremely low free hole injection efficiency into the quantum well (QW) active region. As shown schematically in Fig. 11(a), a conventional III-nitride DUV emitter typically incorporates an electron-blocking (e-blocking) layer with a larger energy bandgap than the active region to maximize the electron-hole radiative recombination in the QW active region. The Al-rich AlGaN e-blocking layer is the most resistive p-layer in the DUV light emitters. Unfortunately, this highly resistive e-blocking layer must have a certain thickness in order to stop the electrons to overflow into the p-layers and to eliminate the unwanted long wavelength emission due to the recombination between electrons and Mg impurities in the p-type layers. Thus, the highly resistive nature of this e-blocking layer is one of the primary causes of low hole injection efficiency and, consequently, low QE of nitride DUV emitters. Although various interesting schemes, such as polarization and piezoelectric doping [102,103], p-AlGaN graded layers [104,105], p-type multiple quantum wells or superlattices [106] have been employed to overcome to some extent the problem of low hole injection efficiency, the exploitation of disruptive device concepts could bring significant advances in the QE of DUV emitters.

Fig. 11(b) illustrates a new p-type layer strategy based on h-BN with the aim to overcome the intrinsic problem of low p-type conductivity (or low free hole concentration) [29–31]. By implementing the wide bandgap and h-BN p-type layer strategy, p-type conductivity of the electron blocking layer will be increased and light absorption in the DUV spectral region will be reduced compared to the conventional approach of using a p-GaN contact layer shown in Fig. 11(a). If successful, this will improve the free hole injection and QE, reduce the contact resistance, operating voltage, and heat generation, and increase the device operating lifetime.

To realize the DUV emitter structure shown in Fig. 11(b), the ability of epitaxial growth of h-BN on AlGaN epilayer is a prerequisite. The lattice mismatch is about 19.54% when h-BN epilayer is grown on a c-plane AlN epilayer. However, it was noted that 4 *a*-lattice constants of AlN ($4\ a_{AlN} = 4 \times 0.3112\ nm = 1.245\ nm$) is almost the same as 5 *a*-lattice constants of h-BN ($5\ a_{BN} = 5 \times 0.2504\ nm = 1.252\ nm$) [30,31]. This means that every 5 atoms in h-BN will align with 4 atoms in w-AlN along the *a*-direction, as illustrated in Fig. 12(a) [30,31]. This 5/4 coincidence in the h-BN/w-AlN heterojunction interface reduces the effective lattice mismatch from 19.54% to 0.58%. The feasibilities of growing h-BN epilayers on top of AlN epilayers [29,30,64] as well as of AlGaN epilayers on h-BN epilayers [47,48] have been demonstrated via MOCVD growth. As shown in Fig. 12(b), a linewidth of 660 arcsec for the XRD rocking curve for the

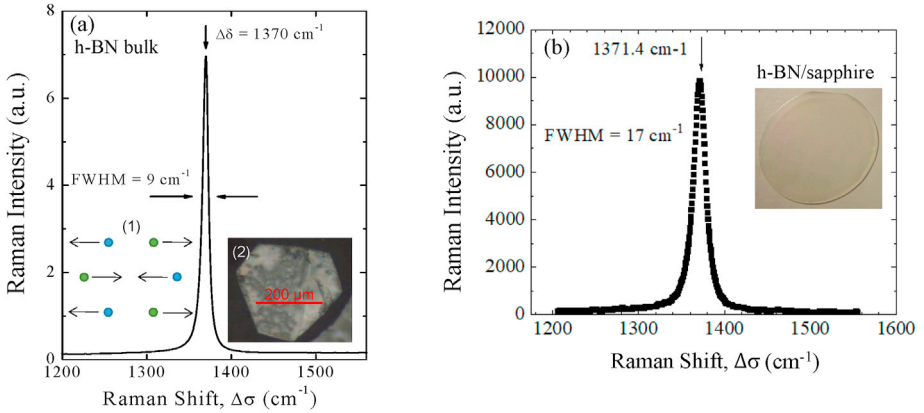

Fig. 10. Comparison of Raman spectra using 780 nm excitation between (a) h-BN bulk crystallite [Ref. 18; Credit: X. K. Cao, B. Clubine, J. H. Edgar, J. Y. Lin, and H. X. Jiang, Appl. Phys. Lett. **103**, 191106 (2013)] and (b) 0.5 μm thick h-BN epilayer grown on sapphire. Inset (1) in (a) is a schematic illustration of the E_{2g} symmetry vibration, corresponding to the in-plane stretch of B and N atoms and inset (2) in (a) is a micrograph of a bulk crystal.

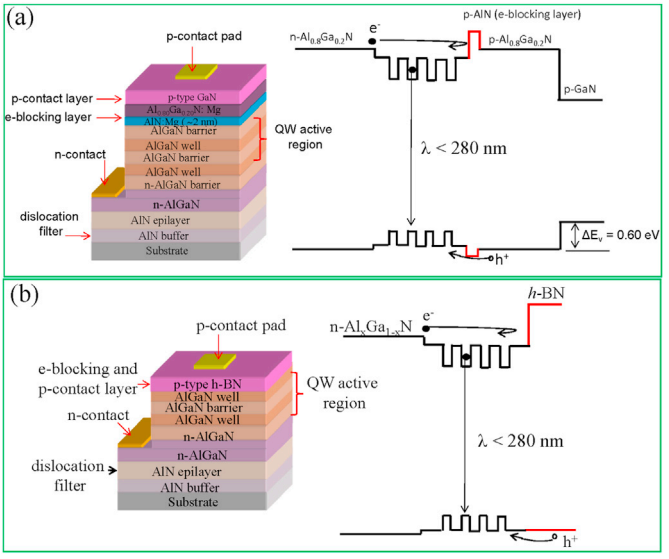

Fig. 11. (a) Schematic diagram of conventional DUV emitter approach and the corresponding energy band diagram of the device layer structure. The e-blocking layer based on AlN or Al-rich AlGaN are generally highly resistive due to the large activation energies of Mg acceptors in AlN and Al-rich AlGaN, which cause very low hole injection efficiencies. The use of p-GaN contact layer also reduces the DUV transparency. (b) Schematic of DUV emitter layer structure using p-type h-BN and the corresponding energy band diagram [Refs. 30 and 31; Credit: H. X. Jiang and J. Y. Lin, Semicon. Sci. Technol. **29**, 084003 (2014)].

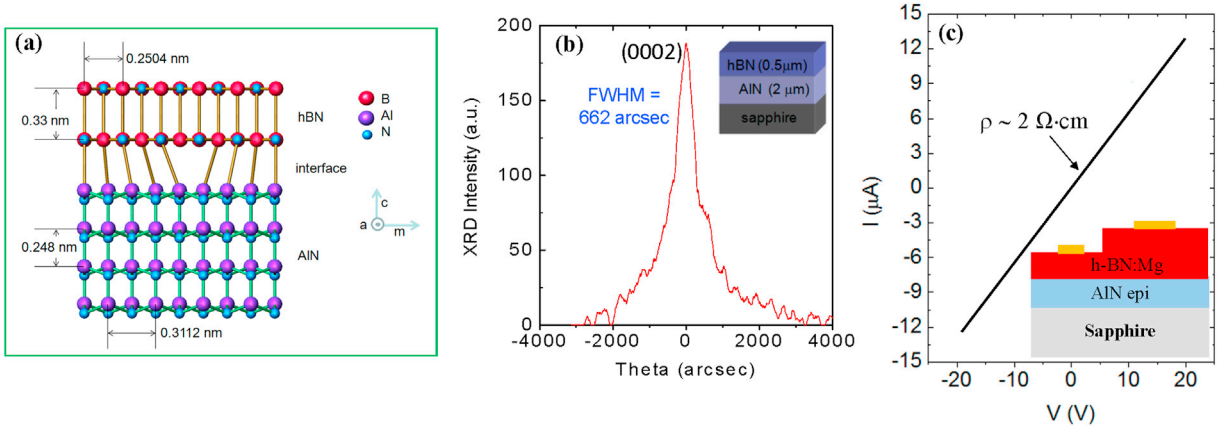

Fig. 12. (a) Illustration of the heteroepitaxial growth of h-BN on wurtzite AlN (w-AlN). Note that 4 *a*-lattice constants of AlN (4 $a_{AlN} = 4 \times 0.3112$ nm = 1.245 nm) are almost the same as that of 5 *a*-lattice constants of h-BN (5 $a_{BN} = 5 \times 0.2504$ nm = 1.252 nm) [Ref. 30, Credit: H. X. Jiang and J. Y. Lin, Semicon. Sci. Technol. **29**, 084003 (2014)]. (b) XRD rocking curve (ω-scan) of the (0002) peak of h-BN epilayers deposited on AlN-epilayer/sapphire templates [Ref. 29; Credit: S. Majety, J. Li, X. K. Cao, R. Dahal, B. N. Pantha, J. Y. Lin, and H. X. Jiang, Appl. Phys. Lett. **100**, 061121 (2012)]. (c) I–V characteristics of h-BN:Mg epilayer deposited on highly insulting AlN with Ni contacts thermally annealed at 1020 °C for 1 min.

h-BN (0002) peak for h-BN epilayers deposited on AlN epilayers has been achieved [29]. A more recent study on the nucleation of h-BN epilayers on (0 0 0 1) AlN templates revealed that increasing the TEB flow rate aided the nuclei growth [64]. Initial h-BN layers on AlN were tilted. With further growth of BN epilayer on the top of initial nuclei, layered (0 0 0 1) h-BN formed, and continuous uniform h-BN layer can be obtained [64].

For the growth of Mg doped h-BN epilayers (h-BN:Mg), biscyclopentadienyl-magnesium was transported into the reactor during h-BN epilayer growth [28–30]. A Mg-doping concentration of about 1×10^{19} cm^{-3} was obtained, as verified by SIMS measurement [28]. From the temperature dependent resistivity measurement result performed on an h-BN:Mg epilayer grown on sapphire substrate, the estimated activation energy (E_A) of Mg in h-BN is around 31 meV [28]. The measured E_A value in this case is not necessarily the energy level of Mg impurity in h-BN or the value expected from the effective mass theory because of relatively heavy doping and layered structure of h-BN. The Hall-effect measurement results confirmed p-type conduction with a free hole concentration p~10^{18} cm^{-3} and an average mobility μ ~2 $cm^2/V{\cdot}s$ [30]. Due to the low value of the hole mobility, the Seebeck effect measurements (or the hot probe method) was also performed to further confirm the conductivity type of h-BN:Mg epilayers [28]. The observation of a sign reversal in the

Seebeck coefficient over a highly n-type $In_{0.3}Ga_{0.7}N$:Si sample confirmed unambiguously that h-BN:Mg epilayers are p-type [28]. For the h-BN:Mg grown on AlN epilayer, the I–V characteristics shown in Fig. 12(c) indicated that a p-type resistivity of around 2 Ω cm at 300 K has been attained [29,30], which is 4–5 orders of magnitude reduction compared to those of Mg doped AlN epilayers [96,98].

The growth of h-BN/n-$Al_xGa_{1-x}N$ (x~0.62) p-n junction heterostructures has also been carried out [29]. Fig. 13(a) shows the I–V characteristics and schematic illustration of a h-BN:Mg/$Al_xGa_{1-x}N$ (x~0.62) p-n junction structure. In addition to the need of thermal annealing treatment of the p-contacts, doping the buffer layer with Mg significantly improves the vertical transport properties. As can be seen from Fig. 13(a), a decent diode behavior has been demonstrated in h-BN:Mg/n-AlGaN p-n junctions [29]. Moreover, the leakage current under reverse bias can be controlled to be quite low (~3 μA at −10 V) [29]. However, practical p-n junction devices based on h-BN epilayers have not yet been realized as of today. We believe that key parameters to be further optimized are the growth and p-type doping conditions of the low temperature buffer layer. Since the low temperature buffer is of amorphous nature, the growth conditions of the buffer layer (a few nm) need to be further optimized to minimize its impact on the free hole injection in the DUV emitters.

More recently, AlGaN nanowire DUV LEDs using h-BN as a p-type current injection layer, as schematically shown in Fig. 13(b), have been successfully demonstrated [107]. It was shown that h-BN/n-AlN nanowire DUV LEDs significantly outperformed AlN p-i-n nanowire DUV LEDs [107]. Nevertheless, the nanowire h-BN/n-AlN DUV LED structures are Mg-dopant free, whereas the p-type conduction was attributed to the possible formation of native acceptor-like defects such as boron vacancies [107]. The observation of free holes in Mg-dopant free h-BN nanowires is in fact consistent with high temperature Hall-effect measurement results performed on an unintentionally doped thin h-BN epilayer grown at 1300 °C [91], which was shown to be naturally weak p-type at high temperatures (>700 K) with a measurable free hole concentration of about 3×10^{14} cm^{-3} and in-plane hole mobility of about 13 $cm^2/V{\cdot}s$, providing an in-plane p-type resistivity of ~1.6×10^3 Ω cm at 790 K [91]. The temperature dependent electrical resistivity of this undoped epilayers yielded an acceptor energy level of 0.68 eV above the valence band with a possible origin attributed to boron vacancies (V_B) or V_B related acceptor defect complexes (V_BX) [91]. Moreover, the carrier mobility and lifetime product (μτ) measurements conducted on an unintentionally doped thick h-^{10}BN epilayer deposited below 1400 °C revealed a larger μτ product for holes than for electrons, again implying that holes (electrons) behave like majority (minority) carriers in unintentionally doped h-BN [35]. Furthermore, a recent study on h-BN layers grown on graphene has revealed that the valence-band maximum in h-BN is located around the K point, 2.5 eV below the Fermi level, and hence also inferred the residual p-type character of typical h-BN [108]. These results seem to imply that, in terms of conductivity control, h-BN is more like diamond than other III-nitride semiconductors.

2.3. h-BN/SiC heterostructure

The synthesis of h-BN epilayers on highly conductive n-type 6H–SiC (0001) substrates has also been investigated [109]. Such heterostructures could allow for the construction of useful devices such as high sensitivity Schottky photodetectors and avalanche photodetectors, as demonstrated for AlN/n-SiC heterostructures [110,111]. The growth was carried out on n-type 6H–SiC (0001) on-axis substrate. The (0001) surface of SiC was the Si terminated surface. The electrical resistivity of the 6H–SiC substrate used was around 0.01 Ω cm with a specified free electron concentration of 5×10^{18} cm^{-3} [109,110]. Prior to the growth of h-BN epilayer, a 20 nm BN buffer layer was first deposited on 6H–SiC substrate at 800 °C to provide strain relieve from lattice mismatch between the substrate and the subsequent h-BN epilayer as well as to enhance the adhesion of h-BN epilayer to the substrate. The growth temperature of h-BN epilayers was 1300 °C. The XRD θ-2θ scan of the h-BN/6H–SiC heterostructure revealed a h-BN (0002) reflection peak at 26.5°, providing a lattice constant of c = 6.70 Å. No other diffraction peaks were observed from h-BN, indicating that h-BN epilayers grown on SiC are of single h-phase [109].

Ohmic contact with a cross section area of about 9 mm^2 consisting of Ni (30 nm)/Au (120 nm) bilayer was deposited on the h-BN surface. Thermal treatment (rapid thermal annealing) at 1020 °C in a N_2 ambient atmosphere was used to decrease the contact resistance

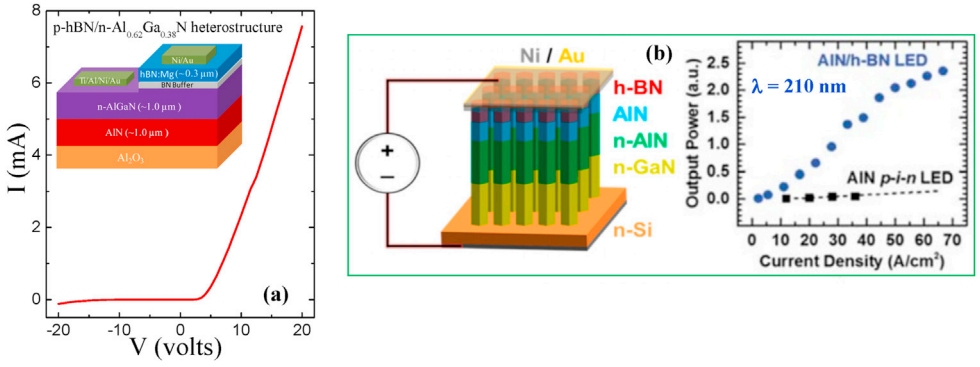

Fig. 13. (a) I–V characteristics and schematic illustration of a h-BN:Mg/n-$Al_{0.62}Ga_{0.38}N$:Si/AlN p-n heterostructure in which the buffer layer was doped with Mg and p-contacts were thermally annealed at 1020 °C for 1 min, exhibiting a diode behavior [Ref. 29; Credit: S. Majety, J. Li, X. K. Cao, R. Dahal, B. N. Pantha, J. Y. Lin, and H. X. Jiang, Appl. Phys. Lett. **100**, 061121 (2012)]. (b) (Left panel) Schematics of a 210 nm DUV LED fabricated from h-BN/n-AlN nanowire heterostructure. (Right) Comparison of L-I characteristics of h-BN/n-AlN nanowire LED and AlN p-i-n nanowire LED [Ref. 107; Credit: D. A. Laleyan, S. Zhao, S. Y. Woo, H. N. Tran, H. B. Le, T. Szkopek, H. Guo, G. A. Botton, and Z. Mi, Nano Lett. **17**, 3738 (2017)].

and enhance the Ohmic behavior of Ni/Au/h-BN contacts [28]. The sample was etched down to the n-SiC layer using inductively coupled plasma (ICP) dry etching and ohmic contact consisting of a layer of Ni (100 nm) was deposited on n-SiC followed by thermal annealing in a N_2 ambient at 950 °C for 100 s. The inset of Fig. 14(a) depicts the schematic layout of the structure with ohmic contacts on h-BN (Ni/Au) and n-SiC (Ni).

Fig. 14(a) shows the I–V characteristics of h-BN/n-SiC heterostructures [109]. A sharp increase in current occurs when the applied voltage is at the onset to produce a flat band condition across the heterointerface. By neglecting thermionic emission of electrons over the h-BN barrier, the voltage at I = 0, V_o, provides the magnitude of the built-in voltage at the heterointerface [112] and represents a close measure of the band offset for the h-BN/n-SiC heterostructure. By knowing that the Fermi level in n-type 6H–SiC is 0.3 eV [113] and the Fermi levels in 6H–SiC and h-BN lineup in the middle of the bandgaps in intrinsic materials, the band alignment for the intrinsic 6H–SiC/h-BN heterostructures can be deduced, as shown on Fig. 14(b), assuming the energy bandgaps of 6H–SiC and h-BN of 3.0 and 6.0 eV, respectively [109]. From Fig. 14(b), the valence and conduction band offsets are about ΔE_V ~0.7 ± 0.2 eV and ΔE_C ~2.3 ± 0.2 eV, respectively, giving a ratio of $\Delta E_C/\Delta E_g \approx 76\%$. The result shown in Fig. 14(b) implies that 6H–SiC/h-BN is a type I (straddling gap) heterojunction [109].

The band offsets between h-BN and AlN have been calculated using first principles calculations, which suggested that it is a type II (staggered gap) band alignment with ΔE_V ~0.67 eV and ΔE_C ~0.57 eV [109]. On the other hand, previous experimental measurements have yielded a conduction band offset of 1.9 eV for the AlN and 6H–SiC heterostructure [114]. Using these independent data, band alignments between h-BN, 6H–SiC and AlN, can be deduced, as shown in Fig. 14(c), from which a conduction band offset (ΔE_C) of 2.47 eV is deduced for the 6H–SiC/h-BN heterojunction. This value of ΔE_C (≈ 2.47 eV) obtained from independent experimental data [114] coupled with first-principles calculations agrees reasonably well with a value of ~2.3 eV deduced experimentally from the analysis of I–V characteristics of h-BN/6H–SiC heterostructure shown in Fig. 14(b). Due to the fact that the valence band of h-BN lies ~0.67 eV above that of AlN, h-BN would be superior over AlN as an electron blocking layer for DUV emitter applications because the use of h-BN electron blocking layer will not introduce a potential barrier for hole injection. This advantageous feature is illustrated in Fig. 11.

2.4. *Freestanding thick h-BN epilayers*

One of the most promising and demonstrated applications of h-BN so far is for solid-state neutron detectors [35–40,115–121]. The element Boron exists as two main isotopes, ^{10}B and ^{11}B in natural abundance of approximately 20% and 80%, respectively [122,123]. The element of ^{10}B is among a few isotopes which possesses a sizable interaction cross-section with thermal neutrons. Fig. 15(a) shows that ^{10}B has a capture cross-section (σ)of 3840 barn (=3.84×10^{-21} cm^2) for thermal neutrons (neutrons with an average energy of 25 meV), which is next to a value of σ~5330 b for a more common neutron detection material of He-3 [122]. Boron density in h-BN is 5.5×10^{22} cm^{-3} in which isotope ^{10}B is about 20% and isotope ^{11}B is about 80% in natural h-BN. Therefore, the density of isotope ^{10}B atoms in h-BN is $N = 1.1 \times 10^{22}$ cm^{-3}. From these, the microscopic neutron absorption coefficient (α) and absorption length (λ) in a natural h-BN epilayer are thus [118]:

$$\alpha_{natural} = N\,\sigma = 42.24\ \ cm^{-1} \ \text{ and } \ \lambda_{natural} = \frac{1}{\alpha_{natural}} = 2.37x10^{-2}\ cm = 237\ \mu m$$

where $\sigma = 3.84 \times 10^{-21}$ cm^2 is the capture cross-section of ^{10}B for thermal neutron [122]. This means that it will require h-BN detectors

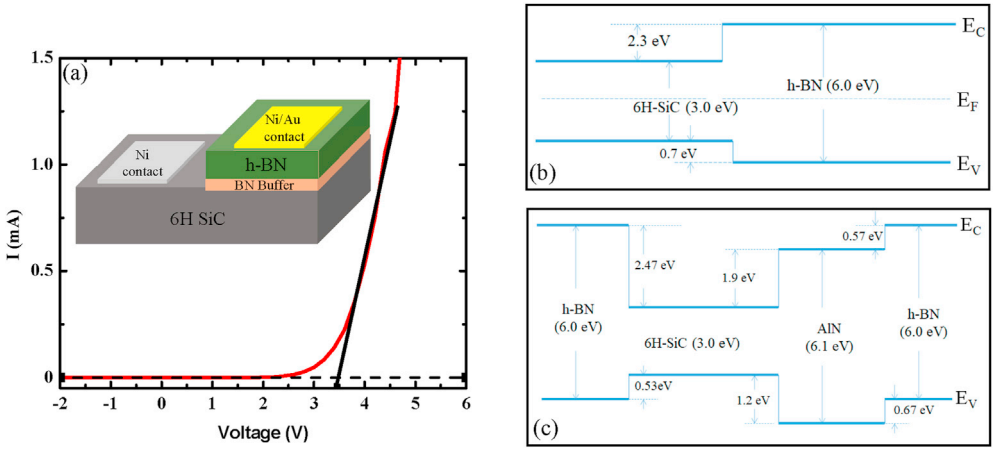

Fig. 14. (a) I–V characteristics of h-BN/n-6H–SiC heterostructures. The inset is a schematic diagram of the heterostructure used for the measurements. (b) Band alignment between intrinsic 6H–SiC and h-BN deduced from the I–V characteristic in (a). (c) Band alignments between intrinsic h-BN, 6H–SiC and AlN constructed from independent experimental data for AlN/6H–SiC heterojunction in Ref. 114 and first principles calculations for h-BN/AlN heterojunctions [Ref. 109; Credit: S. Majety, J. Li, W. P. Zhao, B. Huang, S. H. Wei, J. Y. Lin, and H. X. Jiang, Appl. Phys. Lett. **102**, 213505 (2013)].

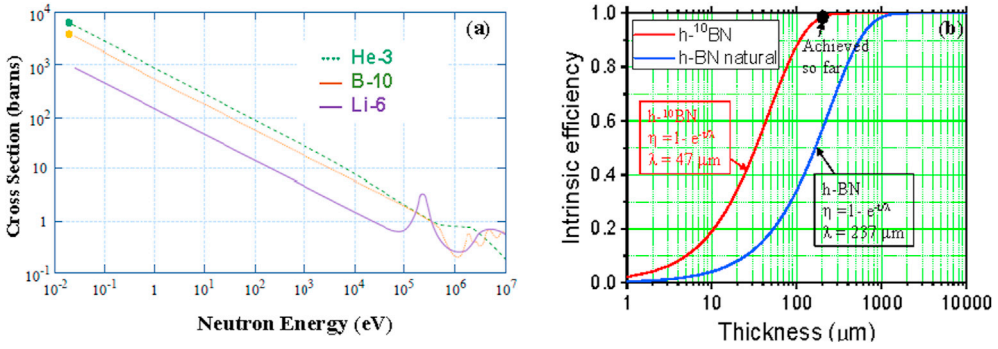

Fig. 15. (a) Neutron capture cross sections as functions of the kinetic energy of neutrons for He-3, B-10, and Li-6. The green and orange dots indicate, respectively, the cross sections of He-3 and B-10 for thermal neutrons (neutrons with an average energy of 0.025 eV) (Credit: MIT OpenCourseWare - https://ocw.mit.edu/courses/nuclear-engineering/22-106-neutron-interactions-and-applications-spring-2010/lecture-notes/MIT22_106S10_lec07.pdf - Slide 27). (b) Plot of Eq. (1): The theoretical thermal neutron detection efficiency a as function of the detector thickness for natural h-BN (blue curve) and 100% ^{10}B-enriched h-^{10}BN (red curve).

to have a layer thickness of 1λ (~237 μm) to attain a theoretical detection efficiency of 1-e^{-1} = 63%. It is evident that the most effective way to gain neutron detection efficiency is by isotopic enrichment of the source molecule, which can increase the neutron detection efficiency by a factor of 5 with little impact to semiconducting properties. For 100% ^{10}B-enriched h-BN, the absorption coefficient (length) will be a factor of 5 larger (smaller). Thus, we have

$$\alpha_{enriched} = 5\alpha_{natural} = 211.20\ cm^{-1} \text{ and } \lambda_{enriched} = \frac{1}{\alpha_{enriched}} = 4.73x10^{-3}cm = 47\ \mu m.$$

The thermal neutron absorption probability (P) or equivalently the theoretical (or intrinsic) detection efficiency (η) of h-^{10}BN detectors as a function the detector's layer thickness, *t*, can be expressed as

$$\eta = P(t) = 1 - e^{-t/\lambda}, \tag{1}$$

where λ is the thermal neutron absorption length with λ = 47 μm for h-^{10}BN and λ = 237 μm for h-BN. Eq. (1) is plotted in Fig. 15(b) for h-^{10}BN and h-BN [35], which shows that the efficiency of BN detectors can be increased by simply increasing the layer thickness. This is a huge advantage over He-3 gas detectors in which the enhancement in the detection sensitivity is achieved through increasing the gas pressure, tube diameter, and length.

Based on the working principles of ^{10}BN neutron detectors, one can see from Eq. (1) that the key to obtain a high intrinsic detection efficiency is to increase the layer thickness of ^{10}BN. In comparison to ^{3}He gas tubes, 100 μm thick h-^{10}BN detectors would be capable of providing an intrinsic detection efficiency of 88% for thermal neutrons, which exceeds the thermal neutron conversion efficiency of 77% for 1-inch diameter ^{3}He gas tubes pressurized at 4 atm. Nevertheless, achieving h-^{10}BN epitaxial layers with thicknesses large than 1λ (>47 μm) is necessary to bring the h-^{10}BN detector technology to a level which can start to compete with ^{3}He gas detector technology, but is a challenging task for MOCVD growth.

To obtain *h*-^{10}BN epilayers with large thicknesses, it is necessary to develop growth processes which would enable an increased growth rate over those for the typical epilayers, such as those shown in Fig. 5(a) of about 1.2 nm/min. One key is to increase the growth temperature to promote the surface mobilities of B and N atoms as well as to enhance the cracking efficiency of NH_3 to support nitrogen-rich growth conditions. As demonstrated in Fig. 8, increasing the growth temperature would enhance the crystalline quality. However, high growth temperatures and long growth times together with the use of sapphire substrate tend to incorporate oxygen impurities into h-BN epilayers during growth [37,39], which can have a deleterious impact on the charge collection efficiency of *h*-BN detectors. Therefore, there is an inevitable trade-off between these two factors. Because of the detrimental effects of oxygen impurities, finding an "optimal" growth temperature is necessary to ensure an adequate crystal quality while minimizing the density of oxygen impurities. However, the recently demonstrated successful growth of *h*-BN epilayers on AlN/sapphire templates at high temperatures may be applied to resolve this dilemma [64].

As schematically illustrated in Fig. 3, thick h-^{10}BN epilayers have been successfully produced using MOCVD on c-plane sapphire (Al_2O_3) substrates of 4-inches in diameter. Trimethylboron (TMB) with a vendor specified ^{10}B isotope enrichment of 99.9% and ammonia (NH_3) were used as the precursors for the growth of h-^{10}BN epilayers. The typical epi-growth temperature employed for producing thick h-^{10}BN epilayers is between 1400 and 1500 °C to obtain epilayers with high crystalline quality at relative high growth rates. Due to the unique layered structure of h-BN and the difference in thermal expansion coefficients between h-BN and sapphire substrate, a h-BN epilayer with a sufficient thickness (>20 μm) automatically separates from sapphire substrate during cooling down after growth, allowing the realization of a freestanding h-BN wafer as shown in Fig. 3. In contrast to h-BN thin epilayers, the use of low temperature buffer layers cannot prevent the self-separation of thick epilayers from sapphire substrates. The surface of thick h-BN films separated from sapphire substrate exhibits an excellent morphology with a typical RMS surface roughness value of 0.1–0.2 nm, comparable to those of thin films shown in the inset of Fig. 9(c). However, the surface morphology of the top h-BN epilayers becomes slightly

poorer with an increase in the h-BN layer thickness with a typical RMS surface roughness value of 1 nm for films with a thickness of 50 μm. As illustrated in Fig. 3(e), the largest thickness of h-^{10}BN epilayers attained so far is 200 μm, which based on Eq. (1) and Fig. 15(b), is capable to provide an intrinsic detection efficiency of 99% for thermal neutrons.

3. Photoluminescence emission properties

3.1. Unique features of h-BN

The unique features of *h*-BN in comparison with AlN are of immense interest for novel photonic device exploration, which can be briefly summarized below:

(a) *High optical emission and absorption.* The previously measured optical absorption of h-BN is as high as 7.5 × 10^5/cm for above bandgap photons [10,32].
(b) *2D vs. 3D*. Having a layered structure, *h*-BN is a quasi-2D material, whereas AlN is a 3D material.
(c) *Very large exciton binding energy* – The exciton binding energies is about 0.7 eV in *h*-BN "bulk" crystals [15–21] and 2.1 eV in *h*-BN monolayers [16].
(d) *TE vs TM mode*. Polarization-resolved PL measurements and theoretical calculations have determined that the band-edge emission in *h*-BN is predominantly transverse-electric (TE) polarized [19,20] in contrast to the well-known transverse-magnetic (TM) polarization in AlN [124–126].

As shown in Fig. 16(a)–(b), photoluminescence (PL) emission intensity of the band-edge transitions in *h*-BN epilayer is more than 2 orders of magnitude higher than that of AlN epilayer when the two samples are measured side-by-side for a direct comparison [19,20,32]. Notice that the 10 K PL spectrum of *h*-BN epilayer shown in Fig. 16(a) is multiplied by a factor of 1/500, whereas the 300 K spectra shown in Fig. 16(b) are multiplied by a factor of 1/10 for *h*-BN epilayer and by a factor of 10 for AlN epilayer, respectively. The observed PL emission spectral linewidths of *h*-BN at 10 K and 300 K are much wider than those of AlN. This is expected and consistent with the XRD results shown in Fig. 9, which revealed that the crystalline quality of AlN epilayer is superior to that of *h*-BN epilayer because the growth processes for AlN epilayers are more developed than those for *h*-BN epilayers at this stage. These results imply that *h*-BN deep UV devices potentially could be even more efficient than those based on AlN.

Fig. 16(c) compares the polarization-resolved band-edge PL emission spectra of *h*-BN and AlN epilayers measured at 10 K [19,20,32]. The PL emission spectral line shape for *h*-BN epilayer shown in Fig. 16(c) for the configuration with emission polarization along the crystal c-axis (E_{emi}//c) is like that in the (E_{emi}⊥c) configuration. However, the emission intensity is about 1.7 times stronger in the (E_{emi}⊥c) configuration, which is in sharp contrast to the polarization-resolved PL spectra of AlN epilayer [124]. The emission polarization of *h*-BN is more like GaN [124–126]. It is well established that the band-edge emission in $Al_xGa_{1-x}N$ alloys evolves from E_{emi}⊥c in

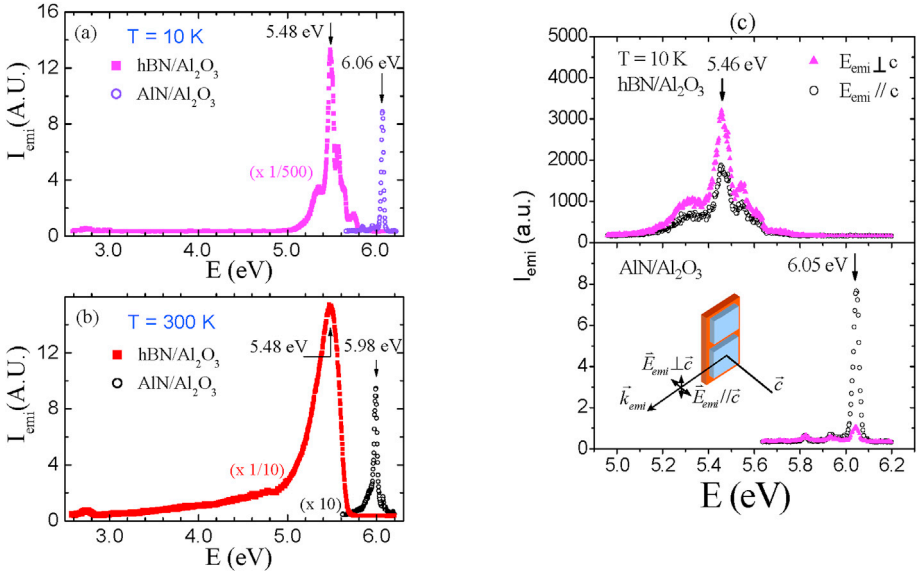

Fig. 16. Comparison of band-edge PL spectra of *h*-BN and AlN epilayers measured at (a) 10 K and (b) 300 K [Ref. 20; Credit: S. Majety, X. K. Cao, J. Li, R. Dahal, J. Y. Lin and H. X. Jiang, Appl. Phys. Lett.**101**, 051110 (2012)]. (c) Comparison of polarization-resolved low temperature (10 K) band-edge PL spectra of *h*-BN and AlN epilayers with emission polarization parallel (E_{emi}//c) and perpendicular (E_{emi}⊥c) to the c-axis, controlled through the use of a polarizer in front of the monochromator [Ref. 19; Credit: B. Huang, X. K. Cao, H. X. Jiang, J. Y. Lin, and S. H. Wei, Physical Review B **86**, 155202 (2012)].

GaN to E_{emi}//c in AlN [124] and that the band-edge emission in AlN is polarized along the c-axis, (E_{emi}//c), due to the nature of its band structure (the negative crystal-field splitting in AlN) [125,126]. This polarization property of AlN has a profound impact on the device applications. For instance, for UV LEDs using c-plane Al-rich $Al_xGa_{1-x}N$ alloys as active layers, the most dominant emission will be polarized along the c-axis (E_{emi}//c), which implies that UV photons can no longer be extracted easily from the surface [124]. Thus, device designs such as photonic crystals for enhancing the light extraction is beneficial for AL-rich AlGaN DUV LEDs [127,128]. Furthermore, in contrast to all conventional semiconductor laser diodes (LDs) with lasing output polarized in the TE mode, it was predicated [124] and experimentally verified [129] that lasing radiation from *c*-plane Al-rich $Al_xGa_{1-x}N$ based LDs is strongly polarized in the TM mode. In general, TE mode is preferred for LDs design because this mode is associated with a lower optical loss and lower threshold as well as with a higher optical gain and lasing beam quality. Thus, the observed predominant ($E_{emi}\perp c$) polarization of the band-edge emission in *h*-BN is an advantageous feature over AlN for DUV light emitting device applications.

3.2. Origin of strong optical transitions in h-BN

Using group theory analysis and first-principles calculations [19], it was shows that the strong optical transitions in h-BN originates predominantly from the unusually strong $p \rightarrow p$-like transitions and its "2D" nature. Due to the weak van der Waals interaction and large distance (3.33 Å) between each layer in h-BN, the interlayer optical transitions are much weaker than those of single-layer transitions, e.g., the strengths of the $\pi \rightarrow \pi^*$ transitions between two neighboring layers are only ~20% of those in the same layer [19]. As a result, the optical properties of h-BN are similar to those of 2D single layer BN shown in Fig. 17(a), which are mostly determined by the "2D" nature of h-BN and strong "single-layer" $p \rightarrow p$ transitions at the absorption edge. The calculated imaginary part of the dielectric response function, $\varepsilon_i(\omega)$, of h-BN and AlN as a function of the polarization of the light is shown in Fig. 17(a). Compared to AlN, the calculation results revealed that h-BN has a greatly enhanced absorption or luminescence intensity at the absorption edge, consistent with experimental results shown in Fig. 16(a)–(b). Furthermore, the calculation results revealed that the absorption (peak) intensity along the ($E\perp c$) direction is significantly larger than that of (E//c). However, the case is opposite for AlN, where the optical transition is forbidden along ($E\perp c$), due to the negative crystal field-splitting [125,126], as shown in Fig. 17(a). The calculation results are consistent with the experimental observations shown in Fig. 16(c).

The PL emission results shown in Fig. 16 inferred a very large oscillator strength and high density of states (DOS) near the absorption edge. It is interesting to note that *h*-BN is the only quasi-2D inorganic semiconductor with such a large energy bandgap. The 2D nature of layer structured *h*-BN can also result in an increase in the exciton binding energy and oscillator strength over the 3D systems [15–19]. A GW plus Bethe-Salpeter equation (GW + BSE) calculation with including the excitonic effect was carried out to obtain the optical spectrum of h-BN and w-AlN [19]. As shown in Fig. 17(b), the excitonic effects are more significant in h-BN than in 3D w-AlN, which red shifts the transition energy of h-BN to a lower energy position, with a high-intensity peak at 5.72 eV. Compared to the minimum direct

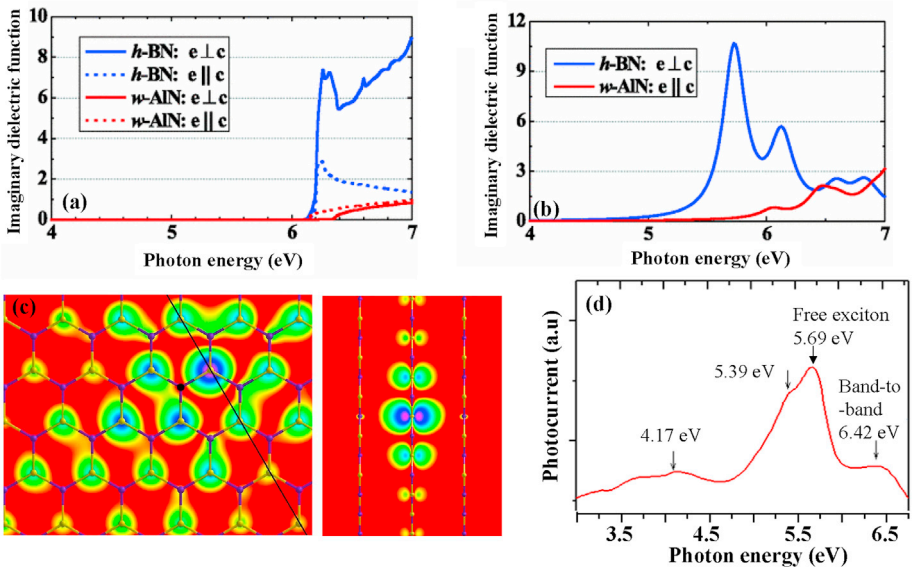

Fig. 17. (a) Calculated imaginary dielectric function, $\varepsilon_i(\omega)$, of h-BN and w-AlN as a function of photon energy, yielding a minimum direct GW band gap of 6.48 eV. (b) Calculated $\varepsilon_i(\omega)$ of h-BN and w-AlN obtained from the GW plus Bethe-Salpeter equation calculations, including the excitonic effect, yielding an exciton binding energy of E_x ~ 0.76 eV [Ref. 19; Credit: B. Huang, X. K. Cao, H. X. Jiang, J. Y. Lin, and S. H. Wei, Physical Review B **86**, 155202 (2012)]. (c) Two-dimensional projections of the exciton probability of a low-lying exciton state in h-BN. The self-energy correction calculation yielded a minimum direct gap of 6.47 eV and an exciton binding energy of E_x ~0.72 eV [Ref. 15; Credit: B. Arnaud, S. Lebègue, P. Rabiller, and M. Alouani, Phys. Rev. Lett., **96**, 026402 (2006). (d) Room temperature photocurrent excitation spectrum of a 30 nm thick *h*-BN epilayer, providing a minimum direct band gap of 6.42 and an exciton binding energy of E_x ~ 0.73 eV [Ref. 21; Credit: T. C. Doan, J. Li, J. Y. Lin, and H. X. Jiang, Appl. Phys. Lett. **109**, 122101 (2016)].

GW band gap of 6.48 eV in h-BN shown in Fig. 16(a), the exciton binding energy is estimated to be ~0.76 eV [19], which are very consistent with the results of a previous calculation [15]. Obviously, this high-intensity excitonic peak is mainly contributed by the high-intensity of electron-hole pairs originating from the "2D" optical nature of h-BN, giving rise to large enhanced optical transition rate at the absorption edge compared to AlN.

The previously measured band-edge optical absorption coefficient (α) of *h*-BN is unusually high (~7.5×10^5 cm^{-1}) [10] and is more than 3 times higher than that of AlN (~2×10^5 cm^{-1}) [130]. This strong optical absorption property can also be understood by simply writing the optical absorption (I/I_0) as $I/I_0 = 1\text{-}e^{-t/\lambda}$ [32,82]. Here λ is the optical absorption length and *t* the h-BN epilayer thickness. On the other hand, since t/λ «1 holds for very thin epilayers, the optical absorption can be reduced to $I/I_0 \approx t/\lambda$. If we adopt the concept of optical absorption of graphene, which states that its absorption is $\pi e^2/\hbar c = \pi\alpha = 2.3\%$, with $\alpha = e^2/\hbar c$ being the fine structure constant [131] and assume the same holds for the above bandgap optical absorption in *h*-BN, we then have the optical absorption of *h*-BN = 2.3% per layer (3.33 Å). This implies that $I/I_0 \approx (t/\lambda) = 0.023$ for t = 3.33 Å. This gives the optical absorption length (λ) and absorption coefficient (α) for the above bandgap photons in h-BN as,

$\lambda = t/0.023 = 3.33$ Å$/0.023 = 144.8$ Å; $\alpha = 1/\lambda = 1/144.8$ Å $= 6.9 \times 10^{-3}$/Å $\approx 7 \times 10^5$/cm

This estimated value of $\alpha = 7 \times 10^5$/cm for the above bandgap optical absorption coefficient based on the optical absorption concept of graphene agrees exceptionally well with the previously measured value of 7.5×10^5/cm [10]. This implies that only a very thin layer of *h*-BN with approximately 70 nm (~5λ) in thickness will absorb all incoming above bandgap photons. This together with its inherent 2D nature of layered structure makes *h*-BN to possess exceptionally strong optical transitions near the absorption edge.

Previous calculation results [15–17] and the results shown Fig. 17(a)–(b) [19] demonstrated a huge exciton binding energy (E_x ~ 0.7 eV) in h-BN due to its low dielectric constant and layered structure. This is more clearly illustrated in Fig. 17(c), where a 2D projection of the probability of a low-lying exciton state with hole localized slightly above a nitrogen atom is shown [15]. The left panel shows that the electron is delocalized on boron atoms and that the probability of finding the electron on a boron atom is maximum for the nearest neighbors of the nitrogen atom where the hole is localized [15]. The right panel shows that the electron is confined within the layer where the hole is located. The results revealed that low-lying excitons in h-BN belong to the Frenkel class because electron–hole pairs in *h*-BN form very tightly bound excitons and are tightly confined within the layers with a binding energy of E_x ~0.72 eV [15].

Experimentally, from the temperature dependence of the exciton decay lifetime, an exciton binding energy of E_x ~740 meV and small exciton Bohr radius of ~8 Å have been deduced [18]. More recently, photocurrent excitation spectroscopy has also been utilized to directly probe the fundamental band parameters of *h*-BN [21]. Fig. 17(d) shows a room temperature photocurrent excitation spectrum of a metal-semiconductor-metal (MSM) photodetector fabricated from a 30 nm thick h-BN epilayer with metal strips width of 6 μm and spacing between the metal strips of 9 μm biased at 100 V, from which the band-to-band, free excitons, and impurity bound excitons have

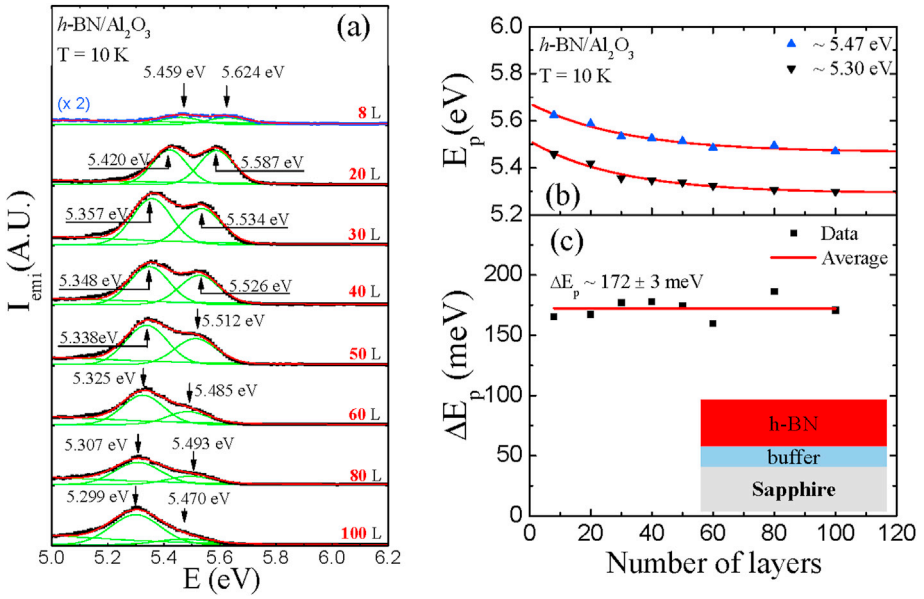

Fig. 18. (a) 10 K PL spectra of h-BN epilayers with varying number of layers. The energy peak positions of the dominant emission lines are near ~5.30 and 5.47 eV in the 100-layer h-BN epilayer. (b) The layer number dependence of the energy peak positions of the dominant emission lines near 5.30 and 5.47 eV. The symbols are data points and solid curves are the least squares fit with $E_p(N) = E_p(\infty) + [E_p(1) - E_p(\infty)]\exp\left(-\frac{N-1}{B}\right)$ The fitted values for the emission line near 5.30 eV are E_p (1) = 5.506 ± 0.010 eV, E_p (∞) = 5.292 ± 0.005 eV and B = 29.6 ± 5.3 L. The fitted values for the emission line near 5.47 eV are E_p (1) = 5.668 ± 0.018 eV, E_p (∞) = 5.466 ± 0.013 eV, and B = 30.9 ± 7.1 L. (c) The energy separation between the two dominant emission lines (ΔE_p) as a function of the layer number measured at 10 K [Ref. 95; Credit: X. Z. Du, M. R. Uddin, J. Li, J. Y. Lin, and H. X. Jiang, Appl. Phys. Lett. **110**, 092102 (2017).

been directly observed. Photocurrent excitation spectrum effectively records the increase in the free carrier concentration (electrons and holes) due to photoexcitation from different energy states [21]. For instance, the free exciton transition peak in the spectrum is formed through the processes of resonant excitation of free excitons (absorbing photons with an energy equals to that of the free exciton transition) and subsequent dissociation of a fraction of excitons into free carriers in the presence of an applied electric field [21]. The observed transition peaks yielded a minimum direct bandgap at room temperature of E_g~6.42 eV and an exciton binding energy of E_x~0.73 eV [21]. The values of the minimum direct bandgap and exciton binding energy measured from the photocurrent excitation spectroscopy shown in Fig. 17(d) agree reasonably well with those of calculations [15–17,19]. The exciton binding energy in h-BN is at least one order of magnitude larger than those in other inorganic semiconductors. The reported values of E_x for AlN (ranging from 60 to 80 meV) were previously considered to be exceptionally large [132–134]. The consequences of this large E_x value on the optical transitions in *h*-BN yet to be fully explored; the oscillator strength of small Bohr radius exciton can be very huge (on the order of unity) due to the strong overlapping between electron and hole wavefunctions, thereby supporting strong optical transitions in *h*-BN.

3.3. Evolution of optical properties from 2D to bulk

The light-matter interactions in quasi-2D layer structured semiconductors are rich in novel phenomena. The optical absorption spectra of *h*-BN bulk, single sheet, and BN nanotubes have been previously calculated using many-body perturbation theory [16]. The results showed that the optical absorption spectral line shapes of bulk *h*-BN and 2D *h*-BN sheet are almost indistinguishable, but the optical absorption peak of *h*-BN single sheet is blue shifted by an amount of about 160 meV with respect to that of bulk *h*-BN [16].

One of the interesting questions arises is that at which thickness can we consider h-BN a 3D material. To answer this question, a set of *h*-BN epilayers with the layer number varying from 8 to 100 were grown by MOCVD on sapphire substrates for PL emission spectroscopy studies [95]. To calibrate the number of layers of *h*-BN which is defined as the epilayer thickness divided by the interlayer distance between *h*-BN sheets of 3.33 Å, a thick *h*-BN epilayer of 0.5 μm was grown and the thickness was directly determined via optical micrograph, from which the growth rate was derived. Based on the pre-determined growth rate, a set of samples with identical growth conditions but varying growth times were grown.

Fig. 18(a) shows 10 K PL emission spectra of the set of *h*-BN epilayers with varying number of layers grown under identical growth conditions, in which two dominant emission lines are clearly resolved around 5.30 eV and 5.47 eV in the PL spectrum of the thick *h*-BN sample (the 100-layer sample) [95]. The emission peaks exhibit a blue shift towards higher energies as the number of layers is decreased from 100 to 8. The evolutions of both emission peaks, E_p (N), with the layer number (N) are depicted in Fig. 18(b) and can be described by, $E_p(N) = E_p(\infty) + [E_p(1) - E_p(\infty)]\exp(-(N-1)/B)$, where $E_p(1)$, $E_p(N)$, and $E_p(\infty)$ denote, respectively, the emission peak positions of 1-layer, N-layer, and bulk *h*-BN, B is a fitting parameter which describes an exponential dependence of $E_p(N)$, and the quantity $[E_p(1) - E_p(\infty)]$describes the total amount of energy peak shift as the dimensionality of *h*-BN scales from bulk to monolayer [95]. The fitting results yielded $[E_p(1) - E_p(\infty)] = 0.21\ eV$ for both emission peaks and a value of B = 30 layers. However, the predicted energy bandgap was expected to increase by ~1.2 eV from bulk to monolayer *h*-BN [16].

The energy peak position difference between these two emission lines, $\Delta E_P = E_{P,\ 5.47\ eV}(N) - E_{P,\ 5.30\ eV}(N) \approx 172 \pm 3$ meV, is independent of N and coincides well with the measured E_{2g} vibration mode in h-BN epilayers which has an energy of 172 meV ($\Delta\sigma = 1370\ cm^{-1}$) as shown in the Raman spectrum of Fig. 10(a). On the other hand, the emission line near 5.3 eV has been identified to be a *q*-DAP transition in both bulk *h*-BN [83] and thick *h*-BN epilayers [81]. Therefore, the emission lines at ~5.30 and 5.47 eV can be assigned to a *q*-DAP transition and its one E_{2g} phonon replica, respectively. In such a context, the observed $[E_p(1) - E_p(\infty)] = 0.21\ eV$ of the q-DAP emission can be attributed to the variations in the activation energies of the involved donor and acceptor. The activation energy of the acceptor involved in the *q*-DAP transition increased only by ~1.6 times as the dimensionality of *h*-BN reduces from thick layer to monolayer due to its deep level nature [95]. Nevertheless, by inspecting the results of Fig. 18(b) and the fitting parameter B = 30 layers, one can conclude that 90 layers (or 30 nm thick) of h-BN can be considered as a "bulk" 3D material.

3.4. Probing the temperature dependence of the energy bandgap

The spectral peak positions (E_p) of the near band-edge transitions in most semiconductors generally exhibit redshifts with increasing temperature and the temperature variation of E_p follows approximately the Varshni empirical equation describing the temperature dependent bandgap [135],

$$E_g(T) = E_g(0) - \alpha T^2/(\beta + T) \tag{2}$$

where $E_g(0)$is the energy bandgap at 0 K, α and β are the Varshni coefficients. Being a layered semiconductor, a previous theoretical work has indicated that the variation of E_g with temperature in *h*-BN is weak, attributing to the small indirect contribution of the lattice constant to the ionicity through crystal-field screening effects [9]. Additionally, the excitonic emission lines in *h*-BN generally exhibit complex features [14,18], whose linewidths tend to be broadened and emission intensities drop rapidly at higher temperatures. These together make the analysis of the general behavior of E_g vs. T in *h*-BN challenging.

It was observed that the energy positions of the q-DAP emission line and its one E_{2g} phonon replica in multi-layer *h*-BN shown in Fig. 18 exhibit a systematic dependence on temperature, which provided an opportunity to study the E_g vs T relation in *h*-BN [136]. More specifically, the temperature dependence of the q-DAP emission line and its one E_{2g} phonon replica in a 20-layer *h*-BN epilayer has been probed and the results are presented in Fig. 19(a) [126]. The emission peaks (E_p) of the q-DAP transition and its one E_{2g} phonon replica (at 5.420 eV and 5.587 eV at 10 K, respectively) are clearly resolved at different temperatures. However, both emission peaks

exhibit a very unusual temperature dependence. For a clear presentation, Fig. 19(b) plots the evolution of E_p with temperature for the zero-phonon line (ZPL) (the emission line with a peak position at 5.42 eV at 10 K), which revealed two different temperature regions. E_p first exhibits a downshift with increasing temperature up to 100 K and then upshift with increasing temperature above 100 K. This temperature dependence is different from the common behavior observed in most other semiconductors including GaN and AlN [137] as well as in *h*-BN nanotubes [138].

For a DAP transition, neglecting the Coulomb's interaction between donors and acceptors, its emission energy peak position can be described as $E_p = h\nu = E_g - E_D - E_A$, where E_D and E_A are the energy levels of the involved donor and acceptor, respectively. Using the Varshni's equation of Eq. (2) for E_g and neglecting the temperature dependence of E_A and E_D, the peak position E_p of the ZPL can be written as, $E_p(T) = E_g(0) - E_D - E_A - \alpha T^2/(\beta + T)$. Therefore, the temperature evolution of E_p is expected to mimic that of E_g Ref. [136]. In general, two dominant mechanisms are responsible for the energy bandgap variation of a semiconductor: (1) lattice constant enlargement with temperature and (2) electron-phonon interaction. In Fig. 19(b), the solid curves are the least squares fitting of data with Eq. (2), however, in two different temperature regions. In the region of T < 100 K, E_g vs T (or E_p vs T) follows the anticipated trend, i.e., the bandgap decreases with increasing temperature and the temperature coefficient α is positive. The fitted value of α is 8.6×10^{-4} eV/K and β is 369 K. The fitted value of α/β is 2.33 μeV/K^2, which is larger compared with 1.28 [137], 1.06 [137], and 0.912 μeV/K^2 [139] for AlN, GaN, and InN, respectively, whereas the value of β is associated with the Debye temperature of the crystal. The results are an indication of a stronger electron-phonon interaction in *h*-BN in comparison with other III-nitride semiconductors due to its layered structure [136].

However, E_p surprisingly increases with increasing temperature at T > 100 K, a behavior which is distinctively different from most semiconductors. As a semiconductor with layered structure, the interaction between layers of *h*-BN is through van der Waals force, which is very weak in comparison with in-plane interaction. As such, E_g of *h*-BN is predominantly determined by the energy difference between electrons localized on B and N atoms [139]. Therefore, the temperature dependent E_g of *h*-BN at T > 100 K can be attributed primarily to the in-plane lattice constant (*a*) change with temperature. The *a*-lattice constants of *h*-BN at different temperatures have been previously measured [140] and the results are shown in Fig. 19(c), which revealed that the in-plane lattice constant expands slightly with increasing temperature at low temperatures and then decreases with increasing temperature from ~70 to 300 K [140]. The calculated values of the in-plane thermal expansion coefficients of *h*-BN, α_a, plotted in Fig. 19(c) showed that they are positive at low temperatures, become negative at temperatures above ~ 60 K and is almost constant of about -2.7×10^{-6} K^{-1} from 150 to 300 K [140]. These results clearly demonstrated that the temperature dependence of E_g above 100 K is dominated by the unusual effect of reduction in the *a*-lattice constant at higher temperatures. The slope of E_p versus T is about 0.43 meV/K from 100 to 300 K as fitted by Eq. (2), which means that the temperature coefficient of E_g, or the Varshni coefficient $\alpha = -0.43$ meV/K [136].

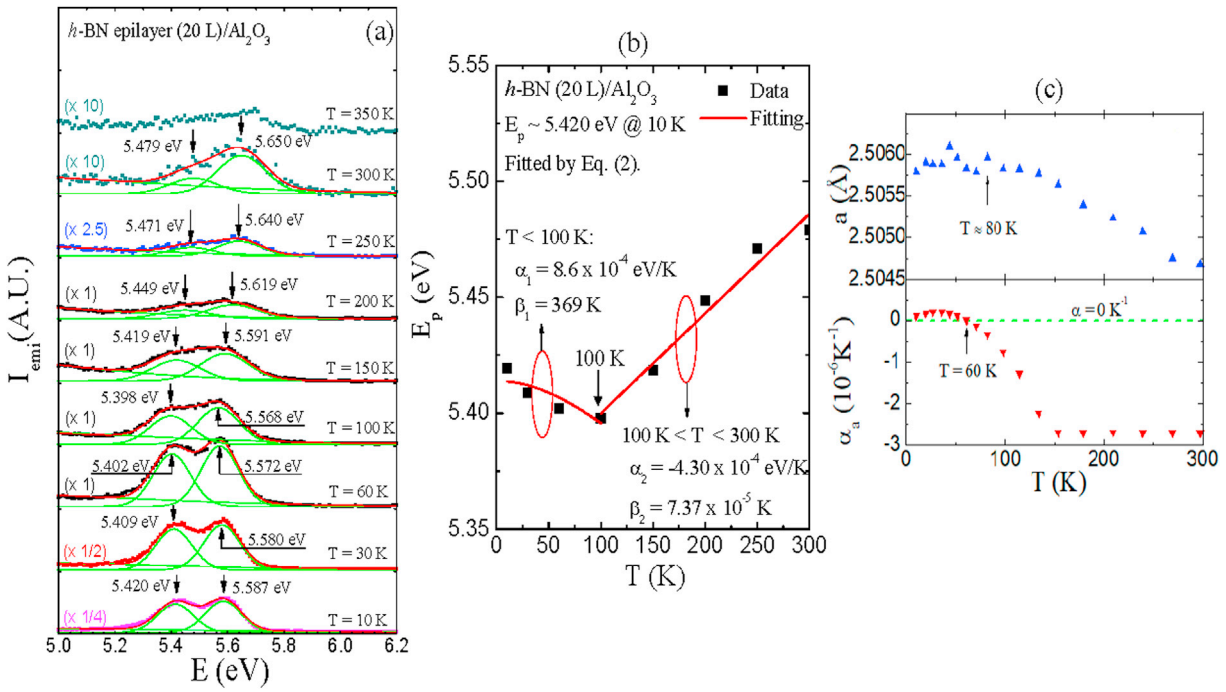

Fig. 19. (a) Near band-edge PL spectra of a 20-layer *h*-BN epilayer measured at different temperatures. (b) Temperature dependence of the energy peak position of the zero-phonon emission line (~5.420 eV @ 10 K) observed in a 20-layer *h*-BN fitted with Varshni's formula of Eq. (2) [Ref. 136; Credit: X. Z. Du, J. Li, J. Y. Lin, and H. X. Jiang, Appl. Phys. Lett. **111**, 132106 (2017)]. (c) Variations with temperature of in-plane *a*-lattice constant obtained experimentally (top panel) and calculated thermal expansion coefficient of *h*-BN (bottom panel) [Ref. 140; Credit: W. Paszkowicz, J. B. Pelka, M. Knapp, T. Szyszko, and S. Podsiadlo, Appl. Phys. A**75**, 431 (2002)].

In comparison, in the case of *h*-BN nanotubes, the excitonic emission peak exhibits a universal downshift in energy with increasing temperature in the entire temperature range of 10–800 K [138], in contrast with the results obtained for thin *h*-BN epilayers. It is interesting to compare the situation in suspended carbon nanotubes [141,142], in which the effective energy bandgap shifts down with increasing temperature due to the dominant electron-phonon coupling effect, despite the fact that the thermal expansion of graphite has a negative coefficient in the same temperature range. Hence, the temperature dependence of the bandgap of *h*-BN nanotube [138] most likely follows a similar trend as that of carbon nanotubes and is dominated by the electron-phonon coupling in the entire temperature range. Although both graphite and *h*-BN epilayers have negative thermal expansion coefficients in a broad temperature range, graphite has a zero-energy bandgap, which makes *h*-BN a unique semiconductor to exhibit this unusual temperature dependence of the energy bandgap.

3.5. *Nature of impurities in h-BN*

Nitrogen vacancies (V_N) and carbon impurities occupying the nitrogen sites (C_N) are two common impurities in *h*-BN [70–78]. The growth of thin *h*-BN epilayers by MOCVD under different NH_3 flow rates has been carried out to probe via PL emission spectroscopy the roles of V_N [80,81]. The PL emission spectra shown in Fig. 7(a) revealed broad impurity emission peaks near 3.9 eV, which were attributed to a donor-acceptor pair (DAP) transition (ZPL at 4.12 eV and its phonon replicas at 3.92 and 3.72 eV) [83–85]. As shown in Fig. 7, there are two other emission lines around 5.3 eV and 5.5 eV in the samples grown under low NH_3 flow rates (between 0.3 up to 1.0 SLM). These emission lines have been assigned to a q-DAP transition and a bound exciton transition, respectively [14,20,70,83–87]. Because the emission intensities of the impurity related transition lines (DAP, q-DAP, and bound exciton transitions) reduce continuously with an increase of the NH_3 flow rate, it was believed that the observed impurity emission lines below 5.7 eV are most likely related to V_N or impurities related to V_N such as carbon impurities occupying the nitrogen sites [80,81].

The temperature-dependence of the DAP emission with its ZPL near 4.1 eV and its LO phonon replicas near 3.9 and 3.7 eV shown in Fig. 7 has been measured from 10 K to 800 K for a sample grown at 1350 °C under 1.5 SLM NH_3 flow rate [80]. An Arrhenius plot of the integrated PL intensity of the DAP emission is shown in Fig. 20(a), which provided an activation energy of ~0.1 eV for the shallow impurity involved in this DAP transition. Assuming a minimum direct bandgap value of ~6.5 eV [15–19,21], the energy level of the deep impurity level involved in the DAP transition can be deduced to be $E_A = E_g - E_{shallow} - h\nu_{emi} \approx 6.5$ eV–0.1 eV–4.1 eV ≈ 2.3 eV, by neglecting the Coulomb interaction between ionized donors and acceptors. The measured energy levels together with previous theoretical insights on the formation energies of the impurities and defects in *h*-BN suggest that V_N and C_N, respectively, are the most probable donor and deep acceptor impurities involved in the DAP transition near 4 eV.

Moreover, assuming the *q*-DAP emission line near 5.3 eV also involves the same V_N donors, the energy level of the involved deep impurity can be deduced from $E_A = E_g - E_{shallow} - h\nu_{emi} \approx 6.5$ eV–0.1 eV–5.3 eV = 1.1 eV. Previous theoretical studies have indicated that a substitutional C_N could induce two deep defect levels [76,77]. With the presence of a deep level of about 1.1 eV, it should be possible to directly observe a band-to-impurity type transition by measuring the PL emission spectra in the near IR region around 1.1 eV. This was indeed the case. As shown in Fig. 20(b), a rather broad weak emission line with its peak energy around 1.2 eV was observed in the *h*-BN epilayer grown under an NH_3 flow rate of 1.5 SLM. This emission peak is most likely corresponding to a band-to-impurity transition between the deep acceptor involved in the *q*-DAP transition and the valence band. As shown in Fig. 7(b), the energy peak position of the free exciton emission line observed in the same set of *h*-BN epilayers is at 5.735 eV, which implies that the binding energy of the bound exciton (E_{BX}) related to the 5.5 eV emission line can be estimated to be around $E_{BX} \sim 0.24$ eV. Based on Haynes' rule, the binding energy of a bound exciton is about 10% of the impurity binding energy, neglecting the central cell correction. This suggests that the energy level of the impurity involved in the bound exciton transition near 5.5 eV is around 2.4 eV, which is very close to a value of 2.3 eV for the energy level deduced for C_N involved in the DAP transition near 4.0 eV. Therefore, it is highly plausible that the bound exciton emission line is due to the recombination of excitons bound to C_N deep acceptors (A^0, X), or I_1 type transition. We speculate that carbon impurities

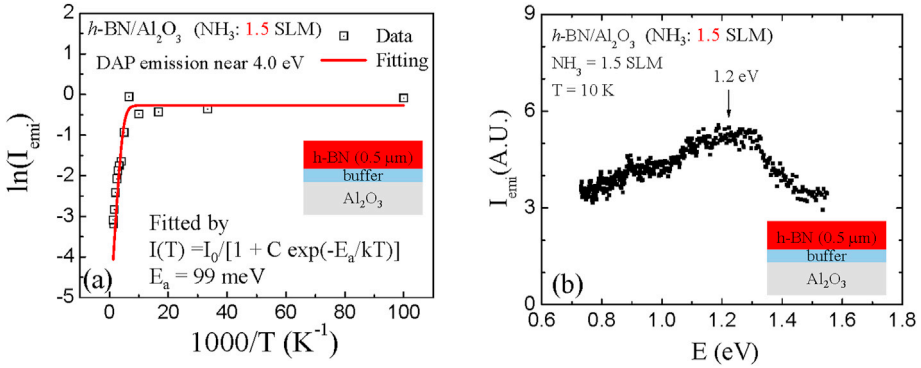

Fig. 20. (a) Arrhenius plot of the integrated PL emission intensity of the DAP transition near 4.1 eV in an *h*-BN epilayer grown under 1.5 SLM NH_3 flow rate [Ref. 80; Credit: X. Z. Du, J. Li, J. Y. Lin, and H. X. Jiang, Appl. Phys. Lett. **106**, 021110 (2015)]. (b) PL spectrum of an *h*-BN epilayer grown under 1.5 SLM NH_3 flow rate measured in the near infrared spectral region and an emission line near 1.2 eV was detected [Ref. 81; Credit: X. Z. Du, J. Li, J. Y. Lin, and H. X. Jiang, Appl. Phys. Lett. **108**, 052106 (2016)].

originate from the boron precursor (TEB source).

For the growth of thick h-^{10}BN epilayers, high growth temperatures (>1400 °C) and long growth times together with the use of sapphire substrates unavoidably introduce oxygen impurities into *h*-BN films due to oxygen diffusion from sapphire substrates. These oxygen impurities tend to act as substitutional donors (O_N) [79,88]. One of the most dramatic effects of oxygen impurity incorporation during high temperature growth was that the majority carrier type in h-BN epilayers changed from holes to electrons [88]. For epilayers grown at temperatures below 1400 °C, the mobility and lifetime (μτ) products of holes are larger than those of electrons, whereas the μτ products of electrons are larger than those of holes in thick epilayers grown at high temperatures above 1500 °C [88]. Fig. 21 compares the room temperature PL emission spectra of two *h*-BN epilayers of about 50 μm in thickness, with one grown at a temperature of 1400 °C and another at 1500 °C [88]. The sample grown at 1400 °C consists of a dominant broad transition peak at 3.9 eV, which is thought to have the same physical origin as the DAP transition peak superimposed within its LO phonon replicas covering from 3.7 to 4.1 eV, resulting from the recombination between V_N donor and C_N deep acceptor shown in Fig. 7(a) [80]. However, a new transition peak near 3.4 eV is clearly visible in the sample grown at a high temperature of 1500 °C. This transition peak also has a very board linewidth like the DAP transition peak near 3.9 eV, which suggested that this new 3.4 eV emission can also be attributed to a DAP transition involving donor of O_N [88]. From the energy difference between 3.9 eV and 3.4 eV and assuming the involved acceptor being the same C_N, the O_N donor involved in the 3.4 eV transition is expected to be about 0.5 eV deeper than the shallow V_N donor. Since the measured energy level of the involved donor, most likely V_N, in the DAP transition near 3.9 eV is about 0.1 eV as shown in Fig. 20(a) [80], the PL results shown in Fig. 21 therefore implied that the energy level of O_N donors in h-BN is about 0.6 eV. The dark current characteristics were measured at different temperatures to deduce the temperature dependent electrical resistance of the same 50 μm thick sample grown at 1500 °C, as shown in Fig. 21(b). The Arrhenius plot of the measured resistance provided an activation energy for O_N donors of 0.56 eV, which is in reasonable agreement with the value deduced from the PL results shown in Fig. 21(a).

With the estimated energy levels of the dominant impurities involved, an energy diagram illustrating the optical processes of the DAP and q-DAP transition lines observed in thin h-BN epilayers grown below 1400 °C shown in Fig. 7 and the DAP transition involving O_N donors in thick h-BN epilayers grown at high temperatures shown in Fig. 21(a) can be proposed, as depicted in Fig. 21(c). These results demonstrated that by monitoring the impurity related PL emission peaks in *h*-BN while varying the growth conditions, it is possible to obtained epilayers with reduced defect densities.

3.6. *Metal-semiconductor-metal photodetectors*

Photodetectors based on metal-semiconductor-metal (MSM) architecture with micro-strip interdigital fingers have been fabricated from *h*-BN epilayers [21,32,120]. The photolithography technique was used to pattern the interdigital fingers on the surface of *h*-BN epilayers. It was found that pattern transfer can be accomplished more effectively using a sulfur hexafluoride (SF_6) gas-based inductively

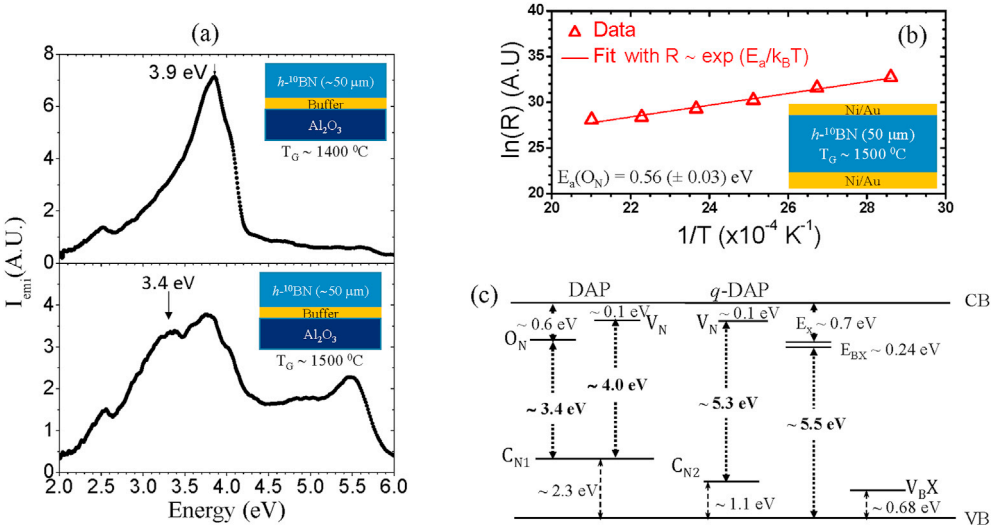

Fig. 21. (a) Room temperature PL spectra of 50 μm thick *h*-^{10}BN epilayers deposited on sapphire by MOCVD at different growth temperatures: T_G ~1400 °C (top) and T_G ~1500 °C (bottom); the insets show schematics of the *h*-^{10}BN epilayers [Ref. 88; Credit: S. J. Grenadier, A. Maity, J. Li, J. Y. Lin, and H. X. Jiang, Appl. Phys. Lett. **112**, 162103 (2018)]. (b) The temperature dependence of the dark resistance (in the Arrhenius plot) of a freestanding *h*-^{10}BN sample grown at 1500 °C measured in the vertical direction (along the *c*-axis), providing a fitted activation energy for O_N donors of 0.56 ± 0.03 eV [Ref. 88; Credit: S. J. Grenadier, A. Maity, J. Li, J. Y. Lin, and H. X. Jiang, Appl. Phys. Lett. **112**, 162103 (2018)]. (c) Energy diagram illustrating possible optical processes of the widely observed DAP emission near 4.0 eV, q-DAP emission near 5.3 eV and bound exciton emission near 5.5 eV in *h*-BN shown in Fig. 7 as well as the observed DAP emission involving O_N seen in Fig. 21(a). The observed energy levels in Figs. 20 and 21(b) are utilized. The measured energy level of an acceptor like defect observed in an undoped h-BN epilayer [Ref. 91] possibly related to boron vacancy complexes (V_BX) is also indicated.

coupled plasma (ICP) dry etching [143,144] than those based on Cl-plasma chemistry developed for GaN and AlN [145]. As shown in Fig. 22(a), etch depths larger than 3.5 μm was achievable in just one photoresist deposition while still maintaining an excellent vertical etching profile using SF_6 [144]. The patterns were etched all the way to the sapphire substrate. Metal contacts consisting of bi-layers of Ti/Al were deposited by e-beam evaporation. Fig. 22(b) shows a micrograph of a representative MSM detector incorporating a 1 μm thick h-BN epilayer and having the widths of etched trenches and micro-strips of 4 μm and 4 μm, respectively [32]. A representative photo-spectral response of an *h*-BN photodetector is shown in Fig. 22(c), exhibiting a peak response at 217 nm and a sharp cut-off wavelength around 230 nm with virtually no detectable responses in the long wavelengths. These results indicate that the *h*-BN MSM devices performed well as deep UV photodetectors. However, the typical responsivity of h-BN based DUV photodetectors is 2–3 orders of magnitude lower than that those of AlN MSM photodetectors [146]. This phenomenon is most likely related to the exceptionally large exciton binding energy in h-BN.

One of the outstanding features of h-BN for detector and electronic applications is its high breakdown field, E_B. As shown in Fig. 23(a), a previous study has yielded $E_B = 7.94$ MV/cm for ultrathin h-BN layers mechanically exfoliated from bulk crystals [147]. To measure the breakdown field of h-BN epilayers, a freestanding h-BN of about 1.8 μm was obtained via mechanical release to form a vertical detector, as illustrated in the left panel of Fig. 23(b) [32]. The right panel of Fig. 23(b) shows the I–V characteristics of the released h-BN epilayer measured in the *c*-direction (out-of-plane), which reveals that the breakdown occurs at around 800 V. This translates to $E_B \sim 4.4$ MV/cm, which is lower than 7.94 MV/cm obtained from ultrathin h-BN layers exfoliated from bulk crystals probed in a micron scale, as illustrated shown in Fig. 23(a). This is expected because the released h-BN epilayer used for E_B measurement has a larger cross section area of ~ 4 mm^2 than the microcrystals used in a previous study [147]. As a larger cross section area contains more defects, the measured E_B value measured in a larger area device tends to be lower [111]. Additionally, h-BN epilayer released from sapphire contains an amorphous buffer layer and is not dislocation free. Nevertheless, the measured value of E_B of 4.4 MV/cm for h-BN epilayer is higher than a value of 4.1 MV/cm deduced for dislocation-free AlN epilayers [111]. Assuming the value of 7.94 MV/cm of ultrathin h-BN layers probed in micron scale approaches E_B value of intrinsic h-BN [147], these comparison results serve as a useful benchmark for further improving the material quality of h-BN epilayers.

4. BN epilayer neutron detectors

4.1. Understanding the charge collection efficiency

Based on Eq. (1) of intrinsic efficiency of a thin film neutron detector, $\eta = 1 - e^{-t/\lambda}$, the key for obtaining high intrinsic detection efficiencies is to realize h-^{10}BN epilayers with large thicknesses (t). Absorption of a thermal neutron by a ^{10}B atom induces the following nuclear reaction inside h-^{10}BN [122],

$$B + n = Li^{*}\ (0.84MeV) + \alpha^{*}\ (1.47MeV)\ [94\%\ excited\ \ state] \tag{3a}$$

$$B\ +\ n\ =\ Li\ (1.015\ MeV) +\ \alpha\ (1.777\ MeV)\ [6\%\ ground\ state] \tag{3b}$$

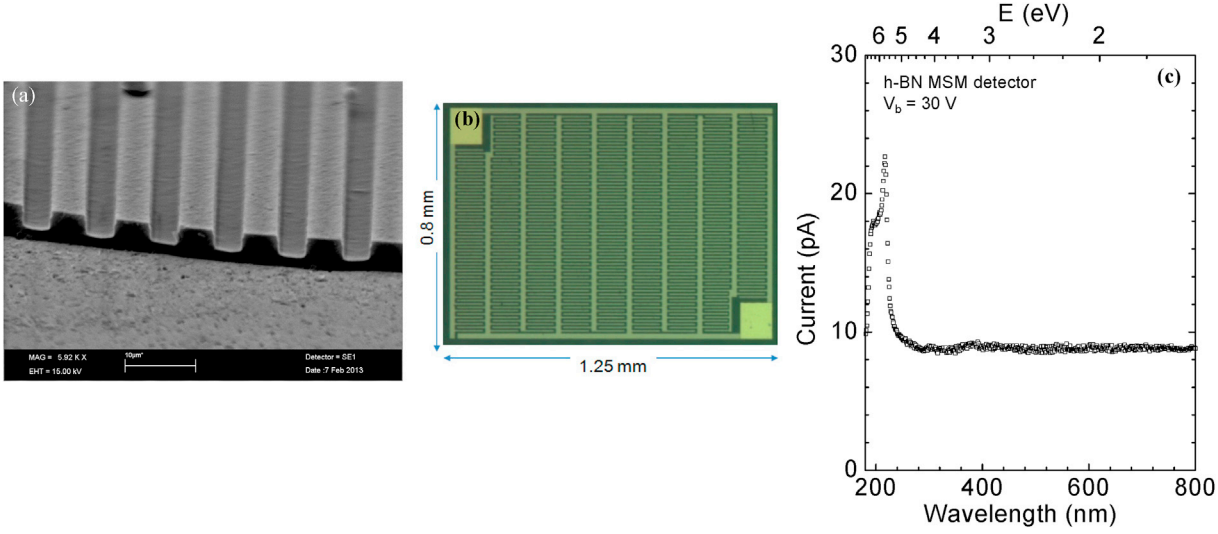

Fig. 22. (a) SEM image of the cross-section profile of an h-BN strip device etched in SF_6 [Ref. 144; Credit: S. Grenadier, J. Li, J. Y. Lin, and H. X. Jiang, J. Vac. Sci. Technol. A **31**, 061517 (2013). (b) Optical image of a representative fabricated h-BN metal-semiconductor-metal (MSM) detector. (c) The relative photo-spectral response of a fabricated h-BN MSM photodetector measured at a bias voltage of 10 V [Ref. 32; Credit: J. Li, S. Majety, R. Dahal, W. P. Zhao, J. Y. Lin, and H. X. Jiang, Appl. Phys. Lett. **101**, 171112 (2012)].

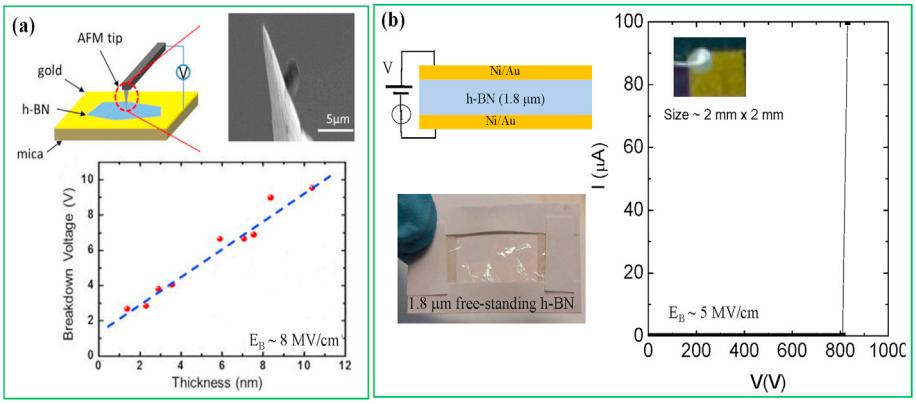

Fig. 23. (a) Breakdown field (E_B) of an ultrathin h-BN layer mechanically exfoliated from a bulk crystal grown by high temperature and high-pressure technique [Ref. 147; Credit: G. H. Lee, Y. J. Yu, C. Lee, C. Dean, K. L. Shepard, P. Kim, and J. Hone, Appl. Phys. Lett. **99**, 171103 (2011)]. (b) (Left) Schematic and photo of a freestanding h-BN epilayer released from sapphire substrate for breakdown field (E_B) measurement; (Right) Breakdown field (E_B) measured from a 1.8 μm thick freestanding h-BN epilayer and the insets show that the structure probed has a cross section area of 4 mm^2 [Ref. 32; Credit: J. Li, S. Majety, R. Dahal, W. P. Zhao, J. Y. Lin, and H. X. Jiang, Appl. Phys. Lett. **101**, 171112 (2012)].

$$\mathrm{Li},\ \alpha \rightarrow \mathrm{N}\ (e^{-}) + \mathrm{N}\ (h^{+}),\ \mathrm{N} \sim 10^{5} \tag{4}$$

Daughter particles (Li, α) created from the nuclear reactions possess large kinetic energies and travel inside the h-^{10}BN detector material, producing free electrons and holes which are collected by the electrodes with the aid of an external applied electric field, serving as a signature for neutron detection. Therefore, h-^{10}BN detectors are considered direct conversion detectors. If the thickness of the material is comparable or greater than the absorption length and the reaction takes place deep inside the material so that the drift lengths of the daughter particles (~2 μm and ~5 μm for *Li* and α, respectively [116]) are shorter than the depth of the reaction, then the total kinetic energy is converted into charge carriers. In contrast to ^{6}LiF [148–150] or ^{10}B [151–154] filled micro-structured semiconductor neutron detectors (MSND), the two sequential processes described in Eqs. (3) and (4) occur in the same h-^{10}BN epilayer. Therefore, h-^{10}BN detectors in principle are capable to provide higher detection efficiencies than those of indirect conversion devices. On the other hand, compare to other direct conversion neutron detectors based on amorphous B_4C [155], gadolinium complexes [156], pyrolytic, polycrystalline BN and alpha rhombahedral boron complexes [115,116,157], as demonstrated by XRD characterization results shown in Fig. 9, h-BN epilayers are single crystals and contain fewer charge traps and thereby allow a more rapid sweep-out of the electrons and holes generated by the nuclear reaction than amorphous, pyrolytic, or polycrystalline materials. However, to realize h-^{10}BN detectors with high detection efficiency, in addition to the necessary condition of a sufficiently large h-^{10}BN epilayer thickness, it is also essential to maximize the collection efficiency of charge carriers (electrons and holes) generated by the nuclear reaction, which demands epilayers with high crystalline quality and purity as well as novel device architecture designs.

The charge carrier collection processes in a detector under irradiation have been described via the classical Many's equation developed for insulating semiconductors, which takes into consideration of both the effects of surface recombination and bulk trapping [158],

$$I_i(V) = I_{0,i}[\eta_{c,i}(V)],$$

$$\eta_{c,i}(V) = \left[\frac{V\mu_i\tau_i\left(1 - e^{-\frac{W^2}{V\mu_i\tau_i}}\right)}{W^2\left(1 + \frac{s_i W}{\mu_i V}\right)}\right].\ (i = e,\ h). \tag{5}$$

Here $\eta_c(V)$ defines as the charge collection efficiency at an external bias voltage (V) applied between the two electrodes, I_0 is the saturation current, $\mu_h\tau_h$ ($\mu_e\tau_e$) and s_h (s_e) denote, respectively, the mobility-lifetime product and surface recombination velocity for holes (electrons), and W is the carrier transit distance or the distance between the two electrodes. To achieve a perfect charge collection efficiency, both the numerator term of $\frac{V\mu\tau}{W^2}\left(1 - e^{-\frac{W^2}{V\mu\tau}}\right)$ and the denominator term of $\frac{1}{\left(1+\frac{sW}{\mu V}\right)}$ in Eq. (5) must approach to 100%. This yields two basic conditions for attaining high charge collection efficiencies:

(a) $\frac{V\mu\tau}{W^2}\left(1-e^{-\frac{W^2}{V\mu\tau}}\right)\rightarrow 1$ or $\frac{W^2}{V\mu\tau}\left(=\frac{W}{\mu\tau E}\right)\ll 1$ *or* $\mu\tau E >>$ W. This condition states that the charge carrier drift length ($=\mu\tau E$) needs to be much larger than the carrier transit distance, *W*. This condition is predominantly determined by the bulk trapping properties as characterized by the numerator of Eq. (5), which provides a useful guidance on the achievable η_c at a given bias voltage for a detector material with a fixed carrier mobility and lifetime ($\mu\tau$) product [159].

(b) $\frac{1}{\left(1+\frac{sW}{\mu V}\right)}\rightarrow 1$ or $\frac{sW}{\mu V}\left(=\frac{s/\mu}{V/W}=\frac{Es}{E}\right)\ll 1$. This condition implies that the external applied electric field must be greater than the surface recombination field, $E >> Es\ (=s/\mu)$, in order to effectively sweep out charge carriers [159]. This condition is dominated by the surface effects described in the denominator of Eq. (5) and represents attainable η_c at a certain bias voltage at a given surface condition (or a surface recombination field) [159].

Inspecting conditions (a) and (b) for high charge collection efficiencies, obtaining h-^{10}BN epilayers with enhanced $\mu\tau$ is needed. In particular, increasing the carrier mobility (μ) would provide the greatest benefits for boosting the charge collection efficiencies because increasing μ would enhance the charge carrier drift length ($=\mu\tau E$) as well decrease the surface recombination field ($Es = s/\mu$). However, getting these improvements requires additional developments in the growth processes to further reduce the density of bulk defects, such as those identified in Fig. 21. Moreover, surface treatments techniques and device architectures for minimizing the surface recombination fields need to be further explored.

To illustrate the effects of bulk defects, $\mu\tau$ products and thermal neutron detection efficiency were characterized for photoconductive-like vertical detectors with varying device configurations [37]. These vertical detectors with a detection area of 1 × 1 mm^2 were fabricated from a 50 μm thick freestanding h-^{10}BN epilayer. Since the optical absorption length of the above bandgap photons in h-BN is only about 14.5 nm [32], most of the above bandgap photons are absorbed within about 70 nm (5λ) from the irradiated surface. As such, as schematically illustrated in the left panels of Fig. 24, depending upon the polarity of illuminated surface, specific charge carrier (hole or electron) can be selected for transport in the direction perpendicular to the sample surface (in the direction of c-axis). Negatively (positively) biased illuminated surface immediately extracts holes (electrons) upon photo-generation and therefore, allowing only electrons (holes) to transport to the opposite electrode to be collected later. This property enables us to characterize the electrical transport properties for holes and electrons separately along the vertical (c-axis) direction. For instance, when a 50 μm thick h-^{10}BN detector is biased in the configuration shown in the left panels of Fig. 24(a), holes are swiped away at the negatively biased irradiated top surface and only electrons travel inside the material, and therefore this configuration allows us to probe transport properties of electrons. The photocurrents were measured for different configurations under UV excitation [37]. Fitting the measured I–V characteristics under UV excitation with Eq. (5), such as those shown in the right panels of Fig. 24, allows us to obtain the $\mu\tau$-products for different biasing configurations. Fig. 24 shows such measurements for two representative configurations. It is noted that for the same device the $\mu\tau$ product of electrons measured in the configuration of Fig. 24(a) in which the top surface was illuminated is more than 3 times larger than that measured in the configuration of Fig. 24(b) in which the bottom surface was illuminated. This is due to the high growth temperature of h-^{10}BN epilayer together with the use of sapphire substrate, which introduced a higher concentration of oxygen impurities near the bottom surface (the surface in contact with sapphire prior to release) compared to the top surface. This

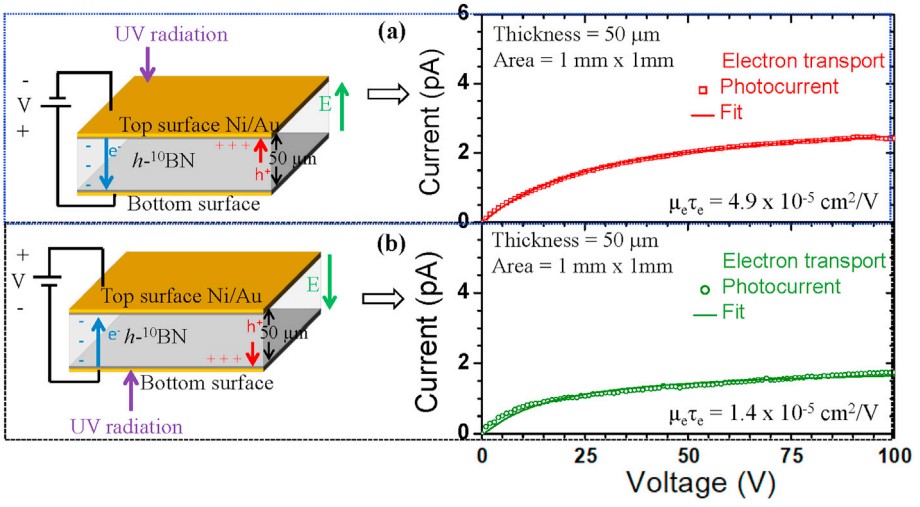

Fig. 24. Photocurrent-voltage characteristics of a photoconductive-like vertical detector fabricated from a 50 μm thick h-^{10}BN epilayer measured under UV irradiation for electron transport for two different biasing configurations [Ref. 37; Credit: A. Maity, S. J. Grenadier, J. Li, J. Y. Lin, and H. X. Jiang, J. Appl. Phys. **123**, 044501 (2018)].

interpretation was confirmed by SIMS measurements, which revealed that the oxygen impurity concentration is about 3 times higher near the bottom surface than that near the top surface [37]. On the other hand, the density of radiation generated charge carriers is highest near the irradiated surface and exponentially decreases with the distance from the irradiated surface. As such, the scattering of charge carriers by oxygen impurities can be minimized by chosen the top surface for irradiation than the bottom surface. Therefore, the measured μτ product is larger in the configuration of Fig. 24(a) than that in the configuration of Fig. 24(b). It was also shown that the optimal configuration of Fig. 24(a) has pushed the detection efficiency of h-^{10}BN neutron detectors to 58% at a bias voltage of 200 V, whereas other configurations provided a detection efficiency around 53% [37].

4.2. *Lateral detectors and transport properties*

It was shown recently that compared to vertical detectors consisting of planar contacts on top and bottom schematically shown in Fig. 24 [35–37], a lateral detector configuration schematically shown in Fig. 25(a) possesses several advantageous features [38–40]. To fabricate lateral detector, a freestanding h-^{10}BN wafer was diced into narrow strips. A highly resistive adhesive material was used to mount the strip detector on a sub-mount (sapphire). E-beam evaporation was used to deposit metal bi-layer of Ni (100 nm) and Au (40 nm) on the clipped edges of the h-^{10}BN strip detector using shadow mask leaving around ~100 μm metal covering on the edges, as schematically depicted in Fig. 25(a).

Compared to a vertical detector of the same detection area, a lateral detector possesses several advantageous features. Fig. 25 compares the dark I–V characteristics of a lateral h-^{10}BN detector to a vertical h-^{10}BN detector with comparable detection areas (29 mm^2 vs. 25 mm^2) fabricated from a 90 μm thick h-^{10}BN epilayer. The results revealed that the measured dark current (I_d) for the 29 mm^2 lateral detector shown in Fig. 25(a) was <0.1 pA at a bias voltage V_b > 500 V, which is considerably lower than that in the 25 mm^2 vertical h-^{10}BN detector shown in Fig. 25(b). This is because, other than a smaller cross-section area, the separation distance between the electrodes is farther apart in the lateral detector (detector width) compared to that in the vertical detector (detector thickness), providing a larger dark resistance, R. Fig. 26 shows the photocurrent-voltage characteristics under UV illumination for the same vertical and lateral h-^{10}BN detectors for both hole and electron transport. Depending upon the polarity of the illuminated surface holes or electron were chosen to travel though the material, allowing us to obtain photocurrent for holes and electrons separately in a vertical detector, as illustrated in the insets of Fig. 26(a) and (b) [35,36]. To conduct similar measurements for a 90 μm thick lateral h-^{10}BN detector, a metal slit was used to selectively illuminate near only one metal contact, as illustrated in the insets of Fig. 26(c) and (d). If the electrode near the illuminated area is positively (negatively) biased, holes (electrons) travel a much longer distance compared to electrons (holes) before being collected by the other electrode. This scheme enables us to measure the photocurrent for holes or electrons separately in a lateral detector [38–40].

Photocurrent-voltage characteristics for holes and electrons were then fitted with the Many's equation in Eq. (5) to obtain charge carrier mobility-lifetime μτ-product and surface recombination field s/μ. The measured $\mu_h\tau_h = 4.0 \times 10^{-6}$ cm^2/V for the vertical detector is 100 times smaller than that of the lateral detector ($\mu_h\tau_h = 4.1 \times 10^{-4}$ cm^2/V), and $\mu_e\tau_e = 1.6 \times 10^{-5}$ cm^2/V is 50 times smaller than that of the lateral detector (8.0×10^{-4} cm^2/V). These results reiterate the fact that lateral geometry is superior in terms of charge carrier transport properties compared to the vertical geometry due to the conductivity anisotropy in layered semiconductors [160,161]. Moreover, the measured surface recombination field for majority carrier electron (s_e/μ_e) was 1.05×10^4 V/cm for the vertical detector, which is 6.6 times higher than that in the lateral detector ($s_e/\mu_e = 1.6 \times 10^3$ V/cm). However, $s_h/\mu_h = 0.9 \times 10^3$ V/cm was found to be lower in the vertical detector than in the lateral detector. Furthermore, while the cross-section area for neutron radiation along the c-axis of h-^{10}BN is the same for both lateral and vertical detectors, the cross-section area for charge carrier collection (or the contact area) in a lateral detector shown schematically in Fig. 25(a) as well as in the insets of Fig. 26(c) and (d) is significantly reduced, providing almost two orders of magnitude reduction in the capacitance, *C*. These combined advantages have enabled us to increase the detector size while maintaining a high detection efficiency of >50% in lateral detectors [38,40].

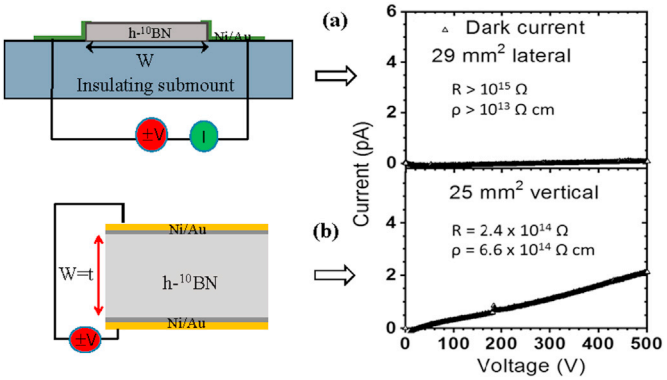

Fig. 25. (a) Schematic and dark I–V characteristic of a 29 mm^2 lateral h-^{10}BN detector of 90 μm in thickness. (b) Schematic and dark I–V characteristic of a vertical 25 mm^2 h-^{10}BN detector of 90 μm in thickness.

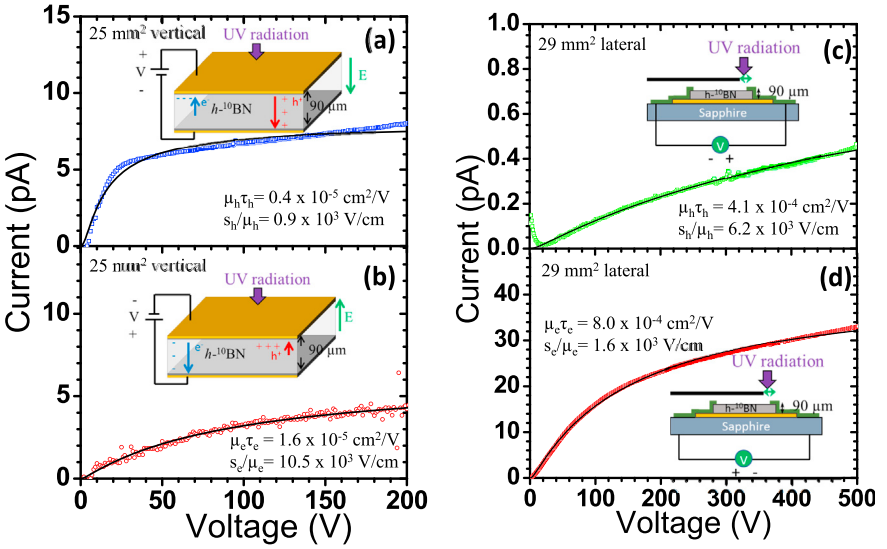

Fig. 26. (a) and (b) Photocurrent-voltage characteristics of a 90 μm thick vertical h-^{10}BN detector under UV excitation for (a) hole transport and (b) electron transport. The insets show schematic diagrams of the vertical detector with the illumination surface biased either positive or negative, allowing the measurement of electron and hole transport separately. The solid curves are the least squares fitting of data with Eq. (5). (c) and (d) Photocurrent-voltage characteristics of a 90 μm thick lateral h-^{10}BN detector under UV excitation for (c) hole transport and (d) electron transport. The insets show schematic diagrams of a lateral detector mounted on a sapphire submount with UV light illuminated through a metal mask near one electrode, allowing the measurement of electron and hole transport separately. The solid curves are the least squares fitting of data with Eq. (5) [Ref. 38; Credit: A. Maity, S. J. Grenadier, J. Li, J. Y. Lin, and H. X. Jiang, Appl. Phys. Lett. **114**, 222102 (2019)].

4.3. *Conditions for high detection sensitivity*

Other than high detection efficiency (η), it is also critical to fabricate neutron detectors with reasonable detection areas (A) to provide adequate sensitivities (ηA). This is due to the nature of low neutron flux from a primitive nuclear device (~3×10^5 neutrons/s) in application area of special nuclear materials detection and low reflectance of neutrons in porosity measurements in scenarios of well and geothermal logging. The sensitivity of a detector or count rate (C_R) detected by a detector is proportional to its detection efficiency (η) and detection area (A), i.e.,

$$C_R = \phi\, \eta A, \tag{5}$$

where ϕ is the neutron flux at the position of neutron detectors. However, the dark current (or the leakage current), the capacitance, the number of dislocations/defects/charge carrier traps and the surface recombination field all increase with an increase in the detector area. This creates technical challenges to retain high detection efficiencies in large area detectors. To ensure a high detection sensitivity, the electronic noise should be kept low. The equivalent noise charge in a simple CR-RC shaper at a fixed integration and differentiation time constant τ_c can be written as [162], $Q_n^2 = 0.924\left[2eI_d\tau_c + \frac{4K_BT}{R_b}\tau_c + e_n^2\frac{C^2}{\tau_c}\right]$, where the "shot noise" in the first term increases with the detector's dark current I_d, which is proportional to the device area (A), the second term is the "thermal noise" contributed from the bias resistor (R_b), and the last term depends on the equivalent input noise of the amplifier with a spectral density e_n and equivalent input capacitance C. Overall, the electronic noise increases linearly with I_d and quadratically with C [162]. The presence of a high noise level could increase the low-level discriminator threshold setting on the detection electronics for pulse height analysis, leading to exclusion of a fraction of the actual neutron counts from being detected and thereby decreasing the detection efficiency. Therefore, the presence of a high background noise (or dark count) could limit the ability of scaling up the device size while maintaining a high detection efficiency.

It was shown recently that lateral detectors can alleviate to some extent the technical challenges involved in scaling up the detector size and appear to be the geometry of choice for realizing h-^{10}BN detectors with high detection sensitivities [38–40]. One of the fundamental requirements for detecting a signal is that the size of the signal must be greater than the background noise or signal-to-noise ratio (SNR) is much larger than 1. The number of thermal neutrons generated charge carriers (N) via the nuclear reaction of Eqs. (3) and (4) can be estimated from the Klein's relation of $N \approx E/3E_g$ Ref. [163]. Here, E is the total energy deposited by the daughter particles and E_g (≈6.4 eV) is the energy bandgap of h-BN. Hence, the number of charge carriers generated per reaction, $N = 2.31 \times 10^6$ eV/(3×6.4 eV) $= 1.2 \times 10^5$ for the reaction with a 94% probability and $N = 2.79 \times 10^6$ eV/(3×6.4 eV) $= 1.4 \times 10^5$ for the reaction with a 6% probability, as described in Eqs. (3) and (4). Assuming a detection area of 1 cm^2, detector thickness of 100 μm, and volume V = 0.01 cm^3, the thermal neutron generated charge carrier density, n_n, which represents the size of the signal, can be estimated to be $n_n = N/V \approx$ (1.2–1.4) x 10^7 cm^{-3}. To detect this thermal neutron generated signal, ideally the background free carrier concentration, n_o, should be one order of magnitude smaller than the neutron generated electrical signal, n_n, and that means,

$$n_o < 10^6\ cm^{-3}. \quad (7)$$

Using the measured electron and hole mobility in the lateral direction in typical thick h-^{10}BN epilayers available today of 35 cm^2/V·s [39], the minimum dark electrical resistivity (ρ_0) of h-^{10}BN detector material to ensure neutron detectors with a high sensitivity can be determined from $\rho > \rho_0 = \frac{1}{en_0\mu}$, which yields

$$\rho > \rho_0 = 2 \times 10^{11}\ \Omega\ cm. \quad (8)$$

As the bandgap of h-BN is more than 6 eV, in principle, the background carrier concentration (n_o) in unintentionally doped h-BN is negligibly small and the intrinsic h-BN epilayers are expected to possess an electrical resistivity exceeding 10^{20} Ω cm. However, the highest resistivity of unintentionally doped h-BN epilayers produced so far is about 5×10^{14} Ω cm [35–40]. In practice, as illustrated in Fig. 21, unintentionally doped h-BN epilayers contain various defects which can contribute to the background carrier concentration as well as act as charge traps [74–81,88]. Therefore, further optimization of epitaxial growth processes is still needed to eliminate undesired defects and impurities, which in turn will further reduce the background carrier concentration and dark (or leakage) current and thereby increase the sensitivities of h-^{10}BN detectors.

4.4. Realization of high efficiency neutron detectors with 1 cm^2 detection area

As demonstrated through the dark current, μτ product and surface recombination field (s/μ) measurement results shown in Figs. 25 and 26, the lateral device architecture which utilizes the lateral transport properties is preferred over that of the vertical detector. Compared to the vertical detectors schematically shown in Fig. 25(b), the advantageous features of lateral detectors shown in Fig. 25(a) include: (1) Higher lateral carrier mobilities and hence larger μτ products; (2) The effects of surface recombination, which have been identified as one of the major factors that limits the charge collection efficiency in h-BN vertical detectors [159], are minimized in lateral detectors because the contact area between the electrodes and the detector's surface is minimized; (3) Inspecting the device geometries between the vertical and lateral detectors shown in Fig. 25, for the same detection area and detector thickness, the device capacitance for the lateral detector is reduced by more than 2 orders of magnitude compared to that of the vertical detector. The combined advantages of lateral device geometry have allowed the successful demonstration of neutron detectors with a detection area of 1 cm^2 with an unprecedently high detection efficiency at 59% [40].

A 100 μm thick freestanding h-^{10}BN wafer was diced into narrow strips. Five strips were combined with an average strip width of W = 1.2 mm and lengths varying from 13.5 to 17 mm to form a detector with a total detection area of 1 cm^2. A highly resistive adhesive material was used to mount these strips on a sub-mount (sapphire). E-beam evaporation was used to deposit metal bi-layer of Ni (100 nm) and Au (40 nm) on the clipped edges of the h-^{10}BN strips using shadow mask of 1.1 mm in width leaving ~100 μm metal covering on the edges, as schematically depicted in Fig. 27(a). The finished 1 cm^2 h-^{10}BN detector is shown in Fig. 27(b).

Dark current-voltage (I–V) measurements were performed for the 1 cm^2 detector from 0 to 500 V and the result is shown in Fig. 27(c). A linear fit of the I–V characteristic provides values of resistance, $R = 1.77 \times 10^{12}$ Ω, resistivity, $\rho = 1.05 \times 10^{12}$ Ω cm, and background electron concentration of $n_o \sim 6.2 \times 10^4$ cm^{-3} based on $\mu = 35$ cm^2/V·s measured in the lateral direction [39]. These basic material parameters all exceeded the minimum requirements for neutron detector fabrication described in Eqs. (7) and (8). I–V characteristics under UV illumination were also characterized. A metal mask was used to allow UV light to enter and illuminate the h-^{10}BN strips only near one electrode, as illustrated in the insets of Fig. 26(c) and (d). It was found that the photocurrent due to hole transport is extremely low in comparison to that of electron transport, which indicates that this h-^{10}BN epilayer has a higher concentration of donors than acceptors. The results again indicate that the background carrier concentration and hence the dark current are contributed by electrons from O_N donors due to the unavoidable oxygen diffusion from sapphire substrate into h-^{10}BN film during MOCVD growth [37, 39]. The measured I–V characteristic of electron transport under UV illumination is shown in Fig. 27(d). To determine the charge carrier μτ product and surface recombination field $E_s = s/\mu$, the measured photocurrent in Fig. 27(d) was fitted by Eq. (5). The measured values of $\mu_e\tau_e$ and s_e/μ_e for this detector were 5.0×10^{-3} cm^2/V and 5.5×10^2 V/cm, respectively, which provide values of $\frac{W}{\mu\tau E} \approx 0.007 \ll 1$ and $\frac{s_e/\mu_e}{V_b/W} \approx 0.14 \ll 1$at a bias voltage of 500 V, and a theoretical charge collection efficiency of 87.4% under UV irradiation. It is important to recognize that the measured $\mu_e\tau_e$ product of this detector has been enhanced by a factor of 6, while E_s^e has been reduced by a factor of 3 in comparison to those of a previous 29 mm^2 h-^{10}BN lateral detector shown in Fig. 26 [38]. These improvements were achieved primarily through MOCVD epitaxial growth optimization [40].

Pulse height spectra of this 1 cm^2 h-^{10}BN detector in response to thermal neutrons were measured at varying bias voltages [40]. The detector was placed at a distance of d = 1 m away from a^{252}Cf source with a radioactivity of 0.45 mCi (~1.95×10^6 n/s), moderated by a high-density polyethylene (HDPE) of 2.5 cm in thickness, as schematically shown in Fig. 28(a) [40]. In Fig. 28(b), the dark spectrum (blue) was recorded in the absence of any radiation source at 500 V, while spectrum (red) under thermal neutron irradiation was measured at the same bias voltage. The green curve is the detector's response to gamma photons emitted from a^{137}Cs source under 10 mR/h exposure measured at the same bias voltage, which shows that h-^{10}BN detector has a negligible response to gamma photons. The pulse height spectrum under thermal neutron radiation was integrated beyond the highest dark channel (low level discriminator or LLD) to obtain the total number of counts. Thermal neutron detection efficiency of the *h*-^{10}BN detector was calibrated against a commercially purchased ^{6}LiF filled micro-structured semiconductor neutron detector (MSND) from Radiation Detection Technologies, Inc. This MSND (Domino™ V4 model D411S-30-D0010-V4) has a built-in circuit which outputs 10 V TTL pulses. Furthermore, the circuit for the MSND also includes a built-in LLD which eliminates any background counts. The MSND detector was constructed by combining four 1 cm^2 detectors with a specified detection efficiency of 30 (±1) % for thermal neutrons. As illustrated in Fig. 27(a), by placing the MSND at the

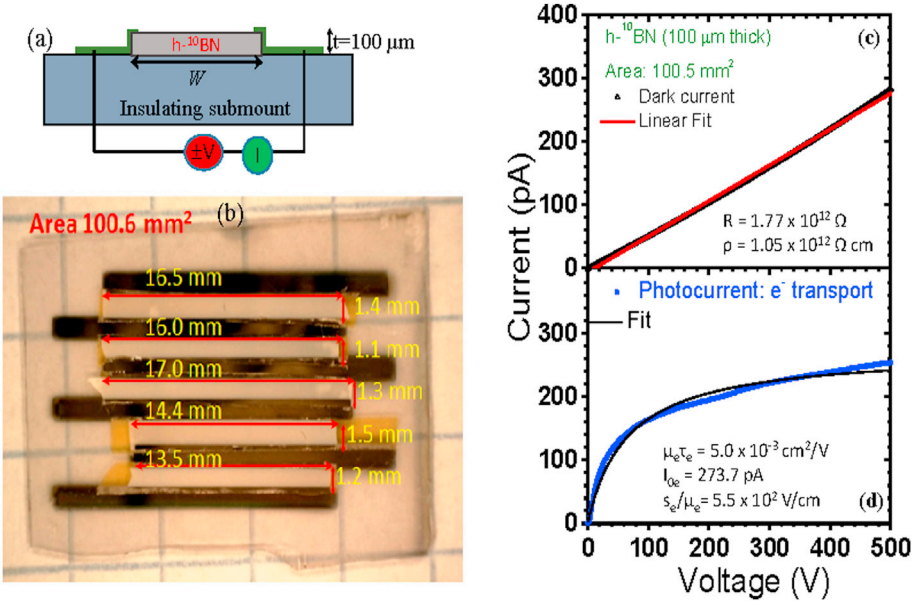

Fig. 27. (a) Schematic diagram of a lateral detector strip mounted on a sapphire submount. (b) Optical image of a 1 cm^2 neutron detector fabricated from 100 μm thick h-^{10}BN freestanding wafer by combining 5 detector strips. (c) Current-voltage characteristic in the dark and (d) current-voltage characteristic under UV irradiation for electron transport and the solid curve is the least squares fitting of data with Eq. (5) [Ref. 40; Credit: A. Maity, S. J. Grenadier, J. Li, J. Y. Lin, and H. X. Jiang, Appl. Phys. Lett. **116**, 142102 (2020)].

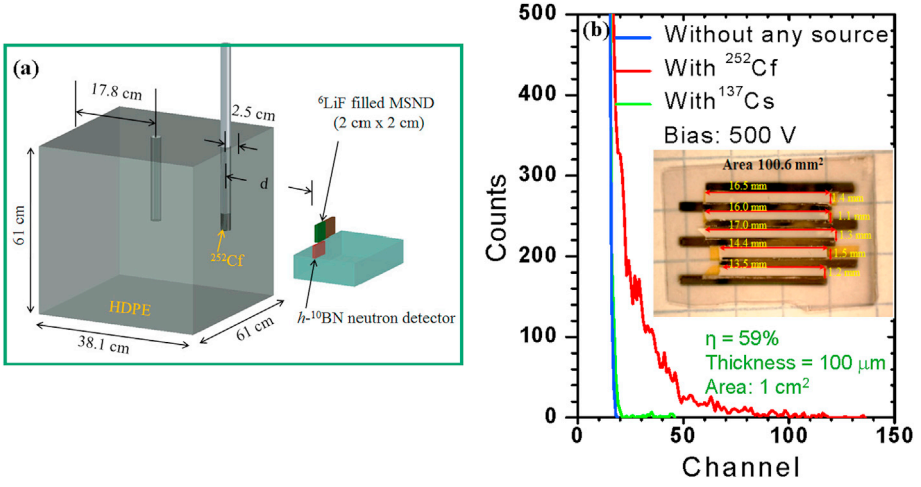

Fig. 28. (a) Schematic diagram of a thermal neutron source constructed from a^{252}Cf source moderated by a high-density polyethylene (HDPE) for characterizing the thermal neutron detection efficiencies of h-^{10}BN detectors [Ref. 35; Credit: A. Maity, T. C. Doan, J. Li, J. Y. Lin, and H. X. Jiang, Appl. Phys. Lett. **109**, 072101 (2016). (b) Pulse height spectra of the 1 cm^2 h-^{10}BN detector. Red curve is the response to thermal neutrons which was recorded by placing the detector at d = 1 m away from the ^{252}Cf source moderated by a HDPE cube. The blue curve is the background (or dark) counts measured at the same bias voltage. The green curve is the response to gamma photons emitted from a^{137}Cs source measured at the same bias voltage [Ref. 40; Credit: A. Maity, S. J. Grenadier, J. Li, J. Y. Lin, and H. X. Jiang, Appl. Phys. Lett. **116**, 142102 (2020)].

same position as the h-^{10}BN detector and knowing its detection efficiency (30%) and detection area (4 cm^2), the thermal neutron detection efficiency of the h-^{10}BN detector can be obtained by comparing the ratio of the count rates per unit area among both the h-^{10}BN and MSND detectors. By doing so, the detection efficiency (η) of our 1 cm^2 h-^{10}BN detector was determined to be 58.9 (±2.4) % at a bias voltage of 500 V, which represents the highest detection efficiency reported among all solid-state neutron detectors as of this writing. We believe that improvements in the overall h-^{10}BN material quality, as reflected through the enhanced μτ product and reduced surface recombination field and the utilization of a lateral device geometry stand to enable the scale up the detector size to 1 cm^2 while retaining a high detection efficiency of ~59%. The attainment of 1 cm^2 h-BN neutron detectors capable of retaining a high detection efficiency represents a significant milestone toward the practical applications of h-BN detectors [40].

It is noteworthy to point out that as the material quality of thick h-^{10}BN epilayers further improves, h-^{10}BN detectors are expected to resolve the nuclear reaction sum peaks at 2.31 MeV and 2.79 MeV of Eq. (3), as already demonstrated in low efficiency detectors fabricated from a very thin (2.7 μm) h-^{10}BN film [91]. Moreover, as shown in Figs. 15(b), 100 μm thick h-^{10}BN detectors are capable to provide an intrinsic detection efficiency of about 88%. The realized detection efficiency of ~59% for 1 cm^2 detector shown in Fig. 28 is still shy from the expected intrinsic detection efficiency. This is because the total detection efficiency of h-^{10}BN neutron detectors not only depends on the epilayer thickness, but also on the charge collection efficiency (η_c) as described by Eq. (5). As illustrated in Fig. 21(c), we have identified that oxygen impurities are one of the major bulk defects in thick h-^{10}BN films, which limit the μτ products and hence η_c. These oxygen impurities were diffused from sapphire substrates during high temperature (~1500 °C) growth and act as substitutional donors (O_N). Scattering of oxygen defects reduces the charge carrier μτ products and hence η_c.

To minimize the identified dominant defects in BN, further growth studies are needed. For instance, reducing the growth temperature is expected to mitigate to a certain degree the issue of oxygen impurities diffusion from sapphire substrate. However, higher growth temperature is preferred for obtaining BN films with enhanced crystalline quality. Therefore, the growth temperature window based on trade-offs between obtaining films with a high crystalline quality and low contents of oxygen impurities, as reflected through improved charge carrier μτ products, need to be further investigated. On the other hand, since AlN epilayers produced by MOCVD are of very high crystalline quality, the use of AlN epilayer as a template could be effective to block the diffusion of oxygen impurities from sapphire. As shown in Fig. 12, the feasibility of depositing high quality h-BN epilayers on top of AlN by MOCVD has already been demonstrated. It should be feasible to utilize AlN epilayer templates to obtain thick h-BN epilayers with reduced oxygen impurity concentrations. Similarly, it may be useful to develop hydride vapor phase epitaxy (HVPE) growth technique for h-BN, which is known to provide a much large growth rate than MOCVD with potential to significantly reduce the growth time for obtaining thick h-BN epilayers. However, there have only been very limited studies on HVPE growth of thin layers of BN in turbostratic phase [166].

With the outstanding features of a semiconductor detector (wafer thin material, reduced size and weight, no pressurization, increased ruggedness, lower power consumption, and large/faster signals), it is anticipated that ^{10}BN detectors can be used to design advanced ^{3}He replacement neutron detector systems with unprecedented performance for homeland security and well-logging applications [164,165]. In comparison to He-3 gas detectors, BN neutron detectors possess all the intrinsic advantages of semiconductor devices:

- BN materials are synthesized at very high temperatures (>1000 °C) and possess high thermal conductivity. The operating temperature of BN detectors is only limited by the metal contacts and wire connecting joints. By incorporating high temperature metal contact bonding schemes, BN detectors can withstand extremely high temperatures.
- BN neutron detectors are more flexible and durable and require lower voltages and no pressurization compared to He-3 detectors, thereby providing significant reduction in size and weight, more versatile forming factors, faster response speed, higher reliability, and lower costs for fabrication/operation/maintenance over those of the current state-of-the-art He-3 gas detectors.
- Due to the high thermal conductivity and high melting point of h-BN, BN detectors potentially enable logging tools to operate in harsh environments where He-3 detectors are not capable to operate.

5. Concluding remarks

By leveraging advances in III-nitride semiconductor growth technologies over the last three decades, significant progresses in epitaxial growth, understanding of the optical and electrical transport properties and device applications of h-BN have been achieved over the last 10 years. The growth of wafer scale *h*-BN epilayers on sapphire, AlN/sapphire template, and SiC substrates has been demonstrated. It was shown that the quasi-2D nature of h-BN gives rise to very high density of states near the band edge, unusually strong $p \rightarrow p$-like optical transitions and large exciton binding energy on the order of 0.7 eV. Evolution of the bandgap with temperature revealed that the bandgap of h-BN exhibits an unusual blueshift with temperature above 100 K, which can be attributed to the distinctive behavior of the in-plane thermal expansion coefficient of *h*-BN that becomes negative above 60 K. Evolution of the bandgap with layer thickness suggested that one can consider 100 layers (or 30 nm thick) h-BN as a "bulk" material. It was demonstrated that the band-edge emission in h-BN is predominantly transverse-electric (TE) polarized in contrast to the well-known transverse-magnetic (TM) polarization in AlN. Much lower p-type resistivity has been achieved in *h*-BN than in AlN. A p-type resistivity of ~2 Ω cm at 300 K via Mg doping has been measured, which is about 5 orders of magnitude lower than what has been possible for Mg doped AlN (>10^5 Ω cm) and has allowed the demonstration of h-BN/AlGaN p-n heterojunctions.

Due to the fact that the isotope of B-10 (^{10}B) has a large capture cross-section for thermal neutrons, *h*-BN is an ideal material for the fabrication of solid-state neutron detectors for applications in special nuclear materials detection, well and geothermal logging, and medical imaging and has the potential to address the issue of worldwide helium-3 gas shortage. However, due to the fact that the thermal neutron absorption length of 100% B-10 enriched h-BN (h-^{10}BN) is 47 μm, the prerequisite for achieving high efficiency neutron detectors is to realize h-^{10}BN epilayers with large thicknesses. It was found that when the thickness exceeds ~20 μm, after growth and during cooling down, a *h*-BN epilayer tends to automatically separates from the sapphire substrate due to its hexagonal (layered) structure and the difference in thermal expansion coefficients between *h*-BN and sapphire. Freestanding h-^{10}BN epilayers with thicknesses up to 200 μm have been realized as of this writing, which possess the potential to provide a 99% detection efficiency for thermal neutrons. By utilizing the conductivity anisotropy nature of h-BN, 1 cm^2 lateral neutron detectors fabricated from h-^{10}BN epilayers have attained a detection efficiency of 59% for thermal neutrons, which is the highest on record among all solid-state neutron detectors as of today. Moreover, freestanding *h*-BN epilayers are flexible with good conformability and transferability, and can be attached to rigid, flat, or curved surfaces and potentially offer a disruptive platform to design a wide range of novel photonic and electronic devices in flexible

form factors.

It was noted from optical and transport studies that various native and point defects, including nitrogen vacancies, carbon and oxygen impurities occupying the nitrogen sites, and boron vacancies significantly impact the optical and electrical properties of h-BN and h-BN device performance. In particular, during the growth of thick h-^{10}BN epilayers, high growth temperatures, long growth times and the use of a sapphire substrate tend to incorporate oxygen related donor impurities into h-^{10}BN epilayers as a result of oxygen diffusion from the sapphire substrate. It was shown that the oxygen related impurities strongly impacted the charge carrier mobility-lifetime ($\mu\tau$) products and charge carrier collection efficiencies of h-BN neutron detectors. These findings indicate that defect reduction strategies are needed to minimize the density of these identified defects or charge traps to further enhance the optical and optoelectronic properties as well as the electrical resistivity, carrier mobility and $\mu\tau$ products. As the h-BN material technology further develops, improved carrier mobilities and $\mu\tau$ products will allow the fabrication of neutron detectors with enhanced detection efficiencies and sensitivities.

Acknowledgement

The h-BN material and neutron detector research are supported by DOE ARPA-E (DE-AR0001257). The development of h-BN material and device technologies at TTU has been supported by DOE ARPA-E (DE-AR0000964), NNSA SSAP program (DE-NA0002927), and (DE-FG02-09ER46552); DHS ARI Program (No. 2011-DN077-ARI048); NSF (DMR-1206652) and (ECCS-1402886). H. X. Jiang and J. Y. Lin are grateful to the AT&T Foundation for the support of Ed Whitacre and Linda Whitacre endowed chairs.

References

[1] I. Akasaki, Fascinated journeys into blue light, nobel lecture, Ann. Phys. 527 (2015) 311. https://www.nobelprize.org/uploads/2018/06/akasaki-lecture.pdf.
[2] H. Amano, Growth of GaN on sapphire via low-temperature deposited buffer layer and realization of p-type GaN by Mg doping followed by low- energy electron beam irradiation, nobel lecture, Ann. Phys. 527 (2015) 327. https://www.nobelprize.org/uploads/2018/06/amano-lecture.pdf.
[3] S. Nakamura, Background story of the invention of efficient blue InGaN light emitting diodes, nobel lecture, Ann. Phys. 527 (2015) 335. https://www.nobelprize.org/uploads/2018/06/nakamura-lecture.pdf.
[4] S. Nakamura, S.J. Pearton, G. Fasol, G, The blue laser diode. The complete story, Meas. Sci. Technol. 12 (2001) 755.
[5] S. Nakamura, A bright future for blue/green LEDs, IEEE Circ. Dev. Mag. 11 (1995) 19.
[6] R.S. Pease, An X-ray study of boron nitride, Acta Crystallogr. 5 (1952) 536.
[7] R.W. Lynch, H.G. Drickamer, Effect of high pressure on the lattice parameters of diamond, graphite, and hexagonal boron nitride, J. Chem. Phys. 44 (1966) 181.
[8] Q. Madelung, Landolt-Bornstein (Eds.), Numerical/Data and Functional/Relationship in Science and Technology - Crystal and Solid-State Physics, vol. III, Springer, Berlin, 1972.
[9] A. Zunger, A. Katzir, A. Halperin, Optical properties of hexagonal boron nitride, Phys. Rev. B13 (1976) 5560.
[10] T. Sugino, K. Tanioka, S. Kawasaki, J. Shirafuji, Characterization and field emission of sulfur-doped boron nitride synthesized by plasma-assisted chemical vapor deposition, Jpn. J. Appl. Phys. 36 (1997) L463.
[11] K. Watanabe, T. Taniguchi, H. Kanda, Direct-bandgap properties and evidence for ultraviolet lasing of hexagonal boron nitride single crystal, Nat. Mater. 3 (2004) 404.
[12] Y. Kubota, K. Watanabe, O. Tsuda, T. Taniguchi, Deep ultraviolet light-emitting hexagonal boron nitride synthesized at atmospheric pressure, Science 317 (2007) 932.
[13] K. Watanabe, T. Taniguchi, T. Niyama, K. Miya, M. Taniguchi, Far-ultraviolet plane-emission handheld device based on hexagonal boron nitride, Nat. Photon. 3 (2009) 591.
[14] K. Watanabe, T. Taniguchi, Jahn-Teller effect on exciton states in hexagonal boron nitride single crystal, Phys. Rev. B79 (2009) 193104.
[15] B. Arnaud, S. Lebègue, P. Rabiller, M. Alouani, Huge excitonic effects in layered hexagonal boron nitride, Phys. Rev. Lett. 96 (2006), 026402 and "Arnaud, Lebègue, Rabiller, and Alouani Reply," Phys. Rev. Lett. 100, 189702 (2008).
[16] L. Wirtz, A. Marini, A. Rubio, Excitons in boron nitride nanotubes: dimensionality effects, Phys. Rev. Lett. 96 (2006) 126104.
[17] L. Wirtz, A. Marini, M. Gruning, C. Attaccalite, G. Kresse, A. Rubio, "Comment on "huge excitonic effects in layered hexagonal boron nitride", Phys. Rev. Lett. 100 (2008) 189701.
[18] X.K. Cao, B. Clubine, J.H. Edgar, J.Y. Lin, H.X. Jiang, Two-dimensional excitons in three-dimensional hexagonal boron nitride, Appl. Phys. Lett. 103 (2013) 191106.
[19] B. Huang, X.K. Cao, H.X. Jiang, J.Y. Lin, S.H. Wei, Origin of the significantly enhanced optical transitions in layered boron nitride, Phys. Rev. B 86 (2012) 155202.
[20] S. Majety, X.K. Cao, J. Li, R. Dahal, J.Y. Lin, H.X. Jiang, Band-edge transitions in hexagonal boron nitride epilayers, Appl. Phys. Lett. 101 (2012), 051110.
[21] T.C. Doan, J. Li, J.Y. Lin, H.X. Jiang, Bandgap and exciton binding energies of hexagonal boron nitride probed by photocurrent excitation spectroscopy, Appl. Phys. Lett. 109 (2016) 122101.
[22] A.K. Geim, K.S. Novoselov, The rise of Graphene, Nat. Mater. 6 (2007) 183.
[23] A.K. Geim, P. Kim, Carbon wonderland, Sci. Am. 298 (2008) 90.
[24] http://www.ioffe.ru/SVA/NSM/Semicond/.
[25] S.L. Rumyantsev, M.E. Levinshtein, A.D. Jackson, S.N. Mohammmad, G.L. Harris, M.G. Spencer, M.S. Shur, in: M.E. Levinshtein, S.L. Rumyantsev, M.S. Shur (Eds.), Properties of Advanced SemiconductorMaterials GaN, AlN, InN, BN, SiC, SiGe, John Wiley & Sons, Inc., New York, 2001, pp. 67–92.
[26] http://www.phy.mtu.edu/~jaszczak/graphprop.html.
[27] M.R. Uddin, T.C. Doan, J. Li, K.S. Ziemer, J.Y. Lin, H.X. Jiang, Electrical transport properties of (BN)-rich hexagonal (BN)C semiconductor alloys, AIP Adv. 4 (2014), 087141.
[28] R. Dahal, J. Li, S. Majety, B.N. Pantha, X.K. Cao, J.Y. Lin, H.X. Jiang, Epitaxially grown semiconducting hexagonal boron nitride as a deep ultraviolet photonic material, Appl. Phys. Lett. 98 (2011) 211110.
[29] S. Majety, J. Li, X.K. Cao, R. Dahal, B.N. Pantha, J.Y. Lin, H.X. Jiang, Epitaxial growth and demonstration of hexagonal BN/AlGaN p-n junctions for deep ultraviolet photonics, Appl. Phys. Lett. 100 (2012), 061121.
[30] H.X. Jiang, J.Y. Lin, Hexagonal boron nitride for deep ultraviolet photonic devices, Semicond. Sci. Technol. 29 (2014), 084003.
[31] H. X. Jiang, S. Majety, R. Dahal, J, Li, and J. Y. Lin, "Structures and Devices Based on Boron Nitride and Boron Nitride-III-Nitride Heterostructures" US patent #9,093,581.
[32] J. Li, S. Majety, R. Dahal, W.P. Zhao, J.Y. Lin, H.X. Jiang, Dielectric strength, optical absorption, and deep ultraviolet detectors of hexagonal boron nitride epilayers, Appl. Phys. Lett. 101 (2012) 171112.
[33] M.R. Uddin, S. Majety, J. Li, J.Y. Lin, H.X. Jiang, Layer-structured hexagonal (BN)C semiconductor alloys with tunable optical and electrical properties, J. Appl. Phys. 115 (2014), 093509.

[34] M.R. Uddin, J. Li, J.Y. Lin, H.X. Jiang, Carbon-rich hexagonal (BN)C alloys, J. Appl. Phys. 117 (2015) 215703.
[35] A. Maity, T.C. Doan, J. Li, J.Y. Lin, H.X. Jiang, Realization of highly efficient hexagonal boron nitride neutron detectors, Appl. Phys. Lett. 109 (2016), 072101.
[36] A. Maity, S.J. Grenadier, J. Li, J.Y. Lin, H.X. Jiang, Toward achieving flexible and high sensitivity hexagonal boron nitride neutron detectors, Appl. Phys. Lett. 111 (2017), 033507.
[37] A. Maity, S.J. Grenadier, J. Li, J.Y. Lin, H.X. Jiang, Hexagonal boron nitride neutron detectors with high detection efficiencies, J. Appl. Phys. 123 (2018), 044501.
[38] A. Maity, S.J. Grenadier, J. Li, J.Y. Lin, H.X. Jiang, High sensitivity hexagonal boron nitride lateral neutron detectors, Appl. Phys. Lett. 114 (2019) 222102.
[39] S.J. Grenadier, A. Maity, J. Li, J.Y. Lin, H.X. Jiang, Lateral charge carrier transport properties of B-10 enriched hexagonal BN thick epilayers, Appl. Phys. Lett. 115 (2019), 072108.
[40] A. Maity, S.J. Grenadier, J. Li, J.Y. Lin, H.X. Jiang, High efficiency hexagonal boron nitride neutron detectors with 1 cm^2 detection areas, Appl. Phys. Lett. 116 (2020) 142102.
[41] N. Alem, R. Erni, C. Kisielowski, M.D. Rossell, W. Gannett, A. Zettl, Atomically thin hexagonal boron nitride probed by ultrahigh-resolution transmission electron microscopy, Phys. Rev. B 80 (2009) 155425.
[42] C.R. Dean, A.F. Young, I. Meric, C. Lee, L. Wang, S. Sorgenfrei, K. Watanabe, T. Taniguchi, P. Kim, K.L. Shepard, J. Hone, Boron nitride substrates for high-quality graphene electronics, Nat. Nanotechnol. 5 (2010) 722.
[43] L. Britnell, R.V. Gorbachev, R. Jalil, B.D. Belle, F. Schedin, A. Mishchenko, T. Georgiou1, M.I. Katsnelson, L. Eaves, S.V. Morozov, N.M.R. Peres, J. Leist, A.K. Geim, K.S. Novoselov, L.A. Ponomarenko, Field-effect tunneling transistor based on vertical graphene heterostructures, Science 335 (2012) 947.
[44] C. Dean, A.F. Young, L. Wang, I. Meric, G.H. Lee, K. Watanabe, T. Taniguchi, K. Shepard, P. Kim, J. Hone, Graphene based heterostructures, Solid State Commun. 152 (2012) 1275.
[45] L. Song, L. Ci, H. Lu, P.B. Sorokin, C. Jin, J. Ni, A.G. Kvashnin, D.G. Kvashnin, J. Lou, B.I. Yakobson, P.M. Ajayan, Large scale growth and characterization of atomic hexagonal boron nitride layers, Nano Lett. 10 (2010) 3209.
[46] A.K. Geim, I.V. Grigorieva, Van der Waals heterostructures, Nature 499 (2013) 419.
[47] T. Makimoto, K. Kumakura, Y. Kobayashi, T. Akasaka, H. Yamamoto, A vertical InGaN/GaN light-emitting diode fabricated on a flexible substrate by a mechanical transfer method using BN, APEX 5 (2012), 072102.
[48] Y. Kobayashi, K. Kumakura, T. Akasaka, T. Makimoto, Layered boron nitride as a release layer for mechanical transfer of GaN-based devices, Nature 484 (2012) 223.
[49] J. Robertson, Electronic structure and core exciton of hexagonal boron nitride, Phys. Rev. B**29** (1984) 2131.
[50] A. Catellani, M. Posternak, A. Baldereschi, A.J. Freeman, Bulk and surface electronic structure of hexagonal boron nitride, Phys. Rev. B36 (1987) 6105.
[51] R.M. Wentzcovitch, S. Fahy, Marvin L. Cohen, Steven G. Louie, Ab initio study of graphite and diamondlike transitions in BN, Phys. Rev. B38 (1988) 6191.
[52] Y.N. Xu, W.Y. Ching, Calculation of ground-state and optical properties of boron nitrides in the hexagonal, cubic, and wurtzite structures, Phys. Rev. B44 (1991) 7787.
[53] X. Blase, A. Rubio, Steven G. Louie, Marvin L. Cohen, Quasiparticle Band Structure of Bulk Hexagonal Boron Nitride and Related Systems, B51, 1995, p. 6868.
[54] G. Cassabois, P. Valvin, B. Gil, Hexagonal boron nitride is an indirect bandgap semiconductor, Nat. Photon. 10 (2016) 262.
[55] L. Liu, Y.P. Feng, Z.X. Shen, Structure and electronic properties of h-BN, Phys. Rev. B68 (2003) 104102.
[56] K. Nakamura, Preparation and properties of boron nitride films by metal organic chemical vapor deposition, J. Electrochem. Soc. 133 (1986) 1120.
[57] Y. Kobayashi, T. Makimoto, "Growth of boron nitride on 6H–SiC substrate by flow-rate modulation epitaxy, Jpn. J. Appl. Phys. 45 (2006) 3519.
[58] Y. Kobayashi, T. Akasaka, Hexagonal BN epitaxial growth on (0 0 0 1) sapphire substrate by MOVPE, J. Cryst. Growth 310 (2008) 5044.
[59] Y. Kobayashi, T. Akasaka, T. Makimoto, Hexagonal boron nitride grown by MOVPE, J. Cryst. Growth 310 (2008) 5048.
[60] M. Chubarov, H. Pedersen, H. Högberg, S. Filippov, J.A.A. Engelbrecht, J. O'Connel, A. Henry, Boron nitride: a new photonic material, Physica B 439 (2014) 29.
[61] X. Li, S. Sundaram, Y. El Gmili, T. Ayari, R. Puybaret, G. Patriarche, P.L. Voss, J.P. Salvestrini, A. Ougazzaden, Large-area two-dimensional layered hexagonal boron nitride grown on sapphire by metalorganic vapor phase epitaxy, Cryst. Growth Des. 16 (2016) 3409.
[62] D. Chugh, J. Wong-Leung, L. Li, M. Lysevych, H.H. Tan, C. Jagadish, Flow Modulation Epitaxy of Hexagonal Boron Nitride, vol. 5, 2018, 045018.
[63] X. Yang, S. Nitta, K. Nagamatsu, S.Y. Bae, H.J. Lee, Y.H. Liu, M. Pristovsek, Y. Honda, H. Amano, Growth of hexagonal boron nitride on sapphire substrate by pulsed-mode metalorganic vapor phase epitaxy, J. Cryst. Growth 482 (2018) 1.
[64] X. Yang, S. Nitta, M. Pristovsek, Y. Liu, Y. Liao, M. Kushimoto, Y. Honda, H. Amano, Scalable synthesis of multilayer h-BN on AlN by metalorganic vapor phase epitaxy: nucleation and growth mechanism, 2D Mater. 7 (2020), 015004.
[65] A. Rice, A. Allerman, M. Crawford, T. Beechem, T. Ohta, C. Spataru, J. Figiel, M. Smith, Effects of deposition temperature and ammonia flow on metal-organic chemical vapor deposition of hexagonal boron nitride, J. Cryst. Growth 485 (2018) 90.
[66] B.N. Pantha, R. Dahal, M.L. Nakarmi, N. Nepal, J. Li, J.Y. Lin, H.X. Jiang, Q.S. Paduano, David Weyburne, Correlation between optoelectronic and structural properties and epilayer thickness of AlN, Appl. Phys. Lett. 90 (2007) 241101.
[67] M.A. Khan, J.N. Kuznia, R.A. Skogman, D.T. Olson, M.M. Millan, W.J. Choyke, Low pressure metalorganic chemical vapor deposition of AlN over sapphire substrates, Appl. Phys. Lett. 61 (1992) 2539.
[68] M. Imura, H. Sugimura, N. Okada, M. Iwaya, S. Kamiyama, H. Amano, I. Akasaki, A. Bandoh, Impact of high-temperature growth by metal-organic vapor phase epitaxy on microstructure of AlN on 6*H*-SiC substrates, J. Cryst. Growth 310 (2008) 2308.
[69] H.J. Kim, S. Choi, D. Yoo, J.H. Ryou, R.D. Dupuis, R.F. Dalmau, P. Lu, Z. Sitar, Modulated precursor flow epitaxial growth of AlN layers on native AlN substrates by metal-organic chemical vapor deposition, Appl. Phys. Lett. 93 (2008), 022103.
[70] M.G. Silly, P. Jaffrennou, J. Barjon, J.-S. Lauret, F. Ducastelle, A. Loiseau, E. Obraztsova, B. Attal-Tretout, E. Rosencher, Luminescence properties of hexagonal boron nitride: cathodoluminescence and photoluminescence spectroscopy measurements, Phys. Rev. B 75 (2007), 085205.
[71] W. Orellana, H. Chacham, Stability of native defects in hexagonal and cubic boron nitride, Phys. Rev. B 63 (2001) 125205.
[72] M. Fanciulli, T.D. Moustakas, Study of defects in wide band gap semiconductors by electron paramagnetic resonance, Physica B 185 (1993) 228.
[73] I. Jimenez, A.F. Jankowski, L.J. Terminello, D.G.J. Sutherland, J.A. Carlisle, G.L. Doll, W.M. Tong, D.K. Shuh, F.J. Himpsel, Core-level photo-absorption study of defects and metastable bonding configurations in boron nitride, Phys. Rev. B 55 (1997) 12025.
[74] T.B. Ngwenya, A.M. UKpong, N. Chetty, Defect states of complexes involving a vacancy on the boron site in boronitrene, Phys. Rev. B 84 (2011) 245425.
[75] B. Huang, H. Lee, Defect and impurity properties of hexagonal boron nitride: a first-principles calculation, Phys. Rev. B 86 (2012) 245406.
[76] C. Attaccalite, M. Bockstedte, A. Marini, A. Rubio, L. Wirtz, Coupling of excitons and defect states in boron-nitride nanostructures, Phys. Rev. B 83 (2011) 144115.
[77] A. Zunger, A. Katzir, Point defects in hexagonal boron nitride. II. Theoretical studies, Phys. Rev. 11 (1975) 2378.
[78] V. Wang, N. Ma, H. Mizuseki, Y. Kawazoe, First-principles study of intrinsic defect properties in hexagonal BN bilayer and monolayer, Solid State Commun. 152 (2012) 816.
[79] L. Weston, D. Wickramaratne, M. Mackoit, A. Alkauskas, C.G. Van de Walle, Native point defects and impurities in hexagonal boron nitride, Phys. Rev. B**97** (2018) 214104.
[80] X.Z. Du, J. Li, J.Y. Lin, H.X. Jiang, The origin of deep-level impurity transitions in hexagonal boron nitride, Appl. Phys. Lett. 106 (2015), 021110.
[81] X.Z. Du, J. Li, J.Y. Lin, H.X. Jiang, The origins of near band-edge transitions in hexagonal boron nitride epilayers, Appl. Phys. Lett. 108 (2016), 052106.
[82] H.X. Jiang, J.Y. Lin, Review - hexagonal boron nitride epilayers: growth, optical properties and device applications, ECS J. Solid State Sci. Technol. 6 (2017) Q3012.
[83] L. Museur, A. Kanaev, Near band-gap photoluminescence properties of hexagonal boron nitride, J. Appl. Phys. 103 (2008) 103520.
[84] L. Museur, E. Feldbach, A. Kanaev, Defect-related photoluminescence of hexagonal boron nitride, Phys. Rev. B 78 (2008) 155204.
[85] J. Wu, Wei-Qiang Han, W. Walukiewicz, J.W. Ager III, W. Shan, E.E. Haller, A. Zettl, Raman spectroscopy and time-resolved photoluminescence of BN and B*xCyNz* nanotubes, Nano Lett. 4 (2004) 647.

[86] L. Museur, G. Brasse, A. Pierret, S. Maine, B. Attal-Tretout, F. Ducastelle, A. Loiseau, J. Barjon, K. Watanabe, T. Taniguchi, A. Kanaev, Exciton optical transitions in a hexagonal boron nitride single crystal, Phys. Status Solidi 5 (2011) 214.
[87] P. Jaffrennou, J. Barjon, J.S. Lauret, B. Attal-Tretout, F. Ducastelle, A. Loiseau, Origin of the excitonic recombination in hexagonal boron nitride by spatially resolved cathodoluminescence spectroscopy, J. Appl. Phys. 102 (2007) 116102.
[88] S.J. Grenadier, A. Maity, J. Li, J.Y. Lin, H.X. Jiang, Origin and roles of oxygen impurities in hexagonal boron nitride epilayers, Appl. Phys. Lett. 112 (2018) 162103.
[89] A.S. Vokhmintsev, I.A. Weinstein, M.G. Minin, S.A. Shalyakin, Thermally stimulated processes in the luminescence of carbon-related defects for h-BN micro-powder, Radiat. Meas. 124 (2019) 35.
[90] A.S. Vokhmintsev, I.A. Weinstein, Temperature Effects in Luminescence of Associated Oxygen-Carbon Pairs in Hexagonal Boron Nitride under Direct Optical Excitation within 7-1100 K Range, arXiv, 2003, 02789.
[91] T.C. Doan, J. Li, J.Y. Lin, H.X. Jiang, Charge carrier transport properties in layer structured hexagonal boron nitride, AIP Adv. 4 (2014) 107126.
[92] V.M. Kaganer, O. Brandt, A. Trampert, K.H. Ploog, X-ray diffraction peak profiles from threading dislocations in GaN epitaxial films, Phys. Rev. B 72 (2005), 045423.
[93] S.R. Lee, A.M. West, A.A. Allerman, K.E. Waldrip, D.M. Follstaedt, P.P. Provencio, D.D. Koleske, C.R. Abernathy, Effect of threading dislocation on the Bragg peak linewidths of GaN, AlGaN, and AlN heterolayers, Appl. Phys. Lett. 86 (2005) 241904.
[94] R.J. Nemanich, S.A. Solin, R.M. Martin, Light scattering study of boron nitride microcrystals, Phys. Rev. B 23 (1981) 6348.
[95] X.Z. Du, M.R. Uddin, J. Li, J.Y. Lin, H.X. Jiang, Layer number dependent optical properties of multilayer hexagonal BN epilayers, Appl. Phys. Lett. 110 (2017), 092102.
[96] M.L. Nakarmi, K.H. Kim, M. Khizar, Z.Y. Fan, J.Y. Lin, H.X. Jiang, Electrical and optical properties of Mg-doped $Al_{0.7}Ga_{0.3}N$ alloys, Appl. Phys. Lett. 86 (2005), 092108.
[97] K.B. Nam, M.L. Nakarmi, J. Li, J.Y. Lin, H.X. Jiang, Mg acceptor level in AlN probed by deep ultraviolet photoluminescence, Appl. Phys. Lett. 83 (2003) 878.
[98] M.L. Nakarmi, N. Nepal, C. Ugolini, T.M. Al Tahtamouni, J.Y. Lin, H.X. Jiang, Correlation between optical and electrical properties of Mg-doped AlN epilayers, Appl. Phys. Lett. 89 (2006) 152120.
[99] Y. Taniyasu, M. Kasu, T. Makimoto, "An aluminum nitride light-emitting diode with a wavelength of 210 nanometres, Nature 441 (2006) 325.
[100] M.L. Nakarmi, N. Nepal, J.Y. Lin, H.X. Jiang, Photoluminescence studies of impurity transitions in Mg-doped AlGaN alloys, Appl. Phys. Lett. 94 (2009), 091903.
[101] J. Li, T.N. Oder, M.L. Nakarmi, J.Y. Lin, H.X. Jiang, Optical and electrical properties of Mg-doped p-type AlGaN, Appl. Phys. Lett. 80 (2002) 1210.
[102] J. Simon, V. Protasenko, C. Lian, H. Xing, D. Jena, Polarization-induced hole doping in wide-band-gap uniaxial semiconductor heterostructures, Science 327 (2010) 60.
[103] Z. Zhang, M. Kushimoto, T. Sakai, N. Sugiyama, L.J. Schowalter, C. Sasaoka, H. Amano, A 271.8 nm deep-ultraviolet laser diode for room temperature operation, APEX 12 (2019) 124003.
[104] J. Piprek, Z.M. Simon Li, Sensitivity analysis of electron leakage in III-nitride light-emitting diodes, Appl. Phys. Lett. 102 (2013) 131103.
[105] Y. Li, S. Chen, W. Tian, Z. Wu, Y. Fang, J. Dai, C. Chen, Advantages of AlGaN-based 310-nm UV light-emitting diodes with Al content graded AlGaN electron blocking layers, IEEE Photonics J. 5 (2013) 8200309.
[106] H. Hirayama, Y. Tsukada, T. Maeda, N. Kamata, Marked enhancement in the efficiency of deep-ultraviolet AlGaN light-emitting diodes by using a multiquantum-barrier electron blocking layer, APEX 3 (2010), 031002.
[107] D.A. Laleyan, S. Zhao, S.Y. Woo, H.N. Tran, H.B. Le, T. Szkopek, H. Guo, G.A. Botton, Z. Mi, AlN/h-BN heterostructures for Mg dopant-free deep ultraviolet photonics, Nano Lett. 17 (2017) 3738.
[108] H. Henck, D. Pierucci, G. Fugallo, J. Avila, G. Cassabois, Y.J. Dappe, M.G. Silly, C. Chen, B. Gil, M. Gatti, F. Sottile, F. Sirotti, M.C. Asensio, A. Ouerghi, Direct observation of the band structure in bulk hexagonal boron nitride, Phys. Rev. B 95 (2017), 085410.
[109] S. Majety, J. Li, W.P. Zhao, B. Huang, S.H. Wei, J.Y. Lin, H.X. Jiang, Hexagonal boron nitride and 6H-SiC heterostructures, Appl. Phys. Lett. 102 (2013) 213505.
[110] R. Dahal, T.M. Al Tahtamouni, Z.Y. Fan, J.Y. Lin, H.X. Jiang, "Hybrid AlN–SiC deep ultraviolet Schottky barrier photodetectors, Appl. Phys. Lett. 90 (2007) 263505.
[111] R. Dahal, T.M. Al Tahtamouni, J.Y. Lin, H.X. Jiang, AlN avalanche photodetectors, Appl. Phys. Lett. 91 (2007) 243503.
[112] S.L. Feng, J. Krynicki, V. Donchev, J.C. Bourgoin, M. Di Forte-Poisson, C. Brylinski, S. Delage, H. Blanck, S. Alaya, Band offset of GaAs-GaInP heterojunctions, Semicond. Sci. Technol. 8 (1993) 2092.
[113] Z. Sitar, M.J. Paisley, D.K. Smith, R.E. Davis, Design and performance of an electron cyclotron resonance plasma source for standard molecular beam epitaxy equipment, Rev. Sci. Instrum. 61 (1990) 2407.
[114] J. Choi, J.P. Chang, Photoconductivity of AlN films on SiC, J. Appl. Phys. 98 (2005), 093513.
[115] J. Uher, S. Pospisil, V. Linhart, M. Schiebar, Efficiency of composite boron nitride neutron detectors in comparison with helium-3 detectors, Appl. Phys. Lett. 90 (2007) 124101.
[116] F. P. Doty (Sandia National Laboratories), *Boron Nitride Solid-State Neutron Detec*tor, US patent, 6727504..
[117] J. Li, R. Dahal, S. Majety, J.Y. Lin, H.X. Jiang, Hexagonal boron nitride epitaxial layers as neutron detector materials, Nucl. Instrum. Methods Phys. Res., Sect. A 654 (2011) 417.
[118] T.C. Doan, S. Majety, S. Grendadier, J. Li, J.Y. Lin, H.X. Jiang, Fabrication and characterization of solid-state thermal neutron detectors based on hexagonal boron nitride epilayers, Nucl. Instrum. Methods Phys. Res., Sect. A 748 (2014) 84.
[119] T.C. Doan, S. Majety, S. Grenadier, J. Li, J.Y. Lin, H.X. Jiang, Hexagonal boron nitride thin film thermal neutron detectors with high energy resolution of the reaction products, Nucl. Instrum. Methods Phys. Res., Sect. A 783 (2015) 121.
[120] T.C. Doan, J. Li, J.Y. Lin, H.X. Jiang, Growth and device processing of hexagonal boron nitride epilayers for thermal neutron and deep ultraviolet detectors, AIP Adv. 6 (2016), 075213.
[121] K. Ahmed, R. Dahal, A. Weltz, James J.Q. Lu, Y. Danon, I.B. Bhat, Appl. Phys. Lett. 110 (2017), 023503.
[122] G.F. Knoll, Radiation Detection and Measurement, 3rd Ed (J. Wiley, 2000); N. Tsoulfanidis, Measurement and Detection of Radiation, Taylor & Francis, Washington, 1995, pp. 131–137.
[123] O. Osberghaus, Isotopic abundance of boron. Mass-spectrometric investigation of the electron-impact products of boron trifluoride and boron trichloride, Zeitschrift fuer Physik 128 (1950) 366.
[124] K.B. Nam, J. Li, M.L. Nakarmi, J.Y. Lin, H.X. Jiang, Unique optical properties of AlGaN alloys and related ultraviolet emitters, Appl. Phys. Lett. 84 (2004) 5264.
[125] G.D. Chen, M. Smith, J.Y. Lin, H.X. Jiang, S.-H. Wei, M.A. Khan, C.J. Sun, Fundamental optical transitions in GaN, Appl. Phys. Lett. 68 (1996) 2784.
[126] J. Li, K.B. Nam, M.L. Nakarmi, J.Y. Lin, H.X. Jiang, Pierre Carrier, and Su-Huai Wei, "Band structure and fundamental optical transitions in wurtzite AlN, Appl. Phys. Lett. 83 (2003) 5163.
[127] T.N. Oder, K.H. Kim, J.Y. Lin, H.X. Jiang, III-nitride blue and ultraviolet photonic crystal light emitting diodes, Appl. Phys. Lett. 84 (2004) 466.
[128] J. Shakya, K.H. Kim, J.Y. Lin, H.X. Jiang, Enhanced light extraction in III-nitride ultraviolet photonic crystal light-emitting diodes, Appl. Phys. Lett. 85 (2004) 142.
[129] H. Kawanishi, M. Senuma, T. Nukui, Anisotropic polarization characteristics of lasing and spontaneous surface and edge emissions from deep-ultraviolet ($\lambda \approx 240$nm) AlGaN multiple-quantum-well lasers, Appl. Phys. Lett. 89 (2006), 041126.
[130] P.B. Perry, R.F. Rutz, "The optical absorption edge of single-crystal AlN prepared by a close-spaced vapor process, Appl. Phys. Lett. 33 (1978) 319.
[131] R.R. Nair, P. Blake, A.N. Grigorenko, K.S. Novoselov, T.J. Booth, T. Stauber, N.M.R. Peres, A.K. Geim, Fine structure constant defines visual transparency of graphene, Science 320 (2008) 1308.
[132] K.B. Nam, J. Li, M.L. Nakarmi, J.Y. Lin, H.X. Jiang, Deep ultraviolet picosecond time-resolved photoluminescence studies of AlN epilayers, Appl. Phys. Lett. 82 (2003) 1694.
[133] M. Dvorak, S.-H. Wei, Z. Wu, Origin of the variation of exciton binding energy in semiconductors, Phys. Rev. Lett. 110 (2013), 016402.

[134] L. Chen, B.J. Skromme, R.F. Dalmau, R. Schlesser, Z. Sitar, C. Chen, W. Sun, J. Yang, M.A. Khan, M.L. Nakarmi, J.Y. Lin, H.X. Jiang, Band-edge exciton states in AlN single crystals and epitaxial layers, Appl. Phys. Lett. 85 (2004) 4334.
[135] Y. P. Varshni, Physica, 34, 149 (19670).
[136] X.Z. Du, J. Li, J.Y. Lin, H.X. Jiang, Temperature dependence of the energy bandgap of multi-layer hexagonal boron nitride, Appl. Phys. Lett. 111 (2017) 132106.
[137] K.B. Nam, J. Li, J.Y. Lin, H.X. Jiang, Optical properties of AlN and GaN in elevated temperatures, Appl. Phys. Lett. 85 (2004) 3489.
[138] X.Z. Du, C.D. Frye, J.H. Edgar, J.Y. Lin, H.X. Jiang, Temperature dependence of the energy bandgap of two-dimensional hexagonal boron nitride probed by excitonic photoluminescence, Appl. Phys. Lett. 115 (2014), 053503.
[139] G.W. Semenoff, Condensed-matter simulation of a three-dimensional anomaly, Phys. Rev. Lett. 53 (1984) 2449.
[140] W. Paszkowicz, J.B. Pelka, M. Knapp, T. Szyszko, S. Podsiadlo, "Lattice parameters and anisotropic thermal expansion of hexagonal boron nitride in the 10–297.5 K temperature range, Appl. Phys. A**75** (2002) 431.
[141] R.B. Capaz, C.D. Spataru, P. Tangney, M.L. Cohen, S.G. Louie, Temperature dependence of the band gap of semiconducting carbon nanotubes, Phys. Rev. Lett. 94 (2005), 036801.
[142] S.B. Cronin, Y. Yin, A. Walsh, R.B. Capaz, A. Stolyarov, P. Tangney, Marvin L. Cohen, S.G. Louie, A.K. Swan, M.S. Ünlü, B.B. Goldberg, M. Tinkham, Temperature dependence of the optical transition energies of carbon nanotubes: the role of electron-phonon coupling and thermal expansion, Phys. Rev. Lett. 9**6** (2006) **1**27403.
[143] L.F. Voss, C.E. Reinhardt, R.T. Graff, A.M. Conway, R.J. Nikolic, N. Deo, C.L. Cheung, Comparison of CF4 and SF6 based plasmas for ECR etching of isotopically enriched 10boron films, Nucl. Instrum. Methods Phys. Res. A 606 (2009) 821.
[144] S. Grenadier, J. Li, J.Y. Lin, H.X. Jiang, Dry etching techniques for active devices based on hexagonal boron nitride epilayers, J. Vac. Sci. Technol. A 31 (2013), 061517.
[145] S.J. Pearton, J.C. Zolper, R.J. Shul, F. Ren, GaN: processing, defects, and devices, J. Appl. Phys. 86 (1999) 1.
[146] J. Li, Z. Y. Fan, R. Dahal, M. L Nakarmi, J. Y. Lin, and H. X. Jiang, "200 nm deep ultraviolet photodetectors based on AlN," Appl. Phys. Lett. 89, 213510 (2006).
[147] G.H. Lee, Y.J. Yu, C. Lee, C. Dean, K.L. Shepard, P. Kim, J. Hone, Electron tunneling through atomically flat and ultrathin hexagonal boron nitride, Appl. Phys. Lett. 99 (2011) 171103.
[148] S.L. Bellinger, R.G. Fronk, W.J. McNeil, T.J. Sobering, D.S. McGregor, Improved high efficiency stacked microstructured neutron detectors backfilled with nanoparticle **6**LiF, IEEE Trans. Nucl. Sci. 59 (2012) 167.
[149] S.L. Bellinger, R.G. Fronk, T.J. Sobering, D.S. McGregor, High-efficiency microstructured semiconductor neutron detectors that are arrayed, dual-integrated, and stacked, Appl. Radiat. Isot. 70 (2012) 1121.
[150] S. L. Bellinger, R. G. Fronk, and D. S. McGregor, "Method of Fabricating a Neutron Detector Such as a Microstructured Semiconductor Neutron Detector," US patent 8778715.
[151] Q. Shao, L.F. Voss, A.M. Conway, R.J. Nikolic, M.A. Dar, C.L. Cheung, High aspect ratio composite structures with 48.5% thermal neutron detection efficiency, Appl. Phys. Lett. 102 (2013), 063505.
[152] R. J. Nikolic, A. M. Conway, D. Heineck, L. F. Voss, T. F. Wang, and Q. Shao, "Method for Manufacturing Solid-State Thermal Neutron Detectors with Simultaneous High Thermal Neutron Detection Efficiency (>50%) and Neutron to Gamma Discrimination (>1.0E4)," US patent 8558188..
[153] R. Dahal, K.C. Huang, J. Cliton, N. LiCausi, J.-Q. Lu, Y. Danon, I. Bhat, Self-powered micro-structured solid-state neutron detector with very low leakage current and high efficiency, Appl. Phys. Lett. 100 (2012) 243507.
[154] R. Dahal, J. K. Huang, J. Q. Lu, Y. Danon, and I. B. Bhat, "Neutron-detecting Apparatuses and Fabrication Methods." US patent 9151853B2.
[155] K. Osberg, N. Schemm, S. Balkir, J.O. Brand, M.S. Hallbeck, P.A. Dowben, M.W. Hoffman, A handheld neutron-detection sensor system utilizing a new class of boron carbide diode, IEEE Sensor. J. 6 (2006) 1531.
[156] K.B. Pfeifer, K.E. Achyuthan, M. Allen, M.L.B. Denton, M.P. Siegal, R.P. Manginell, Microfabrication of a gadolinium-derived solid-state sensor for thermal neutrons, J. Radiat. Res. 58 (2017) 464.
[157] D.S. McGregor, T.C. Unruh, W.J. McNeil, Nucl. Instrum. Methods Phys. Res. 591 (2008) 530.
[158] A. Many, High-field effects in photoconducting cadmium sulphide, J. Phys. Chem. Solid. 26 (1965) 575.
[159] A. Maity, S.J. Grenadier, J. Li, J.Y. Lin, H.X. Jiang, Effects of surface recombination on the charge collection in h-BN neutron detectors, J. Appl. Phys. 125 (2019) 104501.
[160] L.K. Gallos, A.N. Anagnostopoulos, P. Argyrakis, Conduction anisotropy in layered semiconductors, Phys. Rev. B50 (1994) 14643.
[161] R. Dahal, K. Ahmed, J. Woei Wu, A. Weltz, J. Lu, Y. Danon, I.B. Bhat, Anisotropic charge carrier transport in free-standing hexagonal boron nitride thin films, APEX 9 (2016), 065801.
[162] H.G. Spieler, E.E. Haller, Assessment of present and future large-scale semiconductor detector systems, IEEE Trans. on Nucl. Sci., **NS-** 32 (1985) 419.
[163] C.A. Klein, Bandgap dependence and related features of radiation ionization energies in semiconductors, J. Appl. Phys. 39 (1968) 2029.
[164] W.A. Noonan, Neutrons: it is all in the timing - the physics of nuclear fission chains and their detection, Johns Hopkins APL Tech. Dig. 32 (2014) 762.
[165] J. Neal, L. Boatner, Z. Bell, H. Akkurt, M. McCarthy, Evaluation of neutron and gamma detectors for high-temperature well-logging applications, in: Future of Instrumentation International Workshop (FIIW), 2011, pp. 172–175.
[166] N. Coudurier, R. Boichot, F. Mercier, R. Reboud, S. Lay, E. Blanquet, M. Pons, Growth of boron nitride on (0001) AlN templates by high temperature-hydride vapor phase epitaxy (HT-HVPE), Physics Procedia 46 (2013) 102.